International Journal of Extreme Manufacturing

TOPICAL REVIEW • OPEN ACCESS

Laser powder bed fusion of biodegradable magnesium alloys: process, microstructure and properties

To cite this article: Xuehua Wu *et al* 2025 *Int. J. Extrem. Manuf.* **7** 022007

OPEN ACCESS
IOP Publishing | IMMT
International Journal of Extreme Manufacturing
Int. J. Extrem. Manuf. 7 (2025) 022007 (45pp)
https://doi.org/10.1088/2631-7990/ad967e

Topical Review

Laser powder bed fusion of biodegradable magnesium alloys: process, microstructure and properties

Xuehua Wu[1], **Junying Liu**[1], **Youwen Yang**[1,2,*], **Jing Bai**[3], **Cijun Shuai**[1,*], **Joseph Buhagiar**[4] **and Xinghai Ning**[2,*]

[1] School of Mechanical and Electrical Engineering, Jiangxi University of Science and Technology, Ganzhou 341000, People's Republic of China
[2] College of Engineering and Applied Science, Nanjing University, Nanjing 210089, People's Republic of China
[3] School of Materials Science and Engineering, Southeast University, Nanjing 211189, People's Republic of China
[4] Department of Metallurgy and Materials Engineering, University of Malta, Msida, Malta

E-mail: yangyouwen@jxust.edu.cn, shuai@csu.edu.cn and xning@nju.edu.cn

Received 30 June 2024, revised 21 September 2024
Accepted for publication 23 November 2024
Published 5 December 2024

Abstract

Magnesium (Mg) alloys have gained recognition as revolutionary biomaterials, owing to their inherent degradability, favorable biocompatibility and mechanical properties. Additive manufacturing (AM) provides high design flexibility and enables the creation of implants with personalized complex shapes and internal porous structures tailored to individual anatomical and functional needs. Particularly, laser powder bed fusion (LPBF), one prevalent AM technique, utilizes a fine laser beam as heat source and results in tiny molten pool with extremely fast cooling rate, which effectively restricts grain growth, inter-metallic precipitation and macroscopic segregation, thus facilitating the fabrication of high-performance metal parts. This review critically assesses the significance of biodegradable Mg alloys and investigates the feasibility of utilizing LPBF for Mg alloys applications in biomedical field. Detailed discussions on LPBF-processed biomedical Mg alloys parts cover process parameters, microstructure, metallurgical defects, and properties like mechanical performance, corrosion behavior, and biological response in both as-built and post-processed states. Additionally, suggestions for advancing knowledge in LPBF of biodegradable Mg alloys for biomedical applications are highlighted to propel further research and development in this field.

Keywords: additive manufacturing, Mg-based materials, microstructure features, mechanical performance, biological properties

---

[*] Authors to whom any correspondence should be addressed.

2631-7990/25/022007+45$33.00

1. Introduction

Recently, biodegradable metals including magnesium (Mg), zinc (Zn) and iron (Fe), have garnered significant interest in biomedical field owing to their distinctive degradability, excellent biocompatibility, and high mechanical strength [1–10]. These biodegradable metals can gradually dissolve and be safely absorbed *in vivo* through a self-corrosion pattern [11]. This unique characteristic eliminates the necessity for additional removal surgeries after tissue healing, reducing the risk of potentially long-term complications [12, 13]. Mg alloys, in particular, are accepted as a potentially revolutionary biometal for potential orthopedic and cardiovascular applications [2, 6, 14–16]. With a density of 1.79–2.0 g cm^{-3} and a Young's elastic modulus of 35–45 GPa, Mg alloys closely match the characteristics of natural bone (15–30 GPa), effectively alleviating stress shielding effects at the interface of implant between bone [17]. The biodegradation product, mainly Mg^{2+} ions, is essential nutrient for bone tissue, and is able to promote bone regeneration and differentiation, whereas excessive Mg^{2+} would be easily excreted through human metabolic processes [18, 19].

The use of Mg alloys in biomaterials can be traced back to 1878, when Edward and Hughes first used pure Mg wire to suture wounds and blood vessels [20]. Early clinical trials of Mg-based implants faced significant challenges, particularly their rapid degradation rates, resulting in an almost complete halt of clinical applications in the mid-20th century. With the technological advances in developing new Mg alloy series with enhanced corrosion resistance, renewed interest in medical applications began [2]. In 2000, Heublein *et al* utilized the biodegradability of Mg alloys for the development of cardiovascular stents [21]. In 2013, a milestone was reached with the successful development of the first commercially produced Mg-Y-RE-Zr bone screws, MAGNEZIX®, by Syntellix AG [22]. In 2016, the Korean Food and Drug Administration (KFDA) certified an Mg–Zn–Ca alloy screw (K-MET) for internal fixation of metacarpal fractures [23]. At the same year, high-purity Mg screws (99.99%) were approved for therapeutic applications related to the femoral head and neck fracture in China [24]. After that, Shanghai Jiao Tong University designed a novel biodegradable Mg alloy named JiaoDa BioMg (JDBM), an Mg–Nd–Zn–Zr alloy with controlled degradation behavior and exceptional antibacterial properties suitable for cardiovascular stents [25]. Currently, Aap implantate AG and MeKo laser material processing eK in Germany are prominent producers offering both standard and customized biodegradable Mg-based implants. After extensive research and advancements in this field, a variety of small-sized biodegradable commercial Mg implants, like Mg-based screws, pins, suture anchors, and plates, are being researched for various applications such as orthopedic implantation, bone fixation devices, surgical instruments [3, 26–28].

Nowadays, the most common manufacturing techniques for Mg alloys include casting, die-casting, forging, and subsequent machining [29, 30]. However, the production of intricate Mg-based implants remains challenging due to its hexagonal close-packed crystal structure, which limits formability at room temperature. However, it is well-known that the shape of the biodegradable implant usually needs to be customized according to the specific defect morphology of the patient, in order to enhance the morphological adaptability during the implantation surgery. Thus, some scholars have addressed this challenge by increasing the deformation temperature to enable super plastic forming. Nonetheless, this method comes with limitations on part sizes and configurations. Moreover, the implanted material not only needs to have a suitable degradation rate and biomechanical properties, but also requires an interconnected porous structure with mimic shapes and distributions for cell growth and nutrient transport, especially for cardiovascular stent, tissue engineering scaffolds [31–33]. Taking bone tissue engineering scaffold as an example, the pore size should be in the range of 100–600 μm, with a porosity of $\geqslant$70%, to facilitate cell adhesion, oxygen and nutrient entry, and metabolic waste removal [34].

Recently, additive manufacturing (AM), also known as 3D printing, has revolutionized fabrication processes [35–41]. This innovative technique constructs objects layer by layer using 3D model data, freeing designers from the constraints of geometric intricacies [42, 43]. AM methods can be categorized into seven families, including vat polymerization, material jetting, material extrusion, powder bed fusion, binder jetting, sheet lamination, and direct energy deposition, in accordance with the ASTM F2792-12a [44]. Among them, powder bed fusion and direct energy deposition technologies are the two main AM processes for metal parts [45, 46]. Direct energy deposition technology is primarily utilized for creating large, rough-shaped components, while powder bed fusion technology excels in the manufacture of complex parts with high dimensional accuracy [47]. Particularly, laser powder bed fusion (LPBF) shows significant advantages in manufacturing biodegradable Mg alloys device with internal porous structure and outer personalized shape [48, 49]. As a typical AM technique, it can be deeply integrated with modern medical imaging such as computed tomography, magnetic resonance imaging and computer-aided design technology [50]. Thus, it can accurately replicate the complex external anatomical morphology of defective tissue, and finely design the internal structure based on biological functional requirements [51, 52].

Notably, the LPBF of Mg alloys faces great challenges as compared to other metals, since Mg metal has a lower melting point and higher chemical reactivity [53]. Besides, the high saturated vapor pressure of Mg metal makes it prone to intense evaporation under laser irradiation, leading to changes in the chemical composition of the as-build parts and the formation of defects such as cracking, porosity and keyholes. In 2015, Wei *et al* firstly adopted LPBF to prepare ZK60 parts, demonstrating the application potential of LPBF in preparing Mg implants [54]. It was also demonstrated that the evaporation of metal powder led to low densification rate, thereby affecting the mechanical properties. Recently, with the significant improvement of AM equipment and the quality of specialized Mg alloy powders, the densification rate and dimensional accuracy of LPBF-processed Mg alloy parts have been greatly improved [50]. Relevant experts have begun to explore the preparation of fine porous structures using LPBF. In 2015, Jauer *et al* first used LPBF to fabricate porous AZ91 part, proving that it was feasible to fabricate porous degradable Mg alloys with complex shape [55]. In 2022, Liu *et al* evaluated the biological performance of WE43 scaffolds prepared by LPBF, and found that the integrity of the scaffold was compromised after implantation, but exhibited good osteoconductive effects [56].

There is no doubt that the use of LPBF to fabricate Mg alloy medical devices with adaptable structures for the tissue repair and functional reconstruction has become the current mainstream development direction. Currently, a large number of researchers have been conducting cutting-edge research on LPBF of biomedical Mg alloys, and have achieved some substantial progress in process optimization, microstructure, and performance [2–4, 7, 26, 57–67]. However, there is a noticeable lack of reviews specifically addressing the progress and challenges specific to LPBF of biodegradable Mg alloys, particularly regarding the correlation criteria between microstructure evolution, degradation behavior, and biocompatibility. In this paper, it is aiming to fill these gaps by presenting a thorough review covering LPBF of biodegradable Mg alloys. The forming mechanism, microstructure feature, mechanical properties, degradation behavior and biocompatibility, are systematically discussed. Furthermore, the current challenges and prospects are summarized to provide some guidelines to drive the innovation, upgrade, and development of high-performance biomedical devices.

2. LPBF of Mg alloys

2.1. LPBF characteristics

LPBF technology, as previously called as selective laser melting (SLM), was first proposed by the Fraunhofer Institute in Germany around 1995 [60]. It is based on the development of selective laser sintering (SLS) technology. SLS technology uses a laser beam to locally heat powder materials below their melting point to bond them together, while SLM further increases the temperature above the melting point to achieve complete fusion between powder particles [68]. By 2002, the Fraunhofer Institute announced significant success in SLM technology, enabling the direct production of fully dense metal components in one step [59]. This breakthrough marked the transition of LPBF technology from the experimental stage to practical applications, showing potential in aerospace, medical, automotive and other fields [69]. With the continuous advancement of laser technology, powder material preparation technology, computer-aided design and manufacturing software, and control system technology, as well as the performance, stability, and cost-effectiveness of LPBF equipment have gradually improved, promoting its wide application in industrial production [70].

As shown in figure 1, the specific steps involved in LPBF process are described as below [64, 71]: (i) creating a 3D model using digital data from medical professionals for custom or standard implants, converting it to a stereo-lithography (STL) file, and slicing it into uniform thin layers to obtain initial prototype segment data. (ii) Directing a precise laser beam to scan the top layer of powder bed in a selective cross-sectional pattern, applying heat to melt and form a single layer based on the prototype information. (iii) Lowering the powder bed by the thickness of one layer and adding a new powder layer over the melted section. This layer-by-layer process continues until the desired 3D geometry is achieved. Due to the distinctive physical and chemical properties, Mg powders are easily contaminated, leading to deterioration of mechanical properties for final parts. Usually, a protective environment within the processing chamber is maintained by using inert gas like argon, so as to prevent oxidation of Mg metal powder [60]. In particular, considering that Mg metal is prone to producing evaporation and smoke under the action of high-energy laser beam, a device for removing smoke and dust is usually installed in the processing chamber [58]. For example, Qin *et al* have specially set up an airflow field above the powder bed to timely remove the smoke and dust with suitable airflow, thereby reducing the negative interference of smoke on the laser molten pool [72].

The characteristics of LPBF and other AM methods adopted for processing Mg alloys are described in table 1. Overall, LPBF integrates high-precision and high-performance manufacturing of metal parts, which is primarily attributed to several following factors [4]: (i) the smaller laser spot (50–80 μm) makes the heating process more accurate, which brings about small molten pool, and resultant high forming accuracy with surface roughness below 30–50 μm. (ii) During LPBF, the ultrafast cooling rate (10^6–10^8 K·s^{-1}) can be achieved through interfacial heat transfer of tiny molten pools, which is able to reduce the segregation of composition and precipitation of second phases, forming the non-equilibrium structure with fine grains. (iii) LPBF is particularly suitable for manufacturing parts with complex shapes and internal features such as irregular structures, especially intricate biomimetic porous structures that are often difficult or even impossible to achieve through traditional manufacturing processes. Therefore, LPBF has emerged as a highly effective approach for producing personalized metal parts with exceptional precision, reproducible intricate geometries, fine-grained microstructures, and superior comprehensive performance. This positions them well to meet the growing demand for high-performance, customized biodegradable Mg alloy implants tailored for orthopedic and cardiovascular surgeries [60].

2.2. Process parameters optimization

2.2.1. Laser parameters. In LPBF of biodegradable Mg alloys, a variety of parameters are involved, mainly including laser power, scanning speed, hatch space and layer thickness [71, 86]. The laser power determines the energy density of the laser beam interacting with the underling powder bed, while the scanning speed tailors the duration of laser-material interaction [72, 87–90]. Insufficient power or excessive scanning speed results in unmelted defects like pores, compromising structural integrity. Conversely, excessive power or slow scanning rates lead to over-melting issues such as splashing or

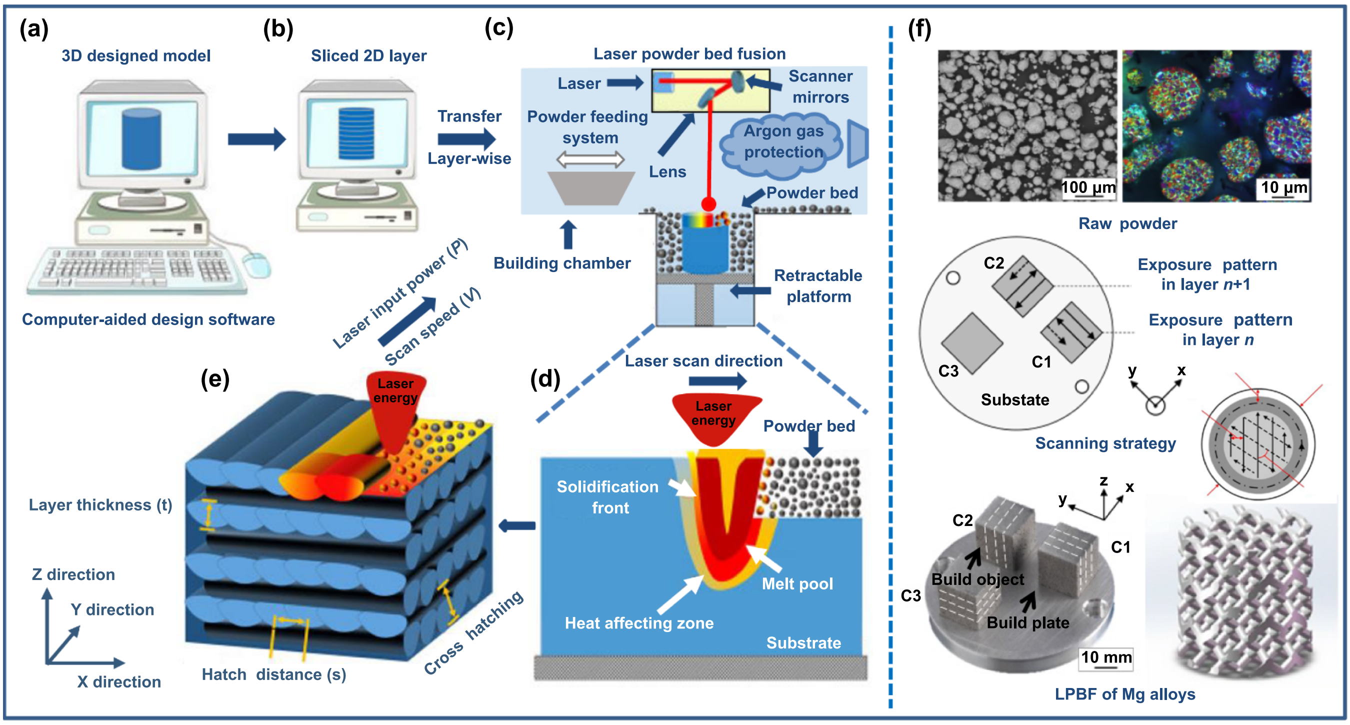

Figure 1. Schematic diagram of LPBF-processed counterparts: (a) creating CAD model, (b) obtaining initial prototype segment data, (c) applying laser heat to melt and form a single layer, (d) the relationship of the laser and power bed, (e) the desired 3D geometry, and (f) the final cubic counterparts.

Table 1. The characteristics of AM methods adopted for processing Mg alloys.

Methods	Advantages	Disadvantages	References
LPBF	Ability for complex geometries or interconnected network structure with high dimensional accuracy and precision Excellent mechanical properties High powder recyclability	High costs Less material flexibility Low forming efficiency Inability for larger components	[49, 55, 58, 61–65, 67, 73, 74]
SLS	Support free Isotropic final products Complex geometries	Porosity and shrinkage Poor surface quality Post-processing for final appearance	[64, 73, 75]
Direct energy deposition	Minimizes waste Part repair and modification Efficiency for larger components	Insufficient precision Poor formation quality	[76, 77]
Wire arc AM	Low cost High material utilization rate Efficiency for larger components	Low cooling rate Large deformation Insufficient precision Inability for complex geometries	[61, 62, 64, 65, 67, 74, 78]
Binder jetting	Exceptional resolution and details Multi-material and full-color Wide array of materials	High costs Restricted build volume Low printing speed Inadequate mechanical properties	[64, 65, 73, 74, 79, 80]
Sheet lamination	Low geometric distortion Good surface finish Ability to produce large structures	Poor tensile and sheer properties Swelling effect Weak bonding at the interface	[64, 65, 67, 74, 81, 82]
Material extrusion	Low cost Speed efficiency Low maintenance Ability to produce porous structure	Requires high temperatures Requires supports Inability for certain geometries	[83–85]

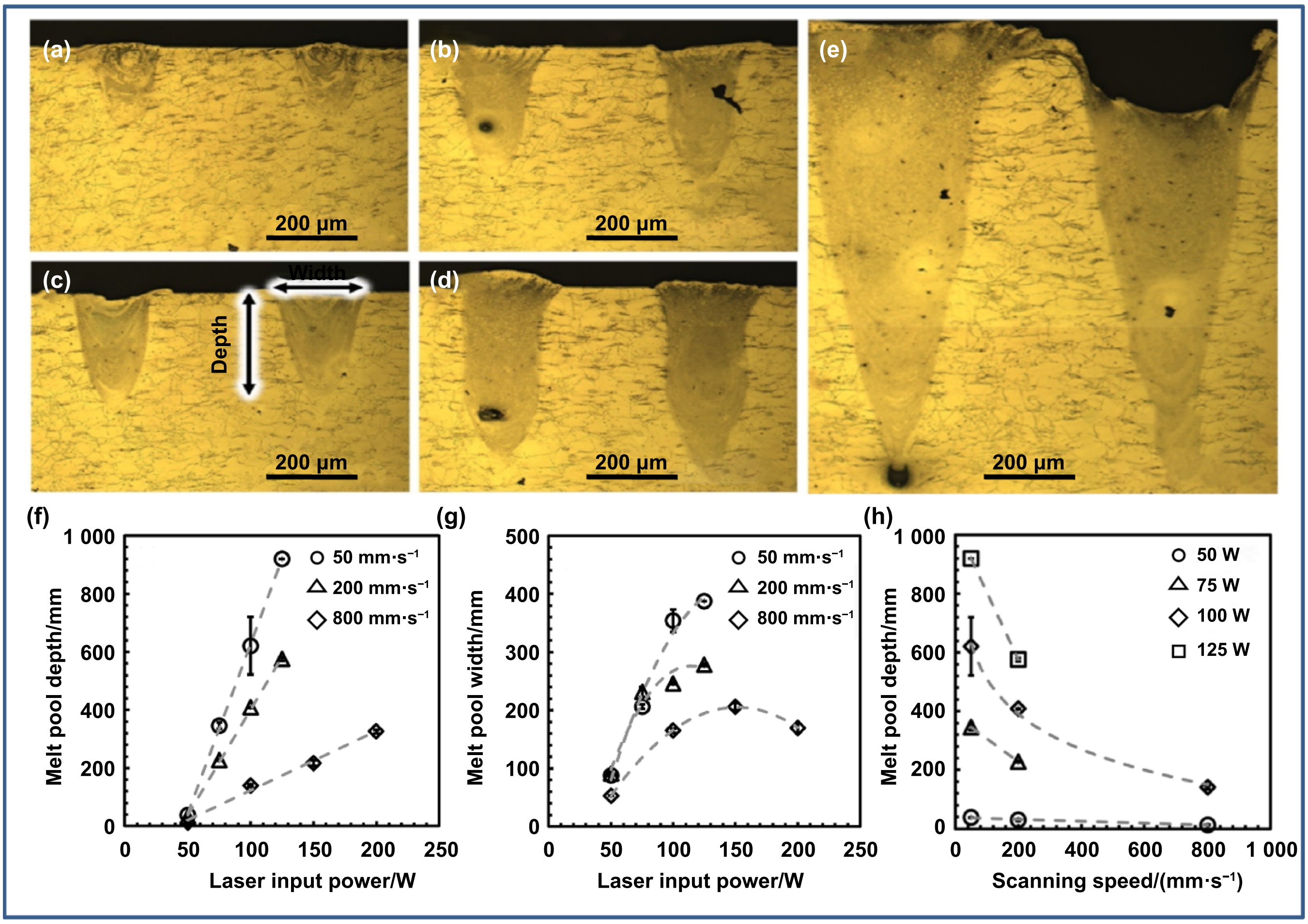

Figure 2. Optical micrographs showing specific molten pool shapes observed during a single-track experiment: (a) 150 W at 800 mm s^{-1}, (b) 75 W at 200 mm s^{-1}, (c) 75 W at 50 mm s^{-1}, (d) 125 W at 200 mm s^{-1}, and (e) 125 W at 50 mm s^{-1}, respectively. (f)–(h) The depth and width as function of the laser energy input or scanning speed. Reprinted from [91], © 2020 Elsevier B.V. All rights reserved.

burning, especially for Mg alloys with low boiling point. As a result, the depth and shape of molten pools along the building direction vary significantly with processing parameters [91, 92], as shown in figure 2. The results showed that the depth varied linearly with laser power input, as shown in figure 2(f), while the width varied parabolically with laser power input, as shown in figure 2(g). In contrast, the dimensions of the molten pool showed a decrease as the scanning speed increased, as shown in figure 2(h). Meanwhile, pores observed at low power levels were unfused-pores, while those at high power levels were primarily keyhole-pores formed by premature Mg vapor escape into the molten pool. Wang *et al* investigated the effect of different laser power levels on the surface quality of LPBF-processed AZ61 parts [93]. At low laser power, surface imperfections were observed due to crater accumulation, while excessively high-power levels resulted in rough, irregular surfaces with notable alloy element loss and decreased densification rates. Similarly, Wei *et al* also observed that low scanning speeds caused notable element evaporation, resulting in ablated pits on sample surfaces [54]. Optimal scanning speeds reduced element evaporation, yielding defect-free parts. However, too fast scanning speeds led to incomplete powder melting, reducing relative density to 82.25% and forming internal pores in the samples.

Hatch space refers to the distance between the midpoints of consecutive laser beams, a crucial factor for ensuring proper adhesion between adjacent tracks in laser processing. The adjustment directly influences the overlap rates of neighboring tracks, which in turn affects the heat transfer behaviors and surface qualities [94]. Usually, smaller hatch distances result in smoother surfaces by creating more continuous transitions between melt pools, reducing distinct pool traces [87]. However, too small hatch space with large overlap scale between molten pools will cause serious element burning and grain growth [95]. When the hatch space increases, the gradual lack of heat input increases the dislocation density, residual stress and composition fluctuations [96]. Therefore, excessive hatch space can lead to interference between melt pools, resulting in a rippled surface [97]. Moreover, a larger hatch space increases the likelihood of insufficient melting, which can result in the formation of defects such as discontinuities and porosities.

Layer thickness is another important parameter that needs optimization to reduce porosity, enhance layer bonding, and

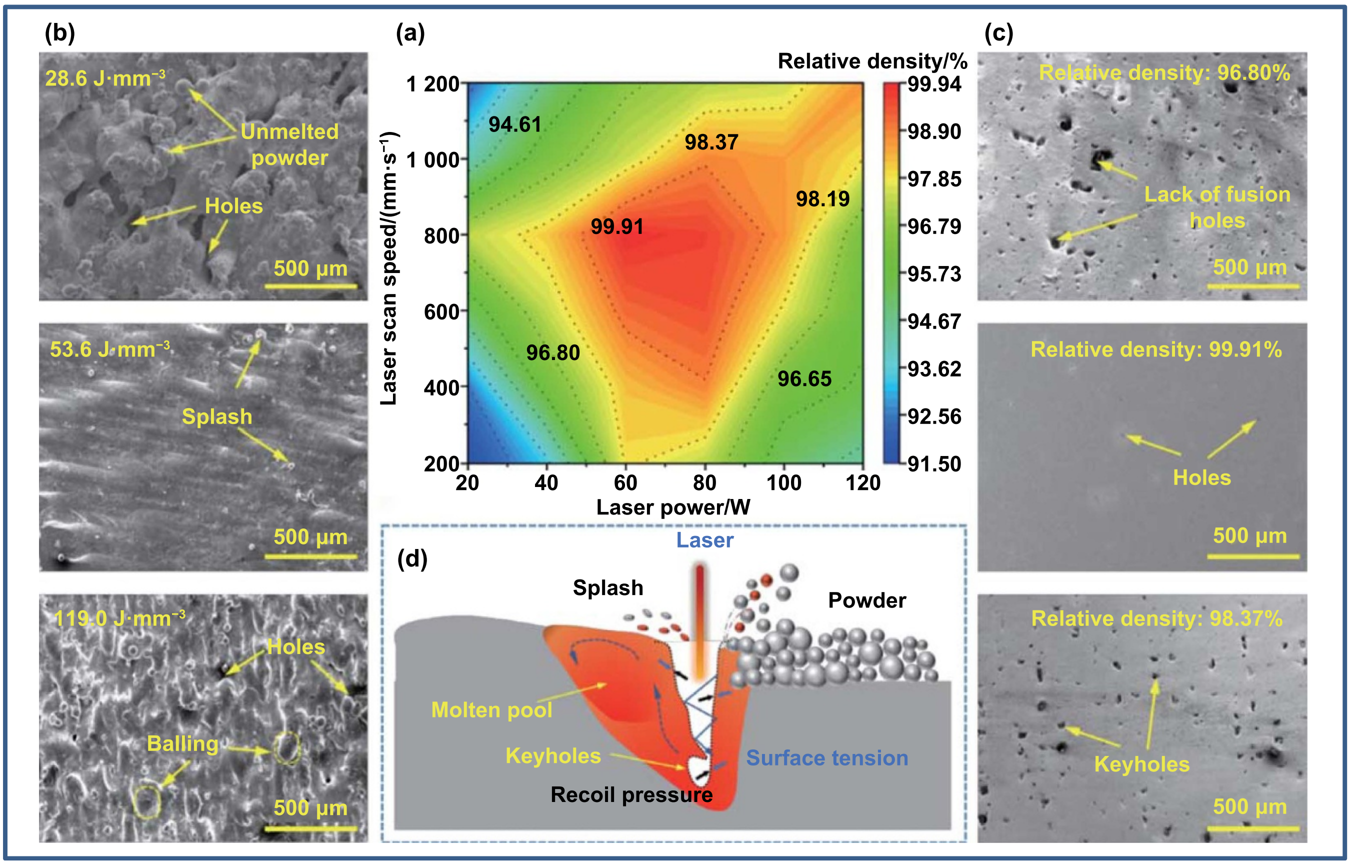

Figure 3. Formation qualities of LPBF-processed WE43 counterparts at various parameters. (a) Densification rate map. (b) Top surface. (c) Cross-section obtained at various input energy densities (28.6, 53.6, and 119 J mm^{-3}). (d) The diagram of molten pool with keyhole feature. Reproduced from [103]. © The Author(s). Published by IOP Publishing Ltd. CC BY 4.0.

create dense components [98, 99]. A thinner powder layer thickness offers higher resolution, enabling accurate reproduction of intricate object details like sharp corners and narrow grooves. Conversely, thicker layer thickness can decrease resolution, affecting object accuracy and surface quality [100]. It should be noted that the layer thickness is interdependent on various factors. In general, maintaining a minimal layer thickness enhances metallurgical bonding between layers by facilitating deeper penetration of molten pools, promoting multiple remelting cycles, and improving wetting characteristics. However, reducing layer thickness below the minimum limit can pose challenges in achieving uniform powder spreading [100].

In fact, the quality of laser forming is comprehensively influenced by above factors. Thus, laser energy density ($E_v = P/vst$) is usually adopted to estimate combination effects of these factors, where P, v, s, and t are laser power, scanning speed, hatching space and layer thickness, respectively [45]. Till now, there have been several studies that have reported the influence of laser energy density on the formation quality of LPBF-processed Mg alloys [89, 101, 102]. Similar to other metals, the appropriate energy density helps to accurately control the size and shape of the melt pool, thus achieving high-precision dimensional control. For instance, the formation quality of the as-built WE43 was conducted in our previous study [103], as shown in figure 3. An optimal range of 60 W $\leqslant P \leqslant$ 80 W and 600 mm $s^{-1} \leqslant v \leqslant$ 800 mm s^{-1} was identified for producing nearly fully dense (>99.5%) counterparts. In other words, the suitable energy density ranged from 53.6 to 95.2 J mm^{-3}. Excessive or insufficient energy density can lead to an oversized melt pool or inadequate melting, causing dimensional deviations, warping, or deformation of the parts [63, 104]. Meanwhile, the laser energy density affects the cooling rate and solidification process of the melt pool, thereby influencing the microstructure (such as grain size, morphology, and distribution). Rapid cooling typically produces fine and uniform grains, which is beneficial for enhancing the material's mechanical properties [60]. Notably, Mg alloys are more prone to burn damage and thermal cracks than other metals at relatively high laser energy densities, mainly due to their low saturation vapor pressure and poor deformability [53]. Nevertheless, the above research results only provide a qualitative reference, since determining the optimal process parameters is highly dependent on the specific experimental setup, hardware, and other factors. Thus, achieving the right combination of parameters for producing fully dense Mg-based parts remains a significant challenge.

2.2.2. Scanning strategy. The spatial movement pattern of the laser beam, namely scanning strategy, also significantly influences the microstructure and performance of as-built parts due to variations in local heat distribution [105]. By combining factors such as scanning direction, sequence, vector length and rotation angle, different scanning strategies can be created. Currently, LPBF-processed Mg alloys primarily employ a back-and-forth scanning strategy, with the scan direction of neighboring layers shifted by 45°, 67°, or 90° to achieve optimal density [66]. Ouyang *et al* explored the impact of different laser scanning patterns on the microstructure evolution of Mg alloy, including a standard raster pattern (R1), a modified raster pattern with an altered line order (R2), and a default zigzag pattern (Z1) [106]. The relative density of the produced porous scaffolds exceeded 99.5%, and the geometrical deviation was reduced to less than 10%. Wang *et al* used various layer rotation angles (0°, 37°, 67°, and 90°) along with different island sizes to fabricate Mg alloy samples [107]. The sample produced with a layer rotation angle of 67° and an island size of 4 mm × 4 mm exhibited the highest relative density (98.53%) and microhardness (95.64 HV).

Currently, there is a notable absence of research comparing the effects of different scanning strategies on the quality of LPBF-processed Mg alloys. Nevertheless, valuable insights can be drawn from LPBF of other metal alloys. Zhang *et al* investigated the effects of varying scanning strategies, including parallel, bi-directional, island, and re-melting scans, on the shape of molten pool, microstructure, residual stress, and mechanical properties of Al–Mg alloys processed through LPBF [108]. The sample produced using re-melting scanning strategy exhibited a relatively flat surface with the lowest roughness measuring (10.2 ± 0.9) μm and minimal stress of 0.195, primarily attributed to the reduced temperature gradient. Moreover, the tensile strength declined from 500 to 473 MPa, while the elongation (EL) also decreased from 15% to 7% following the re-melting scan. The phenomenon may be attributed to the enlargement of precipitation particles, leading to a shift in the strengthening mechanism from precipitate shearing to the Orowan dislocation looping mechanism.

3. Forming defects and related mechanisms

3.1. Alloying elements vaporization

During LPBF, the swift changes in temperature, from high heat to rapid cooling, along with high temperature gradients, lead to small molten pool dimensions and increased surface-to-volume ratios, which in turn raises the molten pool temperature, boosts vapor pressure, and triggers the transformation of vaporized particles/elements into the gaseous phase [109, 110], as depicted in figure 4(a). This occurrence is particularly notable in Mg alloys and Zn alloys, attributed to their low boiling point and intense vapor pressure, known as either alloying element vaporization or burnt alloying elements [111, 112]. Essentially, the evaporation of alloying elements is chiefly impacted by overheating and the extensive volatilization of elements like Mg and Zn in the molten pool. Subsequently, the surrounding powder of the molten pool is scattered, as illustrated in figure 4(b), leading to the emergence of the second type of spherical formation. When Mg and Zn are compared with Al and Cu, it can be observed that Mg and Zn have lower boiling points than Al and Cu (Mg 1 090 °C, Zn 907 °C, Al 2 467 °C, Cu 2 567 °C), leading to Mg and Zn exhibiting significantly reduced vapor pressures (5–10 orders of magnitude) compared to Cu in the temperature range of 2000–2600 K [110], as illustrated in figure 4(c).

According to the Langmuir model, the elements vaporization rate of Mg is 4.2×10^4–3.5×10^{10}, 5.4–160, 2.3×10^5–1.2×10^9 times of the elements vaporization of Al, Zn, and Mn, respectively, emphasizing that Mg is more prone to vaporization [109]. But it is worth mentioning that the weight percentage of the Mg element is much higher than that of the Zn element in Mg alloys. Besides, the diffusivity rate of vaporized Zn surpasses that of vaporized Mg in an argon atmosphere according to the Chapman–Enskog model [54]. As a result, more recondensed Mg tends to deposit immediately around the laser-irradiated zone, where it can melt again and partially compensate for the loss of Mg. Consequently, the final products exhibit a higher Mg/Zn ratio after processing, even though the overall amounts of both Mg and Zn decline due to the contraction of the molten pool and the evaporation of the elements [54]. Wei *et al* found that the relative mass fraction variation of Mg loss for the LPBF-processed AZ91D alloy exceeded 3 wt.% [109]. Furthermore, the impact of element vaporization on formability, microscopic characteristics, and mechanical properties of Mg–Zn–Zr samples were investigated [54]. Generally, within the temperature range of 1000–2600 K, the evaporation rate for Mg and Zn, which have lower melting points, exceeds that of Cu, which has a higher melting point, indicating that Mg and Zn are more likely to evaporate [110], as illustrated in figure 4(d). Overall, enhancing energy input or reducing scanning speed can prolong the molten pool's lifespan, potentially resulting in inadequate convection and increased loss of alloy elements. Encouragingly, Gieseke *et al* implemented an increased process pressure by 0.3 MPa to elevate the boiling point of Mg, prevent its evaporation, and decrease the loss of elements during the LPBF process [113].

3.2. Gas pores

Densification rate is a critical indicator of forming quality for parts produced through LPBF. Pores within LPBF-formed parts can be classified into different types based on their formation mechanisms: lack-of-fusion pores, keyhole pores, entrapment pores, and adsorption pores [114–116]. Lack-of-fusion pores arise from inadequate fusion between consecutive layers or passes during LPBF, resulting in voids or gaps in as-built part [63, 71]. Keyhole pores form when a spoon-shaped depression (keyhole) above the molten pool allows gas expulsion; however, instability can cause sudden closure, trapping gas and leading to gas pore formation post-solidification [117–120]. Entrapment pores occur when gases from the powder bed or shielding gas are not effectively expelled during laser processing, becoming trapped in the molten pool and

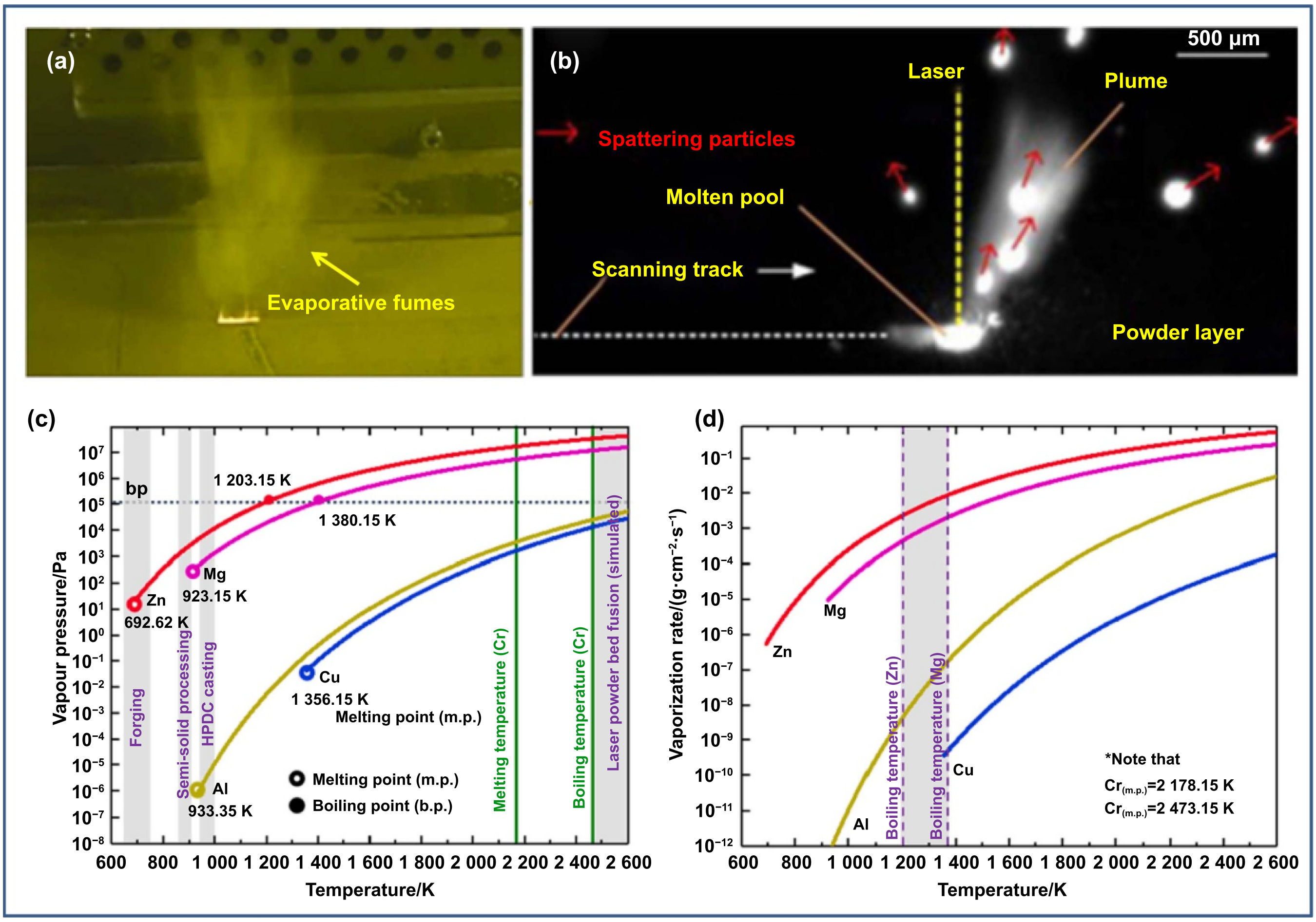

Figure 4. The Mg elements evaporation phenomenon during the LPBF process: (a) evaporative fumes and (b) spatter behavior observed by high-speed camera. Reprinted from [110], © 2021 Elsevier Ltd. All rights reserved. (c) and (d) The vaporization loss rate of different elements changed with the increase of temperature. Reprinted from [112], © 2021 Elsevier B.V. All rights reserved.

solidifying as variously shaped pores [121]. Adsorption pores emerge from gases absorbed on powder or substrate surfaces, releasing into the molten pool during laser heating and forming small bubbles upon solidification.

In LPBF of Mg alloys, the primary pore types are lack-of-fusion pores and keyhole pores, intricately linked to laser parameters as indicated in previous research [62]. Low E_v levels result in incomplete melting of the powder bed, leading to insufficient liquid for stable molten pool formation. This causes the molten pool to exhibit high viscosity, impeding smooth flow and spread, ultimately giving rise to lack-of-fusion pores [122, 123]. Higher E_v levels ensure complete melting of the powder bed by the high-energy laser beam, promoting molten pool evaporation [124]. As discussed above, the depth-to-width ratio of the molten pool increases gradually with rising E_v [125]. Once a certain threshold is surpassed, the heat conduction mode of the molten pool transitions from conduction mode (shallow and semicircular) to keyhole mode (deep and narrow) [125, 126]. In conduction mode, the cooling rate of the molten pool is relatively slow, which helps gases escape from the molten pool and reduces the formation of pores. In keyhole mode, the cooling rate of the melt pool is extremely fast and the internal flow is unstable. Keyhole depressions form under high energy density conditions where a large recoil pressure is generated resulting in the drilling of a deep depression in the melted metal, forming a high-aspect-ratio metal vapor filled cavity [127]. The presence of the vapor channel creates a high-pressure environment within the melt pool, causing gases to become trapped and unable to escape in time. At the same time, the metal vapor recoil effect induces typical keyhole defect characteristics, enhancing Marangoni convection and facilitating heat and mass transfer. Upon laser beam departure, keyholes gradually seal due to surface tension, achieving complete densification. Excessive E_v levels, however, intensify keyhole formation, causing severe evaporation during solidification [117]. Interestingly, keyhole-induced pores in high E_v settings are smaller than those from insufficient fusion at low E_v, owing to differing pore formation mechanisms [128]. Mg alloys' lower boiling points and higher vapor pressure pose challenges in balancing keyhole formation during LPBF due to rapid Mg evaporation. Nevertheless, adjusting process parameters can effectively mitigate adverse effects of excessive Mg vapor on formability, enabling high-density Mg alloy components production.

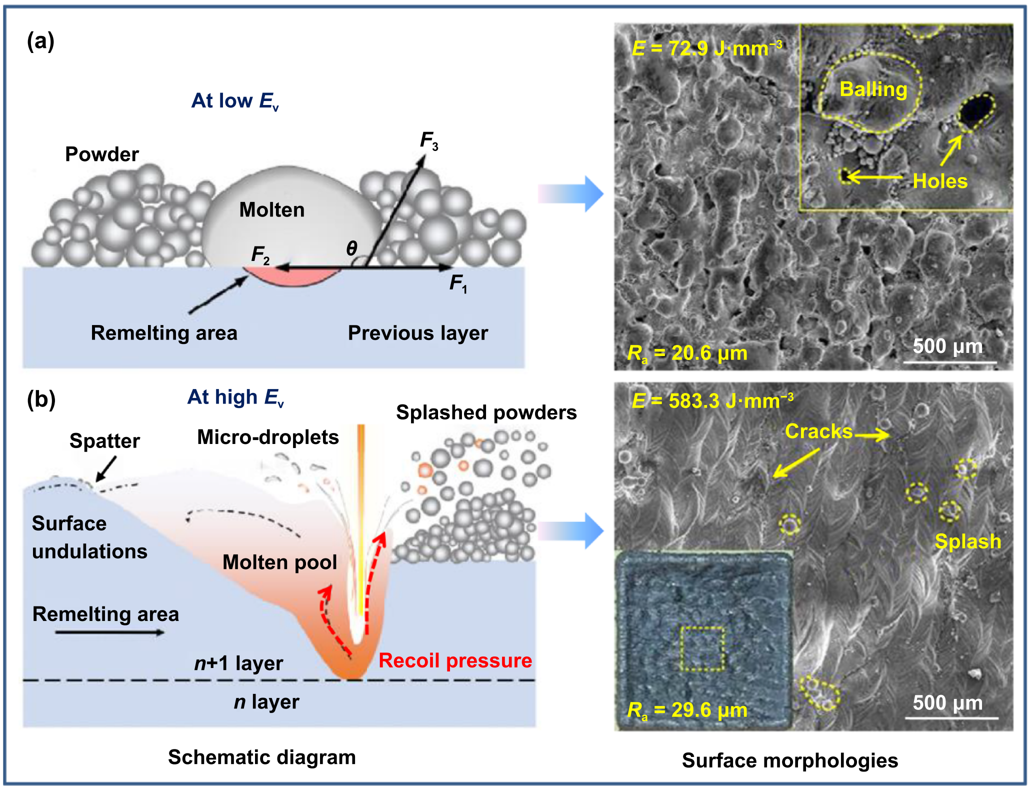

Figure 5. Schematic diagram of balling phenomenon and surface characteristics of LPBF-processed ZK60 Mg alloy at various energy conditions: (a) at low energy condition E_v and (b) at high energy condition E_v, respectively. Reprinted from [102], © 2022 Elsevier B.V. All rights reserved.

3.3. *Balling phenomenon*

In the LPBF process, the balling phenomenon occurs when molten metal on the surface transforms into a spherical shape, driven by factors such as gravity, gas interactions, and the surrounding solid environment. This transformation aims to minimize the difference in surface energy between the molten metal and its environment [129]. This occurrence is characterized by the aggregation of particles into spherical or ball-shaped structures, which is mainly attributed to inadequate process parameters and powder characteristics [56, 87, 89, 123, 129]. Liu *et al* investigated the influence of laser energy densities, ranging between 20.83 and 78.14 J mm^{-3}, on spheroidization process of AZ61 alloy [87]. The macro-surface exhibits four typical topographies: a strong surface balling pore region, weak surface balling pore region, rough scan track region, and flat smooth region. Generally, an insufficient laser energy is absorbed by the powder, which is frequently attributed to low laser power, high scanning speed, and thick layers, numerous powder particles will remain unmelted and keep their original shapes [89, 123].

As the molten pool appears, a mixture of fine particles and vapor gradually envelops it. The surface tension of the molten pool exceeds the binding force with the surrounding powders, leading the pool surface to shrink into a series of spherical shapes [102]. This contraction reduces surface energy and results in significant spheroidization phenomenon. Consequently, the particles surrounding the liquid phase will be assimilated and gather together to form a large metal ball due to the inadequate wetting between the liquid metal and solid surfaces [102], as illustrated in figure 5(a). In general, shrinkage-induced spheroidization is distinguished by the presence of large, irregular spheroids [130]. On the other hand, higher energy density from increased laser power and reduced scanning speed will also result in vigorous vaporization and splashing inside the liquid metal pool. This excessive energy can create a strong recoil pressure, leading to the fragmentation of the liquid melt into tiny droplets that descend back onto the material surface, forming spherical particles [102, 129, 131]. Moreover, due to the Gaussian distribution of laser power, powders located closer to the center of the laser beam, receiving higher energy, may undergo complete melting or vaporization, while those situated farther away may remain partially unmelted. The unmelted powders near the molten pool can be dispersed sideways by metal vapor, contributing to the formation of spherical particles [102], as illustrated in figure 5(b). In general, splash-induced spheroidization is characterized by small, nearly spherical spheroids [130].

Balling phenomenon in LPBF process can cause discontinuous metal balls on the substrate or previously solidified layers, affecting the microstructural characteristics of subsequent layers as well as the bonding strength between layers. To reduce spheroidization, it is vital to carefully select laser parameters for powder deposition [117]. By increasing the quantity of molten metal powders, especially those with uniform, fine, and regular-shaped particles with high bulk density, a larger molten pool size can be achieved, improving the fluidity of the molten metal. This facilitates easier spreading on the substrate surface and helps in suppressing spheroidization. Hu *et al* noted that the 400 mesh powder specimens displayed a rough surface containing numerous unmelted and round particles, whereas the 250 mesh specimens exhibited enhanced compaction [132]. The higher particle quantity in the 400-mesh powder resulted in an increased splashing of droplets from the melted pool due to the low surface energy in small-scale melts, leading to a more prominent balling phenomenon. Moreover, the distinctive physical and chemical characteristics of Mg may result in the generation of white oxides or oxide films when it reacts with oxygen in a high-temperature melted pool. These oxides float on the surface of the melted pool, diminishing the wetting capability and bonding efficiency. As a result, controlling the oxygen content or eliminating oxide films becomes crucial in preventing spheroidization. Currently, the profound understanding of the intrinsic impacts of processing parameters on balling phenomenon remains limited.

3.4. Crack

Cracks are highly destructive defects in LPBF, resulting from the interaction of material characteristics and residual stress deposition [133, 134]. Residual stress consists of thermal, microstructure, and constraint stress, where thermal stress stems from temperature variations among materials with different thermal expansion coefficients and elastic module, microstructure stress arises from phase transformations, and constraint stress occurs when surrounding materials or matrices restrict the expansion of the material being heated [135]. When these stresses exceed the material's strength limit, cracks form and propagate. During LPBF, the quick melting and rapid cooling of powder particles through localized laser energy input create a sharp temperature gradient ($\sim 10^6$ K s^{-1}), leading to increased thermal stress that remain in the final fabricated component [136]. Consequently, hot cracks, such as those arising from solidification and liquation cracks, as well as cold cracks, are prevalent in the microstructures of Mg-based products, significantly compromising component quality [112, 124, 137, 138].

The occurrence of hot cracking is closely associated with the creation of eutectic phases with low-melting-point or liquid films. Additionally, columnar crystals, developed under conditions of low constitutional supercooling and high temperature gradient, are particularly susceptible to hot cracking along boundaries between dendrites. Among them, solidification cracks typically emerge in the final stage of solidification and are impacted by various factors, such as the distribution and quantity of liquid phases, initial solidification phase, liquid phase's surface tension at grain boundaries, grain structure (fine equiaxed or coarse columnar crystals), metal plasticity, shrinkage tendency, and level of shrinkage obstruction [102], as depicted in figure 6(a). Liquation cracks appear in the heat-affected area, propagating along grain boundaries, predominant at moderate energy levels during the AM process [102], as illustrated in figure 6(b). Solidification and liquation cracks can combine, manifesting as extended, unbroken fissures [102]. Enhancing grain structure and forming strengthening phases along grain boundaries can reduce the occurrence of hot cracks. Generally, the refinement of grains and the precipitation of grain-boundary strengthening phases are beneficial for reducing the occurrence of hot cracks [139].

Cold cracks result from the build-up of thermal stress, which intensifies until it exceeds a critical threshold, causing the solidified microstructure to fracture and form cold cracks. Typically, these cracks appear in the middle of a sample rather than at the top or bottom due to the specific stress distribution [92]. In the research conducted by Deng *et al*, a notable macroscopic cold crack developed vertically in the printing stack direction, with the initial crack appearing around 4 mm in an LPBF-processed GZ151K sample [92]. The high temperature gradient and rapid temperature changes in the LPBF process generate substantial thermal stress from the molten pool's solidification shrinkage and subsequent cooling stage. As printing advances vertically, stress accumulates and strengthens [135]. Once thermal stress exceeds the material's tensile strength at current temperature, cold cracks form [135]. While some stress is relieved, it builds up again with increasing component height, leading to a repetitive cycle of thermal stress exceeding the material's tensile strength and causing cold crack formation at specific heights throughout the printing process [112].

LPBF of crack-free Mg-based parts is a significant challenge due to the complex thermal cycles and variations in powder characteristics caused by Mg evaporation. While the precise cause of crack formation remains uncertain, it is likely associated with powder splatter, as the likelihood of cracks decreases with decreased powder splatter under lower energy input. Several approaches have been suggested to tackle the issue of cracks [112, 140]: (i) modifying the material composition to improve ductility and resilience; (ii) optimizing process parameters such as minimizing energy input and optimizing scanning strategy; (iii) preheating the base material or employing laser re-melting to narrow temperature gradient and minimize the impact of thermal stress. It should be noted that varying localized heating may also result in diverse microstructures, potentially affecting the final mechanical characteristics of the fabricated component.

3.5. Oxide inclusions

Mg is easily prone to oxidation, even at room temperature and low oxygen pressure, making it extremely difficult from a thermodynamic perspective to prevent Mg oxidation. Therefore, oxide inclusions are a type of structural defect found among nonmetallic inclusions, typically situated on the surface layer and distributed as a thin film. Generally, the

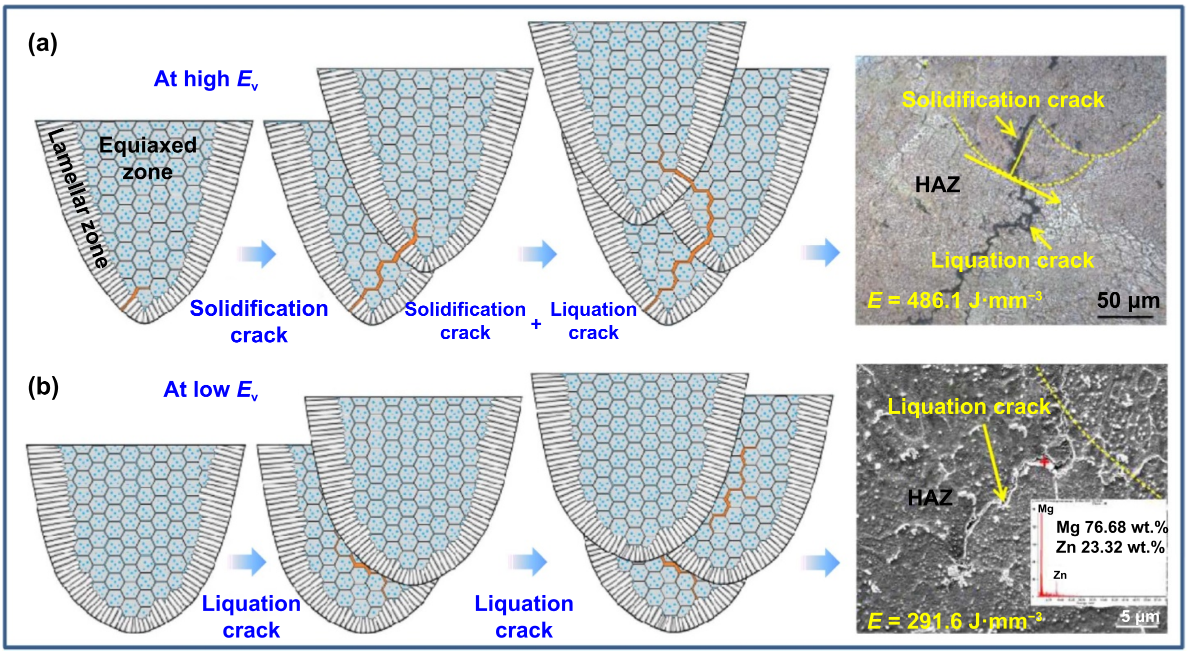

Figure 6. The schematic diagrams of solidification and liquation cracks at various energy conditions: (a) at high energy condition E_v and (b) at low energy condition E_v, respectively. Reprinted from [102], © 2022 Elsevier B.V. All rights reserved.

presence of oxide inclusions during the printing process can be explained by two primary causes: the natural oxide film or particles on the surface of the initial powder particles [63] and the absorption of oxygen from the protective gas during the LPBF process [141, 142], resulting in the creation of oxide films on the preceding layer. Salehi *et al* reported that at temperatures above 400 °C and with minimal oxygen content, MgO oxide film had the capacity to nucleate and grow on powder particles in the presence of oxygen impurities found in Ar gas [143]. It is hypothesized that the presence of oxygen in the powder may lead to the formation of voids and a decrease in the sample's mechanical properties. Deng *et al* observed evenly dispersed thin white oxide layers of Gd_2O_3 in the LPBF-processed G10K alloy, which stemmed from the oxides present in the initial powder and a slight amount of oxygen in the printing environment [112, 144], as shown in figure 7.

Generally, these oxidized inclusions can hinder interlayer bonding, impede the densification process, induce balling effects due to poor wettability, and initiate cracks under high temperature difference and pressure, significantly weakening the structural integrity of components. To minimize the presence of oxygen in the chamber, high-purity protective gas and appropriate process parameters are necessary, although complete elimination of oxygen is not achievable [145]. In addition, by incorporating active ingredients, passivation agents, and RE elements, it is also possible to reduce the content of oxides in Mg alloy powders [60]. Moreover, the Marangoni flow, also known as Gibbs–Marangoni effect, resulted by the increased energy density, can help minimize them by partially breaking the oxide films. However, the oxide film at the edges may remain undisturbed, forming an oxide 'wall' [145]. Besides, increased energy supply could also boost vapor pressure, thereby accelerating the elemental burning process simultaneously, and the crushed oxides could be encapsulated in the melted pool, impeding the diffusion and wetting of the surrounding materials, leading to the generation of micro-cracks and negative impacts on the mechanical characteristics of the final component.

4. Microstructure features

4.1. As-built

In LPBF, the key features are rapid solidification and layer-by-layer manufacturing. The fast-cooling rate creates non-equilibrium metallurgical structures with nano-scale grains, supersaturated solid solutions, and possibly amorphous phases. It also results in fine microstructures with varied precipitates compared to conventionally processed Mg alloys of the same composition. Fine precipitates tend to accumulate at grain boundaries, showcasing the unique characteristics of the melt pool. Besides, the as-built parts exhibit a high density of dislocations within each grain, likely due to thermal distortions influenced by melt pool constraints and thermal cycling. In terms of layer-by-layer construction, LPBF-prepared Mg alloys show anisotropy because of inconsistent thermal histories in different regions, or different directions. Currently, a series of Mg alloys, including RE–Mg, Mg–Zn, Mg–Al, Mg–Li, Mg–Ca have been reported for potential biomedical application. In general, their microstructure feature mainly includes fine grains and precipitates, anisotropy, high dislocation

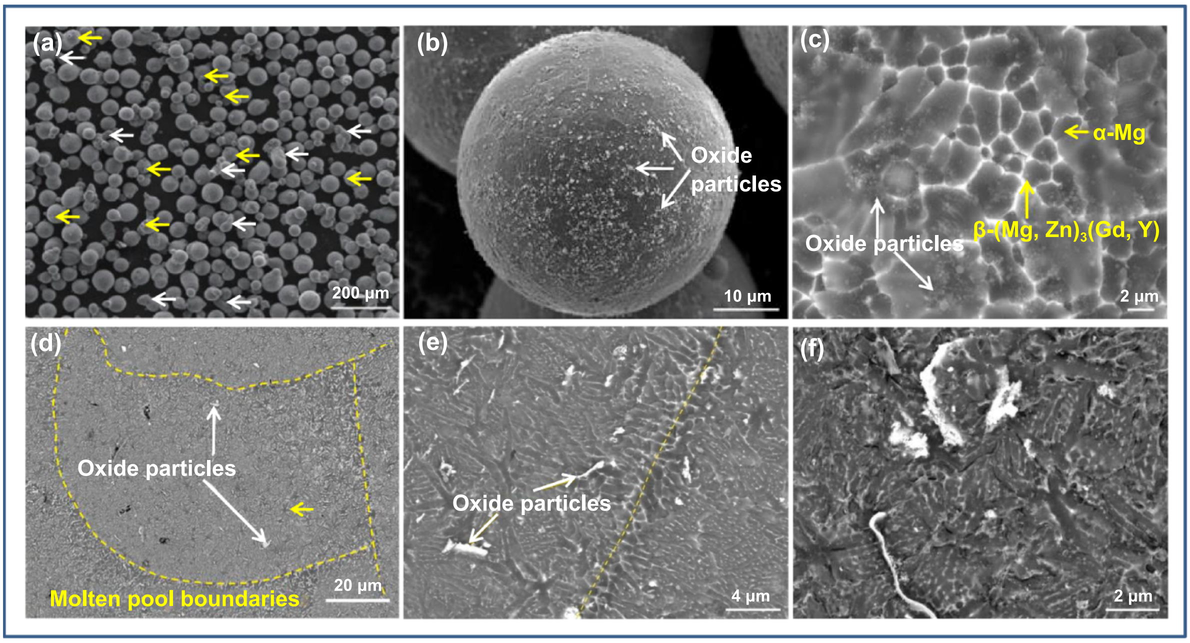

Figure 7. The SEM characterizations of the GWZ1031K unmixed powder: (a) the general appearance, (b) image captured by SE-SEM, and (c) image captured by BSE-SEM. Reprinted from [112], © 2021 Elsevier B.V. All rights reserved. (d)–(f) The BSE-SEM micrographs showing oxides formed in the as-built GWE1031 alloy. Reprinted from [144], © 2021 Elsevier B.V. All rights reserved.

density, and even non-equilibrium structure, which will be further discussed in upcoming chapter.

4.1.1. Fine grains.

Compared to those fabricated through traditional methods, LPBF-processed Mg alloys typically exhibit uniform and fine microstructures [146, 147]. Zumdick *et al* found that the as-built WE43 alloy exhibited refined and almost uniformly distributed equiaxed grains (1–3 μm), in stark contrast to the largest grains (approximately 44.3 μm) presented in the as-cast WE43 alloy [146]. Similarly, the rapid solidification rate also resulted in a significantly smaller average grain size in LPBF-processed ZK60 (7.3 μm) [102, 123] and AZ91D (1.2 μm) [89], compared to cast ZK60 (56.4 μm) and AZ91D (57 μm), respectively. Interestingly, both equiaxed and columnar grains were observed in LPBF-processed Mg alloys, in contrast to other metals like Ti-based and Ni-based alloys manufactured through LPBF process, which typically show epitaxial to columnar grain growth [101, 102, 148, 149]. In the research conducted by Liang *et al*, three distinct microstructure regions are observed in the LPBF-processed ZK60 alloy, including a central equiaxed zone with an average grain size of 8 μm, a perpendicular lamellar zone with a width of 20 μm along the melt pool's boundary, and a heat-affected zone (HAZ) displaying an average grain size of 10 μm outside the molten pool [102]. Notably, a columnar to equiaxed transition phenomenon was also observed in the 'last melt pool' of LPBF-processed WE43 alloy, with columnar grains in region I growing from pool edges towards the center, while equiaxed grains in region II nucleated ahead of the columnar grain zone [148]. Hence, the bulk counterparts contain two distinct types of particles: small grains averaging (1.4 ± 0.6) μm and large irregular-shaped grains with an average size of (20.4 ± 6.3) μm.

Undoubtedly, cooling rate is one of the key factors influencing grain size in LPBF process. Besides, the final grain morphology is determined by two key factors: the temperature gradient (G) and solidification rate (R). In general, higher cooling rates ($G{\cdot}R$) result in greater undercooling (ΔT) at the solid-liquid interface, which is beneficial for the formation of new grains and the ratio of G to R (G/R) determines the microstructure morphology, such as equiaxed, cellular, and columnar) after solidification [131]. In other words, when the freezing conditions near the solid-liquid interface do not provide adequate ΔT to form new nucleation points, columnar grains will be the dominant microstructure. At the melt pool's bottom, extremely high G combined with the smallest R will promote the growth of columnar grains more effectively due to the lack of sufficient ΔT, thereby suppressing heterogeneous nucleation occurs. Conversely, as the molten pool continues to cool and solidify, G decreases while R increases. In the upper part of the deposition, the minimum value G/R ratio results in significant ΔT and a high likelihood of nucleation, facilitating the CET (columnar to equiaxed transition) and the formation of equiaxed grains [102, 148]. In addition, it is noticed that the variation of chemical composition (such as the addition of Al, Mn, Cu, Zn, Zr, and RE) also plays a crucial role in the grain refinement for the LPBF-processed Mg alloys by generating the constitutional ΔT and providing extra heterogeneous nucleation sites through the precipitation of a second phase [138, 150–155]. This is another main reason for the formation of equiaxed-grain structure in additive manufactured Mg alloys. For instance, Shuai *et al* discovered that incorporating 1% Al into LPBF-processed Mg-3Zn alloy resulted in a

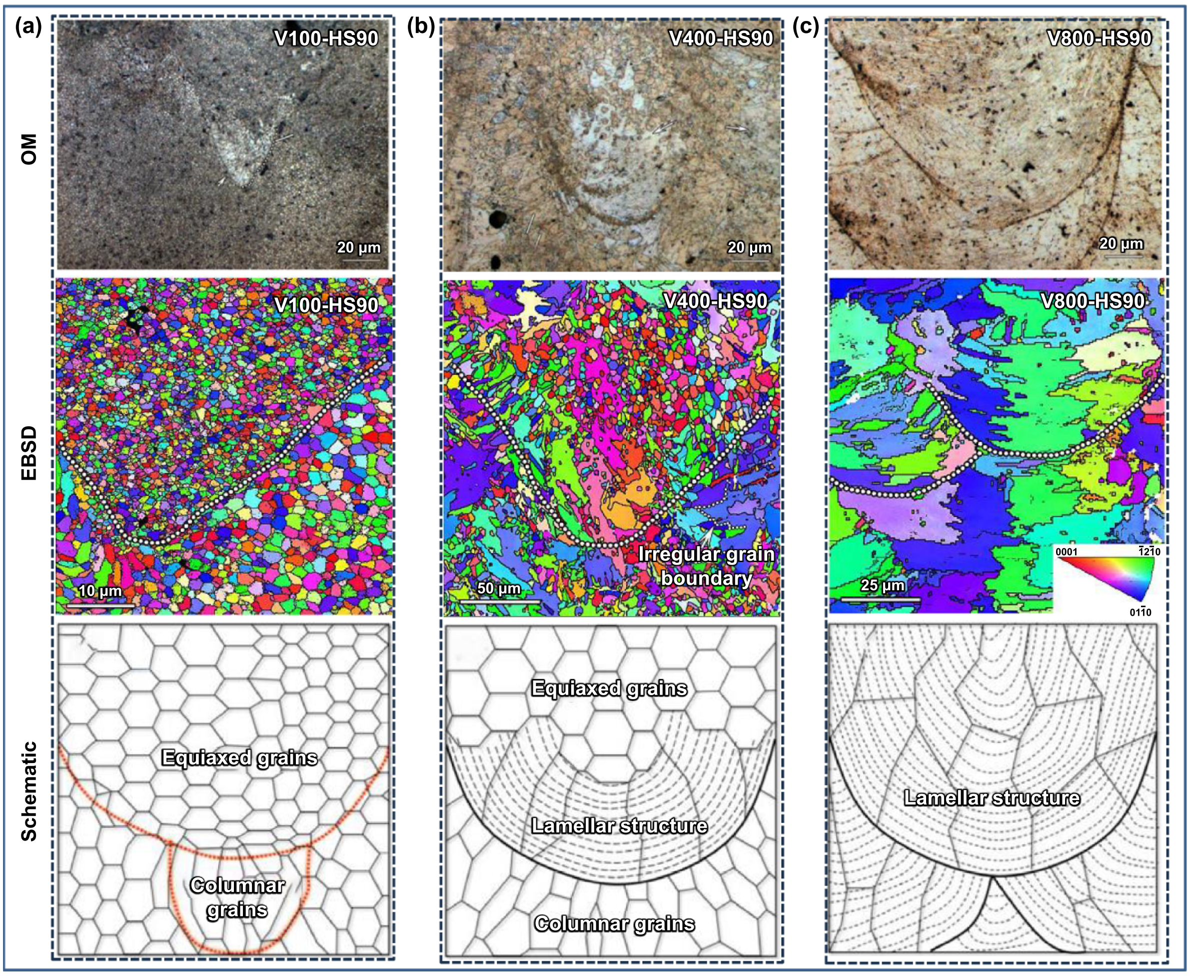

Figure 8. The OM images, EBSD mappings, and schematic diagram of the microstructure for the LPBF-processed NZ30K under different processing parameters: (a) V100-HS90, (b) V100-HS90, and (c) V100-HS90. Reproduced with permission from [88]. © 2022 Chongqing University. Publishing services provided by Elsevier B.V. on behalf of KeAi Communications Co. Ltd. CC BY-NC-ND 4.0.

significant reduction in grain size, reducing it from (21.6 ± 2.6) to (10.5 ± 1.9) μm [155]. Furthermore, with the increase of Al content to 7%, the grain size was further minimized to (6.8 ± 1.5) μm. Based on the CET (columnar to equiaxed transition) theory mentioned above, it is anticipated that pure Mg manufactured by LPBF would predominantly comprise columnar grains, due to the insufficient ΔT for CET occurrence during the solidification process. However, it is interesting to note that the LPBF-processed pure Mg exhibits equiaxed grains [156]. Some scholars attributed this deviation to the dynamic recrystallization induced by thermal accumulation or high thermal stress caused by the 'layer-by-layer deposition' feature [62]. In general, the formation mechanism of equiaxed to columnar grains growth in LPBF-processed pure Mg and Mg alloys remains a subject of debate, underscoring the need for further research to elucidate the specific mechanisms governing grain formation.

Besides, the laser parameters also play a crucial role in defining the grains during LPBF of Mg alloys. It is widely acknowledged that grain size tends to increase as energy density rises, due to the resulting decrease in cooling rate. The decrease in cooling rate reduces the number of possible nucleation sites at the solid–liquid interface and provides more time for grains growth, leading to coarser grains. Interestingly, an opposite linear relationship that grain size is decreased with laser energy density for LPBF-processed Mg-3Nd-0.2Zn-0.4Zr alloy (NZ30K) has been reported by Xu *et al* [88], as shown in figure 8. The results demonstrated that the microstructure evolved from large grains (approximately 8.99 μm) with a lamellar structure under low laser energy density (V800-HS90, 2.79 J mm^{-2}) to a combination of large grains (approximately 3.51 μm) with a lamellar structure, equiaxed, and columnar grains at moderate energy density (V400-HS90, 5.56 J mm^{-2}), and finally to fine equiaxed and columnar grains (approximately 0.93 μm) at high energy density (V100-HS90, 11.11 J mm^{-2}). Besides, the discovery of a lamellar structure within the large grain represents a novel characteristic in the LPBF-processed NZ30K alloy. They ascribed this abnormal phenomenon to the excellent grain refinement and high grain growth restrictive effect of the Zr element in the NZ30K alloy. According to the heterogeneous nucleation theory, the Zr particles formed during the crystallization of the dissolved Zr element must reach a critical size to serve as heterogeneous nucleation cores for α-Mg grains, thereby refining the grains. While the high cooling rate under low laser energy density inhibits the growth of the Zr particles, preventing them from achieving the critical size needed for heterogeneous nucleation, resulting in the formation of the larger grains with a lamellar structure. Conversely, the low cooling rate under high laser energy density promotes the growth of the Zr particles, allowing a greater number to reach the critical size necessary for heterogeneous nucleation, which leads to the formation of finer equiaxed grains.

4.1.2. Dispersed precipitate phase. Generally, the dispersed precipitate phase constituents of LPBF-processed Mg alloys are greatly influenced by their chemical composition. Among Mg–RE-based alloys, oxide formation is inevitable even if in an atmosphere with extreme low oxygen content and different combinations of RE elements could bring different phase constituents [91, 101, 144, 146, 157]. Besides, the oxides in LPBF-processed Mg–RE alloys, such as Y_2O_3 and Gd_2O_3, always with flaky shape will inhibit the appearance of secondary phase precipitation during the subsequent heat treatment (HT). In the research conducted by Esmaily *et al*, strong-basal-textured grains structure was identified with oxide particles, inter-metallic precipitates, and RE elements was observed near melt pool boundaries [101]. By analyzing with x-ray diffraction, the existence of inter-metallic like Mg_3Gd, $Mg_{41}Gd_5$, $Mg_{24}Gd_5$, as well as oxygen-rich compounds including MgO and Y_2O_3 was identified in the as-built WE43 alloy. Li *et al* found irregular oxide particles containing Y, along with inter-metallic precipitates abundant in Nd, Gd, and Y elements in the Mg matrix of the LPBF-processed WE43 porous scaffolds [157]. Besides, three types of inter-metallic precipitates were identified based on size, shape, and distribution relative to melt pool boundaries, including wavy fibrous patterns, aligned spherical precipitates arranged above the boundary, and horizontal structures below it, as shown in figure 9(a).

Among Mg–Zn-based alloys, a big obstacle lies in their poor printability, because they have a low eutectic temperature of approximately 325 °C and a broad solidification range [102, 123, 158]. In general, alloys with higher Zn content display two phases: primary α-phases and secondary inter-metallic phases. The microstructures of cast ZK60 and LPBF-processed ZK60 were compared by Wu *et al*, revealing that both samples had a matrix with equiaxed grains and precipitated phases [123]. Due to the suppression of the eutectoid reaction $Mg_7Zn_3 \rightarrow \alpha\text{-Mg} + MgZn$ at 325 °C during LPBF process, distinct precipitated phases were observed around the matrix in the two samples: MgZn in cast ZK60 and Mg_7Zn_3 eutectic phase with an orthorhombic structure in LPBF-processed ZK60, respectively. Moreover, the incorporation of Zn can greatly boost the amount of Mg_7Zn_3 eutectic structure and transform its appearance, shifting from a granular form to an almost mesh-like configuration gradually [158]. In the study conducted by Liang *et al*, three distinct microstructure regions were observed LPBF-processed ZK60 alloy, including a central equiaxed zone, a perpendicular lamellar zone along the melt pool's boundary, and a HAZ outside the molten pool [102], as illustrated in figure 9(b). Notably, nano-scale precipitates are distributed inside the grains. The further research showed that the nano-scale precipitates are rich in Zn and Zr, consisting of Zn-Zr inter-metallic surrounded by a Zn-rich region, as illustrated in figure 9(c).

Amongst Mg–Al based alloys [87, 89, 138, 159, 160], the majority of LPBF-processed Mg–Al alloys contain high levels of Al, due to the ability of Al to enhance strength through solid solution and the formation of $Mg_{17}Al_{12}$ inter-metallic phase, as well as its positive impact on printability. According to the Mg-Al phase diagram, the maximum solubility of Al in Mg is 12.5 wt% of at 450 °C, but this solubility decreases to less than 1 wt% at room temperature. Thus, any alloy with an Al content exceeding 1 wt% will result in the formation of the α-Mg phase and the precipitation of $Mg_{17}Al_{12}$ inter-metallic phase with an irregular shape [87, 89]. There exist two forms of $Mg_{17}Al_{12}$ inter-metallic phases, one that aligns with the grain boundaries, while the other manifests as nano-particles in spherical shape, ranging from 100 to 300 nanometers in diameter. Moreover, the content of initial Al element and the laser processing parameters could induce change in the $Mg_{17}Al_{12}$ phase morphology. With the increase in Al or the decrease in scanning speed, the volume fraction of $Mg_{17}Al_{12}$ precipitates increases due to the more pronounced evaporation of the Mg element. Moreover, the isolated inter-granular $Mg_{17}Al_{12}$ precipitates can merge and form a network when the volume fraction reaches a sufficiently high level [138].

4.1.3. High dislocation density. Generally, components produced by LPBF method have a higher geometrically dislocation density than those made by traditional casting methods. Due to the thermal distortions during printing, high dislocation density was possibly generated and primarily dictated by constraints surrounding the melt pool and thermal cycling [161–164]. In previous research [162], a generally higher density of dislocations was detected both in grain interiors and across grain boundaries in the LPBF-processed AZ91D alloys, compared to that in the extruded samples, as shown in figure 10. Recently, several mechanisms have been proposed to explain the formation of these dislocation structures [165]: (i) fine crystal structure. The rapid cooling observed in the LPBF process results in a refined grain structure, which increases the number of grain boundaries. Compared to the as-extruded counterparts, the LPBF-processed samples possessed an impressive uniformity in their microstructures or grain structures. At these boundaries, dislocations tend to accumulate and interact, consequently elevating the dislocation density, as shown in figure 10(b). (ii) Complex thermal history. Recent studies suggest that dislocation formation can be primarily driven by residual stresses resulting from the complex thermal cycles in the LPBF process. In the AM process,

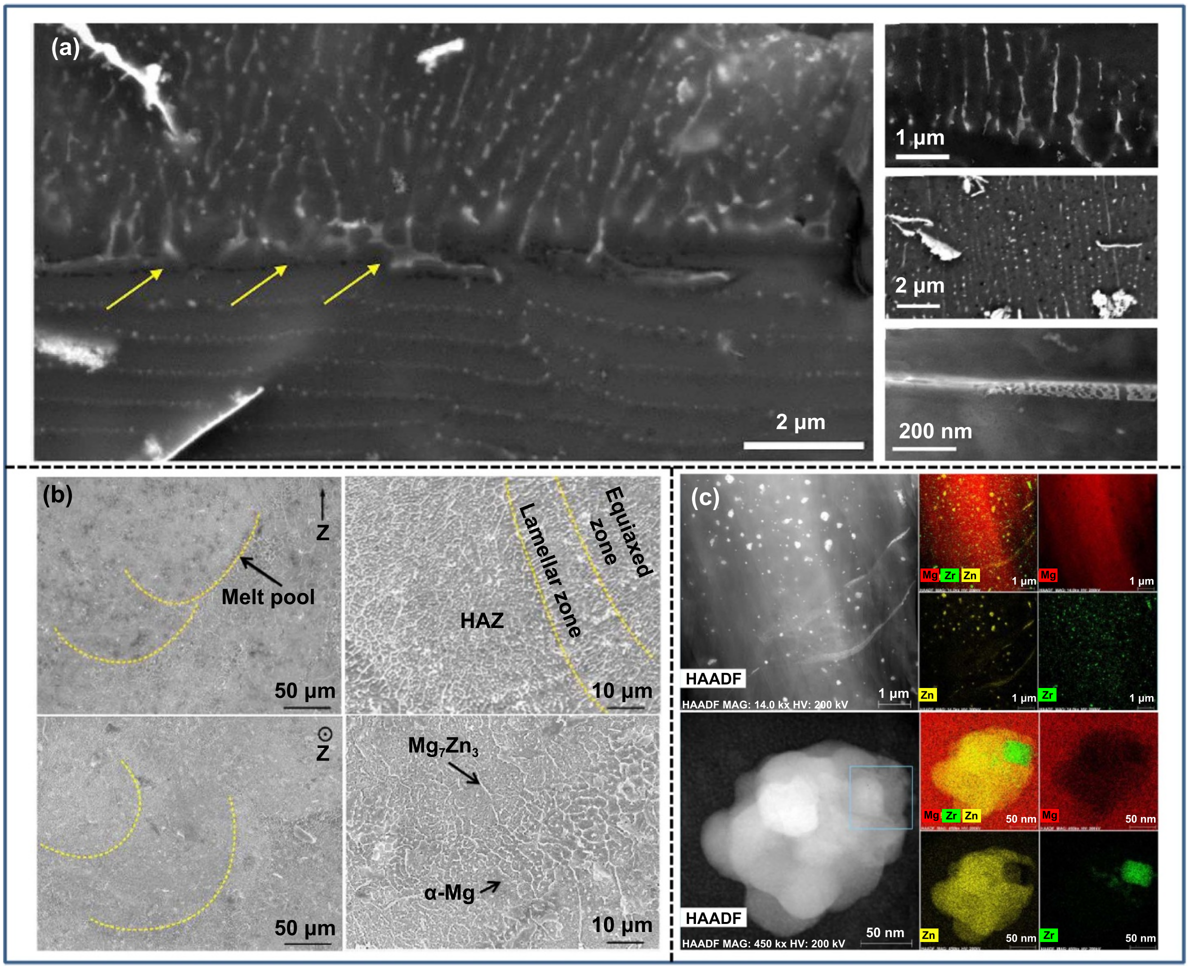

Figure 9. Various dispersed precipitate phases in the LPBF-processed Mg alloys. (a) Three different precipitate structures in the LPBF-processed WE43 scaffolds. Reprinted from [102], © 2022 Elsevier B.V. All rights reserved. (b) The microstructure of the LPBF-processed ZK60 alloy at different cross section. (c) The HAADF images of the nano-scale precipitates and the related elements' distribution. Reprinted from [157], © 2020 Elsevier B.V. All rights reserved.

molten metal solidifies rapidly within milliseconds due to the movement of heat sources. As deposition continues, the material undergoes multiple thermal cycles in the solid state, characterized by varying temperature rates and amplitudes. The substantial thermal gradient during the forming process creates a tension-compression cycle each time the laser beam scans the surface of the part. This cycle induces a unique dislocation structure as the material experiences repeated tensile and compressive stresses [166]. It was obvious that the lattice distortion in LPBF-processed samples was generally higher than that in the extruded samples, as illustrated in the figure 10(c). Besides, it can be observed that dislocations are distributed along defects, as stress concentration tends to occur at defect sites based on the Kernel average misorientation (KAM) maps, as shown in figure 10(a). Generally, the thermal expansion and shrinkage during rapid re-melting and solidification are considered to be the primary causes of dislocation structure formation [49]. (iii) Alloying element distribution. During rapid cooling, alloying elements may not have sufficient time to diffuse and distribute uniformly. This incomplete distribution enhances the solution strengthening effect, as these elements can instigate dislocation formation and hinder their movement, further increasing dislocation density.

As well known, dislocations are an important type of defect in crystals, and their presence and density directly affect the material's strength, plastic deformation ability, fatigue characteristics, and corrosion resistance [163, 167, 168]. For instance, a high entropy alloy with high density dislocation network structure and high volume fraction toughness nanoprecipitation has been synthesized by laser based AM technology, which shows excellent strength and tensile ductility by forming a unique dislocation-precipitated phase skeleton (DPS) structure [167]. Likewise, a high density of stacking fault distribution was also found in the Mg–Li alloys processed with LPBF in Dobkowska *et al*'s research [163]. The findings indicated that the dense stacking fault distribution can negatively impact the enhancement of the microscopic hardness of the Mg–Li materials manufactured through LPBF method. Besides, Bian *et al* proposed that the dislocation density will also affect the corrosion resistance of Mg alloys because the area with high density dislocation may become the preferred site for corrosion due to its higher chemical reactivity [162].

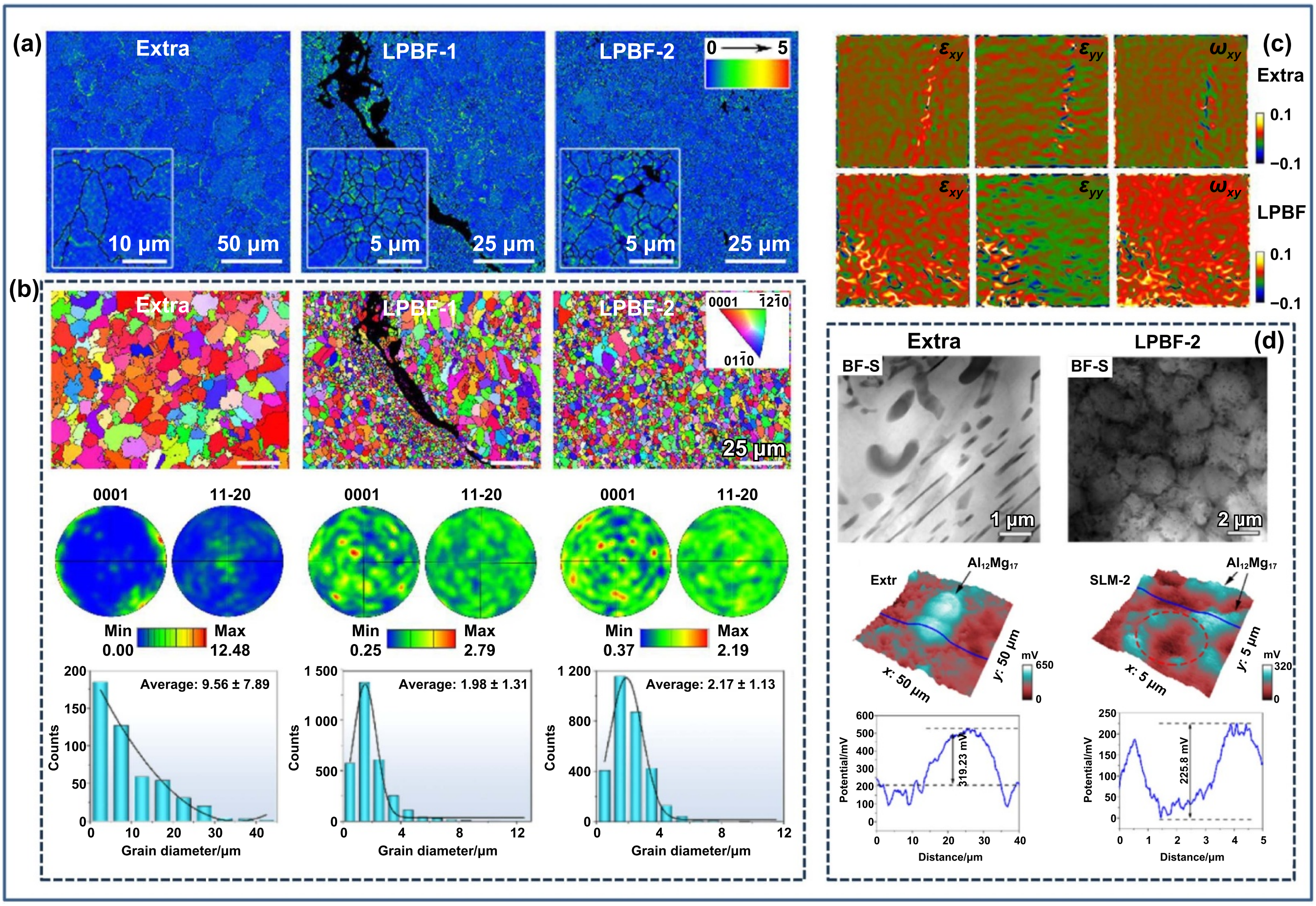

Figure 10. Accelerated corrosion mechanisms related to the unique LPBF-processed counterparts. (a) The kernel average misorientation (KAM) maps. (b) Inverse pole figures, pole figures and grain size distributions. (c) Geometric phase analysis (GPA) results and the typical distribution of second phase-based TEM images showing. (d) Potential difference on the sample surface of the extruded samples and LPBF-processed samples, respectively. Reprinted from [162], © 2024 Published by Elsevier Ltd on behalf of The editorial office of Journal of Materials Science & Technology.

Even though both the samples possessed the same constituent phases, the related microstructures were totally different. Fine $Al_{12}Mg_{17}$ phases (<30 nm) in LPBF-processed counterparts tend to be arranged at grain boundaries, forming the regular honeycomb-type microstructure and a great deal of Mn-rich precipitates (<100 nm) evenly dispersed in the matrix, forming the regularly spherical shapes. While, heterogeneous $Al_{12}Mg_{17}$ phases in extruded samples are much bigger (nano to 20 μms), and they are randomly distributed. Either dislocations or high local strain sites existed in the α-Mg matrix were in a high energy state, which could be preferentially attacked, as shown in figure 10(d). That is to say, the high dislocation density derived from LPBF process resulted in significantly accelerated micro-galvanic corrosion behaviors.

4.1.4. Quasicrystalline and amorphous Mg alloys.

Amorphous Mg alloy, especially Mg–Zn–Ca amorphous alloy, has attracted close attention in biomedical field [169–173]. Amorphous alloys, also known as metallic glasses, refer to metal alloys with short-range order and long-range disorder in atomic arrangement in the solid state. Due to the lack of grain boundaries, dislocations, and other crystal structural defects, amorphous Mg alloys generally exhibit superior corrosion resistance compared to their corresponding polycrystalline counterparts. In general, the microstructures of amorphous Mg alloys produced through LPBF are typically complex and heterogeneous. This complexity arises from the intricate thermal history involved in the laser multi-layer printing process.

A laser-printed component generally comprises two distinct regions: the molten pool zone (MP) and the HAZ [174], as shown in figures 11(a) and (b). These two regions undergo different thermal treatments, resulting in distinct microstructures consequently. In the molten pool zone, a rapid cooling rate is essential during the cooling process to prevent crystallization. As a result, the amorphous melt within the molten pool zone can solidify into a fully amorphous structure. Distinctively, the HAZ partially crystallized, composed of the glass and crystalline phase. Theoretically, in the HAZ, the temperature remains below the melting point (T_m) and does not enter the liquid phase. While, it is worth noting that the

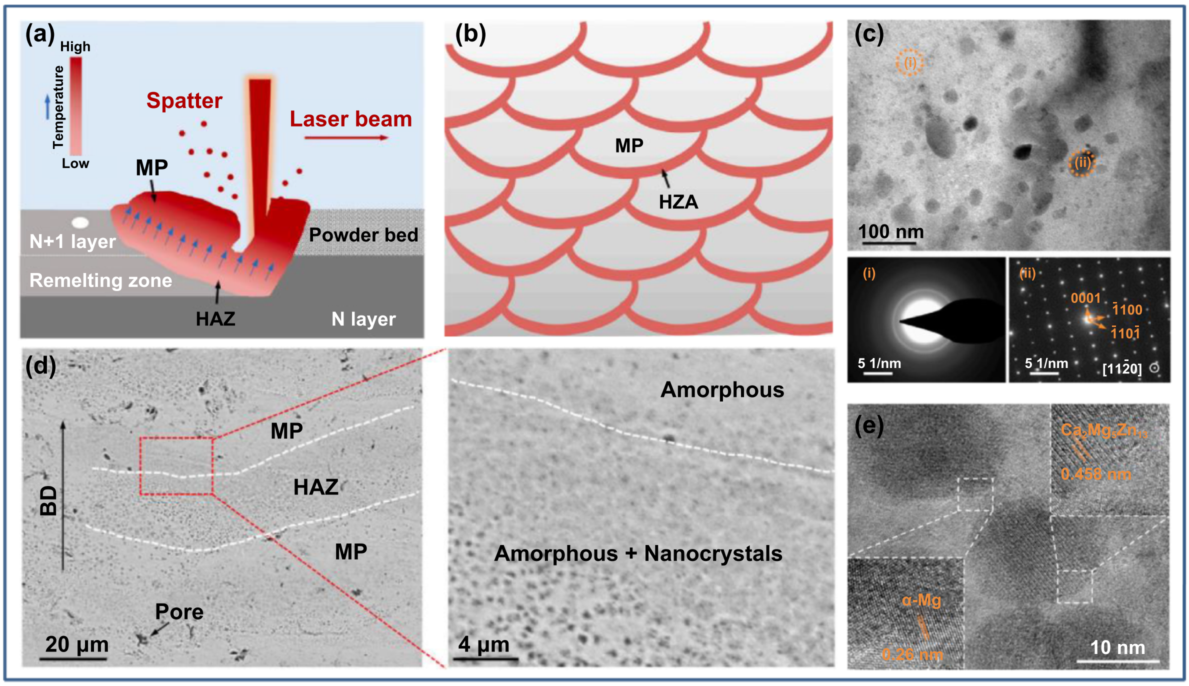

Figure 11. LPBF-processed quasicrystalline and amorphous Mg alloy: (a) the schematic diagram of laser powder bed fusion process, (b) the hierarchical microstructure of the as-built counterparts, and (c)–(e) the TEM, SEM and, HR-TEM maps showing the cross-section microstructure of LPBF-processed $Mg_{60}Zn_{35}Ca_5$ alloys, respectively. Reprinted from [169], © 2023 The Authors. Published by Elsevier B.V.

temperature in the HAZ still exceeds the crystallization temperature, which induced the transformation of the amorphous structure into crystalline structure during both the heating and cooling processes, consequently. Our team firstly utilized LPBF to fabricated amorphous Mg–Zn–Ca scaffold for biomedical application [169]. It was discovered that the as-built scaffold consisted of amorphous phase and a small amount of $Ca_2Mg_5Zn_{13}$ crystalline phase, as illustrated in figures 11(c)–(e). A close investigation revealed that the molten pool areas are mainly amorphous, with a few nano-crystals appearing in the HAZ. One reasonable explanation was that atoms in the HAZ above the crystallization temperature region will orderly arrange to nucleate into nano-crystals. Meanwhile, the melt pool experiences cyclic thermal accumulation during the layer-by-layer progress, promoting structural relaxation and further inducing crystallization.

In addition, some studies have indicated that the design of compositions can result in the formation of Mg alloys that contain quasicrystalline phases. For instance, Chen *et al* found out that incorporating the Y into LPBF-processed Mg–Zn–Zr led to the creation of a nano-scale and uniformly distributed quasicrystal I-phase (Mg_3Zn_6Y), characterized by strip-like and partially dot-like features [175]. This quasicrystal I-phase, due to the reduced potential difference, can act as a weak cathode, helping to reduce the risk of micro-galvanic corrosion in the Mg matrix. Additionally, the formation of rare earth oxide (Y_2O_3) on the surface of the I-phase enhances the density of the corrosion product layer, providing effective protection for the substrate and improving corrosion resistance. Notably, the quasicrystal I-phase, featuring a specialized icosahedral structure, maintains a specific orientation relationship with the Mg matrix, which results in a stable interfacial bond and initiates the Orowan strengthening effect. In addition, dislocation lines in the I-phase were anchored to prevent the sliding of dislocations, which resulted in increased mechanical strength. As a result of these combined effects, the LPBF-processed ZW61 component exhibited enhanced mechanical properties along with excellent biocompatibility.

4.1.5. Nano composites.

Combining the high stiffness and high strength properties of magnesium matrix composites (MMCs) and the technical advantages of AM forming complex structural parts with high performance, the LPBF-processed Mg-based composite materials offer great potential for fulfilling the requirements of lightweight, strong, and stiff materials in various fields like aerospace, defense, electronics, and biomedicine industries [176–180]. However, the poor dispersion and agglomeration of the reinforcement due to the strong van der Waals force between the nanoparticles and the very poor wettability with the Mg matrix will lead to stress concentration and crack initiation [181]. Besides, low interfacial bonding ability between the reinforcement and Mg matrix will contribute to the poor interfacial bonding strength. Therefore, ensuring the even distribution of reinforcements and optimizing the interface between reinforcement and Mg matrix are crucial for enhancing the overall properties of Mg-based composites [179].

To overcome poor wettability, Yuan *et al* utilized the semi-coherent interfacial bonding between Mg and MgO to increase the interfacial bonding strength, ensuring the effective transfer of load from the matrix to the carbon nanotubes and producing AZ91 alloys reinforced with carbon nanotubes coated with MgO [178]. Besides, employing *in-situ* reduction techniques is being explored as a viable approach to tackling interface challenges. Shuai *et al* devised a hydrothermal reaction/*in-situ* reduction method to enhance the interfacial compatibility of graphene oxide (GO) with AZ61 alloys, fabricating the TiO_2/GO-AZ61 composites successfully [182]. TiO_2 underwent *in-situ* reduction via a magnesiothermic reaction, with the resulting Ti combining with Al in the AZ61 matrix to produce $TiAl_2$. Simultaneously, Ti reacted with GO to generate TiC at the AZ61-GO interface. Due to formation of the intermetallic compounds at the GO/AZ61 interface, the reinforced interfacial bonding in turn led to a 12.5% reduction in the degradation rate and a 10.1% increase in compressive strength for AZ61-TiO_2/GO compared to AZ61-GO.

4.2. Post-processing treatment

As previously mentioned, the printability of Mg alloys poses a significant obstacle due to their high rates of oxidation, quick vaporization, and vulnerability to gas entrapment. These factors result in a range of defects in the final manufactured components, such as cracking, delamination, porosity, incomplete fusion, residual stress, deformations, non-uniform microstructure, and anisotropic mechanical properties. Studies indicate that the subsequent techniques like solution and aging HT, hot isostatic pressing (HIP), and surface modification can address issues like micro-segregation, reduce residual thermal stress, and enhance mechanical properties while keeping the original shape of LPBF-produced parts [26, 61]. Table 2 summarizes the microstructure evolution of the LPBF-processed Mg alloys before and after post treatment.

4.2.1. HT. Among the various post-processing treatments, HT have been recognized as a cost-effective method to adjust microstructural heterogeneity and eliminate defects that are inherently induced by rapid solidification or layer-by-layer building processes [91, 112, 144, 189, 191]. Usually, homogenization treatment is employed to dissolve undesirable phases, followed by aging treatment to enhance final strength through precipitation strengthening. In previous research, the impact of HT performed by heating to a temperature of 536 °C for a duration of 24 h, followed by subsequent aging at 205 °C for 48 h, on the microstructures and mechanical characteristics of LPBF-processed WE43 alloy were explored [91]. The globular β_1-Mg_3Nd precipitates initially dissolved and then re-precipitated into plate-like Mg_3Nd phase within α-Mg (hcp) matrix. Moreover, a flake-shaped structure containing dense nano-scale Mg and Y_2O_3 dispersoids agglomerates was uniformly distributed throughout the WE43 alloy. As a result, the maximum tensile strain at fracture of the LPBF-processed WE43 alloy increased significantly from 2.6% to 4.3%. Similar results were also discovered for the LPBF-processed porous Mg–Zn–Gd counterparts in our previous work [189]. During the HT, the precipitated β-$(Mg,Zn)_3Gd$ phase dissolved in α-Mg firstly and transformed into plate-shaped long period stacking ordered (LPSO) phases by reducing the energy threshold of stacking faults on basal plane, as shown in figures 12(a) and (b). Compared to β-$(Mg,Zn)_3Gd$ phase, the randomly distributed LPSO phases owned minor potential difference with α-Mg, thus causing less micro-galvanic corrosion.

In general, the HTs can improve various properties of the LPBF-processed counterparts. Deng *et al* investigated the influences of various solution treatment and aging HTs, including T4, T5, and T6 treatment, on the microstructure of LPBF-processed GZ112K alloy and GWZ1031K [112, 144], as illustrated in figure 12(c). As for GZ112K alloy, with suitable solution HT (400 °C for 12 h), the rigid and fragile β-$(Mg, Zn)_3Gd$ eutectic phase underwent a transformed into a comparatively softer lamellar 14 H type long period stacking order structure, which precipitated from α-Mg matrix with composition of Mg-9.7Gd-5.6Zn at.% inside grains, along with the formation of the X phase, which derived from eutectic phase with composition of Mg-9.8Gd-4.9Zn at.% along grain boundaries, resulting in improved ductility of LPBF-T4 alloy. Moreover, aging HT could enhance the ductility of LPBF-T6 alloy by refining grains, precipitation of prismatic β' precipitates, secondary phases of the 14H-LPSO structure, as well as strengthening from a combination of basal γ' and prismatic β' precipitates. The impact of T4 and T6 processes on LPBF-processed GWZ1031K is similar to that of LPBF-processed GZ112K alloy. LPBF-T4 achieved the best EL $(10.3 \pm 0.5)\%$, while LPBF-T6 showed the best yield strength (YS) (316 ± 5) MPa and ultimate tensile strength (UTS) (400 ± 7) MPa. In contrast to T4 and T6, the LPBF-T5 GWZ1031Kalloy showed remarkably high YS (365 ± 12) MPa but exceptionally low EL $(0.8 \pm 0.3)\%$.

4.2.2. HIP. As well-known, porosity poses a significant challenge in the LPBF process, leading to notable changes in the mechanical properties of the as-built counterparts. In fact, HIP, a commonly employed thermal-mechanical processing technique, which is carried out at elevated temperatures ranging from 1 000 to 2 000 °C and intense pressures of 200 MPa, can enhance the mechanical characteristics of the as-built components by reducing porosity and alleviating residual stresses [101, 183, 190, 192, 193]. Gangireddy *et al* studied the microstructure evolution during the HIP (350 °C under 15 ksi for 2 h) process for the LPBF-processed WE43 alloy [183]. The results showed that the previously identified Nd-rich precipitates, initially resembling long ribbons in the as-built states, fragmented into shorter but thicker plate-shaped structures measuring around 100–500 nm in diameter, as shown in figure 13(a). After HIP treatment, densification and EL of LPBF-processed Mg alloys can be significantly enhanced. This enhancement is more pronounced in alloys with higher initial porosities when the scanning speed is set at

Table 2. Summary of the microstructure evolutions of the LPBF-processed Mg alloys before and after post treatment.

Materials	State	Microstructures	References
WE43	LPBF	Nd-rich precipitates (platelet-shaped $Mg_{41}Nd_5$ and globular Mg_3Nd) and various oxygen-rich phases exist in the Mg matrix	[56, 91, 101, 148, 183]
	T4	Precipitate of fine and nano-scaled rectangular $Mg_{24}Y_5$ particles	[103]
	T6	The $Mg_{24}Y_5$ particles turned into $Mg_{41}Nd_5$ and formed a network structure. Globular precipitates β'-$Mg_{12}YNd$ decorates the grain boundaries and the plate-shaped precipitates β_1-Mg_3RE grows parallel to the prismatic planes of the Mg hcp lattice	[103, 157]
	HIP	Nearly all AM-induced microscopic pores are removed. Plate-like thicker Nd-rich precipitates, small globular Zr-rich precipitates, and Zr-Y-O rich oxides along with a large oxide exist in Mg matrix	[101, 183]
	HIP + T4	Dissolution of the minuscule Nd-rich and Y-rich particles	[101]
	HTO	A dense oxidation layer composed of Y_2O_3 and Nd_2O_3 and a transition layer contained few Mg-RE precipitates as well as similar α-Mg grains and Y_2 O_3 oxides to those of the matrix	[184–186]
	DCT	Smaller grain size. Lattice shrinkage, micro and compressive stress exist	[187]
	PEO	Form protective composite inhibitor-and-polymer-containing layers	[188]
Mg-Zn-Gd	LPBF	Primarily composed of α-Mg, β-$(Mg,Zn)_3Gd$ and $MgZn_2$ phases and exhibited nearly continuous distribution at grain boundaries of α-Mg	[189]
	T4	The precipitated β-$(Mg,Zn)_3Gd$ phase dissolved in α-Mg and transformed into plate-shaped LPSO phases	[189]
GZ112K	LPBF	Hard and brittle β-$(Mg,Zn)_3Gd$ eutectic phase and high solid solubility of Gd and Zn elements exist in α-Mg matrix	[117, 144]
	T4	Hard and brittle β-$(Mg,Zn)_3Gd$ eutectic phase transforms into a relatively softer lamellar 14 H type LPSO structure inside grains and X phase at grain boundaries	[144]
	T6	Basal γ' precipitates or lamellar 14 H-LPSO structure and dense prismatic elliptical β' precipitates coexist	[144]
AZ61	LPBF	Brittle-hardβ-$Mg_{17}Al_{12}$continuous precipitation exists along the grain boundary	[190]
	HIP	Partial dissolution of brittle-hard β-$Mg_{17}Al_{12}$ along grain boundaries and reduction of pores	[190]
ZK60	LPBF	Three types of precipitated phases were distributed inside the grains: Zn-rich precipitated phase with Zr-rich core, Zn-rich precipitated phase without Zr, and Zr-rich particle	[191]
	T4	The Mg_7Zn_3 phase at the grain boundary melted and merged into the matrix. The precipitated phases in the grain mainly evolved into Zn-rich phase with Zn_2Zr core	[191]
	T6	The rod-shaped $\beta1'$-MgZn precipitated phase separated out from the α-Mg matrix	[191]

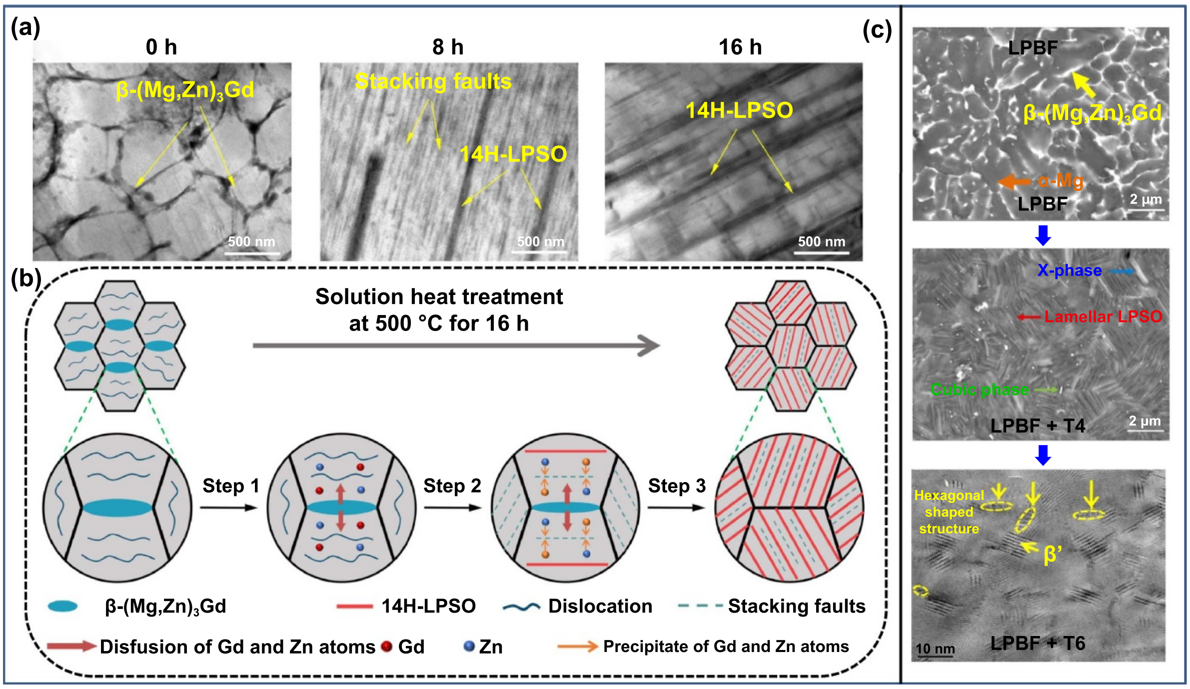

Figure 12. The schematics illustrate the microstructure evolution of the LPBF-processed parts and LPBF-T4 parts of Mg–Zn–Gd alloy: (a) bright-field images of as-built counterparts and (b) the formation of 14H-LPSO phase after heat treatment. Reprinted from [144], © 2022 Published by Elsevier Ltd on behalf of The editorial office of Journal of Materials Science & Technology. (c) The microstructure evolution of the LPBF-processed GZ112K under different heat treatment conditions. Reprinted from [189], © 2021 Elsevier B.V. All rights reserved.

1200 mm s^{-1}, as shown in figure 13(b). However, the improvement is limited for alloys with lower porosity levels at a scanning speed of 800 mm s^{-1}, as the porosity level increases with the scanning speed, as shown in figure 13(c). Besides, the reduced strength can also be attributed to the breakup of Nd-rich ribbon-like precipitates. Similarity, the influence of HIP (450 °C under 103 MPa for 3 h) on the microstructure of LPBF-processed AZ61 alloy was also studied [190]. Partial dissolution of brittle-hard β-Mg$_{17}$Al$_{12}$ along grain boundaries and reduction of pores resulted in increased densification and improved EL, with a slight decrease in micro-hardness and yield stress.

Generally, the improvement in the properties of as-built parts by HIP might insufficient, thus the combination of the HIP and HT has been indicated as a more effective method to improve the comprehensive mechanical properties of the LPBF-processed counterparts. Esmaily *et al* evaluated the effects of HIP (520 °C under 15 ksi for 4 h) and HT (525 °C for 8 h) on the microstructure and corrosion behavior of LPBF-processed WE43 specimens [101], as illustrated in figure 14(d). Minimal grain growth was observed in LPBF-processed WE43 after HIP, attributed to solute drag effects and the pinning effect of flake-shaped oxide particles. Following HIP + HT treatment, the enhanced corrosion resistance in WE43 could be explained to the dissolution of the minuscule Nd-rich and Y-rich particles and the elimination of microscopic pores. Sorkhi *et al* explored how the microstructure and mechanical characteristics of LPBF-processed WE43 samples were influenced by HIP and T6 treatments [192]. The findings indicated that HIP was effective in decreasing the porosity of WE43 samples to less than 0.1%, whereas T6 could dissolve and precipitate the hard and brittle phase along the grain boundaries, resulting in an 8% enhancement in the EL of WE43. Overall, the specimens treated with HIP and T4 or T6 together demonstrated the most favorable balance of strength and ductility.

4.2.3. *Surface modification.*

Moreover, several of surface modifications have also been used to improve the structure and surface quality of manufactured products, enhancing their mechanical strength, degradability, biocompatibility, antibacterial properties, and anti-inflammatory characteristics. Among them, utilizing high-temperature oxidation (HTO) as an efficient technique for passivation could potentially slow down the degradation process of Mg alloys [184–186, 194]. Liu *et al* investigated the impact of HTO on the microstructure, mechanical characteristics, and biocompatibility of LPBF-processed WE43 alloy [184–186]. Following HTO treatment, the transformation of the metastable β_1 phase in the as-built sample to a stable phase Mg$_{24}$RE$_5$ was observed, alongside the presence of α-Mg and Y$_2$O$_3$ oxides. Besides, a continuous oxide layer (OT) measuring approximately (2.04 ± 0.51) μm in thickness, along with a transition layer (TL) measuring around (74.38 ± 4.77) μm thick, was observed on the matrix's surface, as shown in figures 14(a)–(e). The enhanced

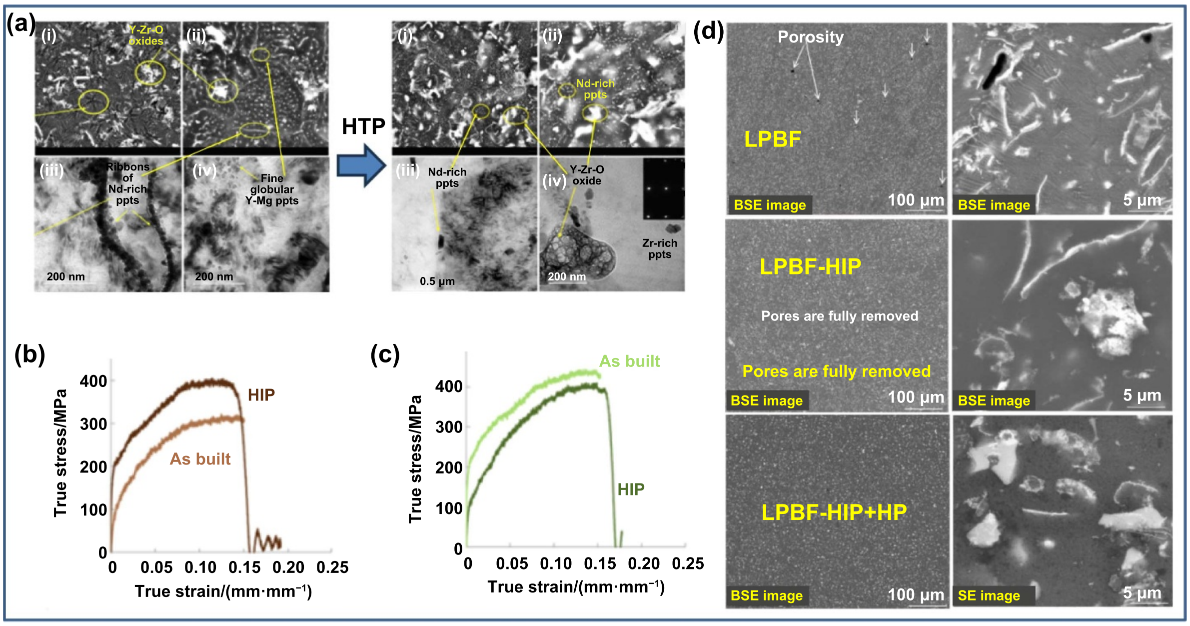

Figure 13. Microstructure evolutions before and after HIP process. (a) Microstructure of the LPBF-processed WE43 at as-built states and HIP states. (b)–(c) Dynamic stress strain curves and the obtained porosity contents at scanning speeds of 1200 mm s^{-1} and 800 mm s^{-1}. Reprinted from [101], © 2020 Elsevier B.V. All rights reserved. (d) The microstructure of the LPBF-processed WE43 at as-built states, HIP states, and HIP + HP states. Reprinted from [183], © 2018 Published by Elsevier B.V.

corrosion resistance is due to the dense oxide layer's improved passivation effect and the transition layer's inhibition of galvanic reactions, as illustrated in figure 14(f). Besides, the oxide layer could enhance surface smoothness, hydrophilicity, and wettability. In general, the lower degradation rate of the HTO sample contributes to its improved biocompatibility, enhancing cell viability, osteogenesis, and reducing hemolysis.

Inherently, deep cryogenic treatment (DCT) also can demonstrate the beneficial effects on the performance of the LPBF-processed Mg alloys [187]. Li *et al* explored the influence of the DCT on the microstructure evolution, mechanical properties, and the related mechanism of the LPBF-processed WE43 alloy [187]. The micro-stress storage strain energy attributed to the lattice shrinkage during the DCT process could reduce the driving force of the precipitation, which further enhanced the hardness strengthening phases' precipitation without destroying the initial metastable phases, including the β'-$Mg_{12}NdY$ and β''-$Mg_3(Y, Nd)$ phases, as shown in figure 14(g). Besides, the growth of subgrain boundaries in the DCT alloy inhibits the movement of partial dislocations, such as slipping and climbing, leading to a combined enhancement in strength and toughness. And the mechanical properties of the LPBF-processed WE43 alloy were improved effectively after the DCT process.

Despite the comparatively high dimensional accuracy of LPBF-processed porous Mg-based scaffold, inevitable dimensional discrepancies exist between the porous molded parts and design specifications. Hence, chemical or electrochemical polishing through immersion is highly preferable. Besides, the deposition of protective coatings by plasma electrolytic oxidation (PEO) is another way to enhance the corrosion resistance [188, 195]. Kopp *et al* proposed that the LPBF-processed WE43 porous scaffold's degradation rate during the early immersion in SBF could be reduced by PEO [188]. Gnedenkov *et al* revealed that the formed protective composite inhibitor-and-polymer-containing layers effectively reduce the corrosion current density of Mg alloys by three orders of magnitude in a 3 wt.% NaCl solution [195]. Therefore, these protective layers show great potential in lowering the risk of implant-related infections.

5. Properties of Mg-based implants

The mechanical characteristics and biological performance of the final implant are significantly affected by various factors, including the internal structure, design geometry, dimensional accuracy, and formation quality. This section offers a comprehensive review and analysis of the mechanical performance, biodegradation performance, and biological properties. By shining a light on these essential factors, a deeper understanding of how they collectively influence the overall performance and successful integration of the device could be obtained.

5.1. Mechanical performance

The microstructure of LPBF-processed Mg alloys differs significantly from that of Mg alloys produced using traditional manufacturing processes, which results in significant variation in their mechanical properties. The mechanical performances of LPBF-processed Mg alloys are summarized in table 3.

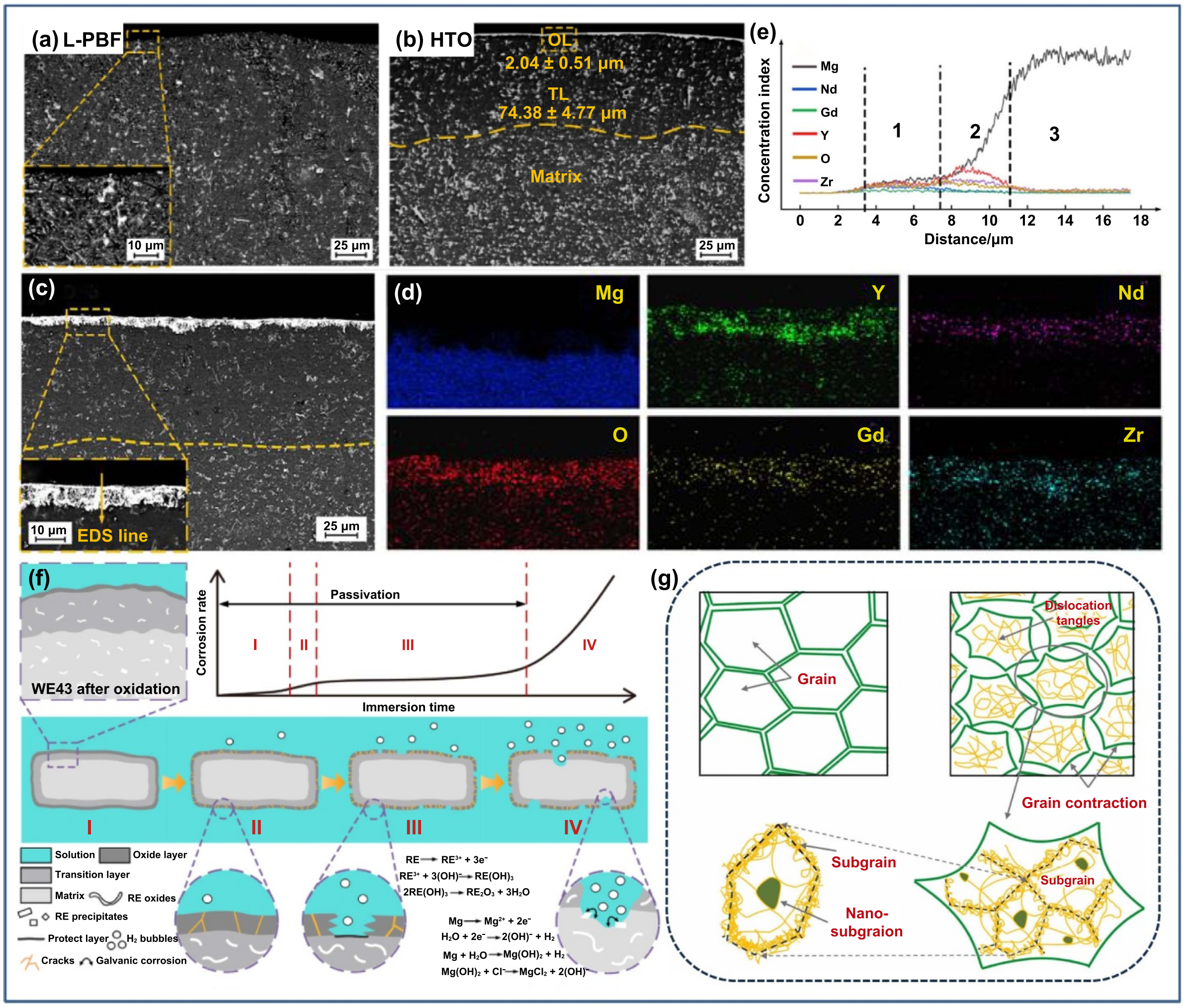

Figure 14. Microstructure characterizations of the LPBF samples. (a)–(c) SEM images at the cross sections of HTO samples. (a), (b). Reprinted from [194],© 2024 Published by Elsevier Ltd on behalf of The editorial office of Journal of Materials Science & Technology. (d)–(e) The element mapping and concentration change of the HTO samples from the oxide layer to the matrix. (f) The corrosion process and mechanism of the HTO samples. (c)–(f) Reproduced with permission from [186]. © 2022 Chongqing University. Publishing services provided by Elsevier B.V. on behalf of KeAi Communications Co. Ltd. CC BY-NC-ND 4.0 (g) The microstructure evolution during the DCT process. Reprinted from [187], © 2023 Elsevier B.V. All rights reserved.

5.1.1. Mechanical strength. The primary purpose of any biomedical implants or scaffolds lies in stabilizing or bolstering fractured bones to withstand specific anatomical pressures during the healing period. That is, the ideal orthopedic implant must possess adequate mechanical strength and compatibility with the surrounding bone tissue, providing essential mechanical support during the healing process of the bone and exhibiting excellent stress conductivity. This necessitates that the mechanical characteristics, including hardness, ability to withstand compression and tension, fracture toughness, stiffness or flexibility, ductility, and fatigue meet the requisite criteria for clinical applications [201]. Generally, the tensile YS of human cortical bone is approximately 53 MPa when measured perpendicular to the bone axis, and ranges from 124 to 174 MPa when measured parallel to the bone axis and the compressive YS varies from 1 to 20 MPa, while the compressive strength is between 103 and 140 MPa [202, 203]. The elastic modulus of cortical bone spans from 1 to 35 GPa. In contrast, the compressive YS of trabecular bone ranges from 2 to 12 MPa, with an elastic modulus between 0.1 and 5 GPa [202, 203]. It is crucial to recognize that the mechanical properties of human bones are significantly influenced by factors such as age, bone health, and bone type.

Unlike conventional biomaterials such as Ti-based alloys, stainless steel, and Co–Cr alloys, Mg-based materials exhibit distinct mechanical features that render them better suited for implantation. Firstly, they offer a superior strength-to-weight ratio, which is advantageous for lightweight implant designs; secondly, their hardness and elastic modulus are much closer to those of human bone, thereby mitigating the risks of 'stress-shielding' effects and bone loss [48, 57, 63, 64, 133, 177]. Moreover, products manufactured through AM techniques tend to demonstrate superior mechanical characteristics such as hardness and tensile strength when compared to those made though conventional approaches with the same chemical composition, mainly attributing to the high

Table 3. Mechanical performances of LPBF-processed Mg alloys.

Alloy	State	YS/MPa	UTS/MPa	EL/%	References
WE43	As-built	276	292	6.1	[116]
	As-built	215	251	2.6	[91]
	T6	219	251	4.3	
	As-built	296	308	11.9	[146]
	As-built	236	313	9.6	[187]
	DCT	275	337	10.5	
AZ91D	As-built	254	296	1.83	[89]
	As-built	265	298	2.0	[159]
	As-built	225	317	6.8	[196]
AZ91D + SiC	As-built	308	345	1.1	[159]
AZ91D + TiCN	As-built	242	361	8.9	[196]
AZ31B	As-built	183	212	7.9	[197]
AZ61	As-built	233	287	3.1	[87]
	T4	124	240	5.9	[198]
	HIPed	126	274	8.2	[190]
ZK60	As-built	137	246	15.5	[191]
	T4	107	224	16.7	
	T6	191	287	14.1	
GZ112K	As-built	332	351	8.6	[144]
	T4	281	311	11.4	
	T6	343	371	4.0	
G10K	As-built	203	271	10.3	[161]
	T5	285	360	2.9	
GWZ1031K	As-built	310	347	4.1	[112]
	T4	255	328	10.3	
	T5	365	381	0.8	
	T6	316	400	2.2	
GWZ1221M	As-built	315	340	2.7	[199]
	T4	247	304	6.9	
	T5	342	356	1.4	
	T6	320	395	2.1	
GZ151K	As-built	345	368	3.0	[200]
	T5	410	428	3.4	

densification and the combined effects of refining grains, dislocation, grain boundaries strengthening, precipitation strengthening, solution strengthening, and hetero-deformation induced (HDI) strengthening [116, 204–206]. Deng *et al* analyzed the grain boundary strengthening effect by comparing the mechanical performance of parts fabricated by LPBF method and those manufactured by casting for Mg–Gd–Zn–Zr alloy [117]. The results indicated that the enhancement from the grain boundary strengthening could boost the strength by 138–196 MPa, accounting for 42.5%–60% of the total strength in the LPBF-processed counterparts. According to the Hall–Petch equation, the strength is inversely proportional to the grain size. Moreover, as discussed above, components produced by LPBF method also have a higher geometrically dislocation density, thus dislocation strengthening is also an important strengthening mechanism in AMed Mg alloys [163, 167, 168, 207]. Chang *et al* found that the dislocation strengthening contribution in the LPBF-processed Mg alloys could reach 55.9 MPa, occupying 18.7% of the overall YS [207]. Generally, the hardness of LPBF-processed bulk Mg alloys ranged from 0.4 to 1.2 GPa, the elastic modulus is 27–35 GPa, and the YS is typically higher than 200 MPa, with some even achieving 350 MPa, making them suitable for a wide range of structural uses. Besides, through the design of the porosity, the stiffness of the regulated porous LPBF-processed Mg alloys is closer to the level of human bone [208]. Generally, the elastic modulus, compressive YS, and compressive strength of porous LPBF-processed Mg-based scaffold range 0.207–0.8 GPa, 4.07–23 MPa, and 13–31 MPa, respectively [133].

Besides, it is worth to note that the mechanical properties of the LPBF-processed Mg alloys were different in different directions, indicating that the AMed counterparts had significant anisotropy. As discussed above, the microstructure of the AMed specimen exhibited anisotropy due to the significant temperature gradient along the building direction [45]. Thus, the LPBF-processed hcp structural metals, such as Mg alloys or Zn alloys, tended to grow in the $<10\bar{1}0>$ direction, resulting in higher strength along the building direction and significant anisotropy of the material properties. Currently, AMed Mg alloys tested for mechanical properties are all sampled in the transverse direction (TD), and data in the longitudinal direction (LD) are limited. Besides, it is worth noting that the changing tendencies of tensile strength and EL in vertical direction and horizontal direction are different in different investigations. Pawlak *et al* found that the average strength and EL of LPBF-processed AZ31B in horizontal direction (UTS = (212 ± 34) MPa, EL = (7.9 ± 2.9)%) were superior to those at a 45-degree angle (UTS = (207 ± 54) MPa, EL = (7.7 ± 6.0)%) to the processing platform plane [197].

5.1.2. Ductility. However, it should be noted that LPBF-processed Mg-based materials possessed relatively lower ductility, mainly attributing to the existence of defects, including very small gas pores and thermal cracks, and the enhanced stress sensitivity caused by the introduction of oxide impurities and high residue stress during the formation process. Generally, a tradeoff between ductility and strength is encountered during the LPBF process. For instance, the tensile strength and YS of LPBF-processed AZ91 were roughly 30% and 50% higher than those of traditionally cast AZ91 alloys, while the ductility of the LPBF-processed specimens (1.24%–1.83%) was approximately 40% lower compared to the cast samples (3%) [54, 89]. Moreover, in Mg alloys like AZ91, WE43, and Mg–Gd alloys, the excessive alloy elements tend to form brittle inter-metallic compounds along the grain boundaries. This brittleness is the key factor leading to localized failures by impeding plastic deformation mechanisms such as grain boundary sliding, slip, and twin transmission. The last but not the least, the sputtered powder or vapor would redeposit on the sample surface, as evidenced by the cauliflower-like appearance on the fractured surface, causing inadequate consolidation or weak bonding in the related part. The EL rates of LPBF-processed AZ91D alloy [87, 89] and AZ61 alloy [87] range from 1.24% to 1.83% and 2.14% to 3.28%, respectively, which are comparatively lower than the EL rates of 3% and 5.2% observed in the die-cast state, respectively.

Wei *et al* studied the fracture patterns of LPBF-processed AZ91D Mg alloy [89]. The fractures displayed a mixed of ductile and brittle characteristics, with dimples, tearing edges, and quasi-cleavage planes observed. Dimples indicate a certain level of plastic deformation prior to fracture. This fracture mode is mainly related to the heterogeneous microstructure and micropores in the alloy. The incompatible crystal structures of the α-Mg matrix (with a close-packed hexagonal structure) and the β-$Mg_{17}Al_{12}$ eutectic phase (featuring a cubic crystal structure) led to the brittleness of the α-Mg/β-$Mg_{17}Al_{12}$ interface. Furthermore, the presence of micropores, high levels of dislocation, and localized stress concentrations at the interface initiated and propagated cracks along the phase boundary. The softer α-Mg matrix favors ductile fractures, while the brittle β-$Mg_{17}Al_{12}$ eutectic phase and micropores cause stress concentration, reducing plasticity and promoting cleavage brittleness. Therefore, restricting the precipitation of $Mg_{17}Al_{12}$ phases is crucial to achieving good plasticity in LPBF-processed Mg–Al alloys. Generally, most AMed Mg alloys exhibit ductility below 5%, with certain alloys lacking any EL capability, which limits their application *in situ*ations with high cyclic load-bearing requirements.

However, Xu *et al* discovered that different laser energy densities could result in varied SEM morphologies of the tensile cross-section fracture, as illustrated in figure 15(a) [116]. When the E_v reached 88 J mm^{-3}, the fracture exhibited numerous microcracks (approximately 80 μm in length) and cleavage steps, indicating a typical brittle fracture. With the increase of E_v, there was a slight rise in gas pore defects resulting from intense evaporation. However, the material's properties showed gradual improvement, as demonstrated by the tensile curves revealing the emergence of numerous equiaxed dimples of various sizes. Notably, samples with an E_v of 138 J mm^{-3} displayed multi-scale dimples of sizes ranging around 50 μm and 2 μm, showcasing a mixed fracture mode combines brittleness and ductility. These dimples primarily resulted from stress concentration around nano-precipitates at the bottom during tensile testing, playing a crucial role in absorbing fracture energy, retarding fracture initiation and bolstering the alloy's ductility.

5.1.3. Fatigue. In addition, human body is not only an aqueous environment but also a severe environment with complex cyclic loading, thus fatigue is also one of the current failure mechanisms that can happen for biomedical implants or scaffolds due to the cyclic stress [209]. As is well-known, fatigue is a progressive, localized, and permanent change in the structure of materials, resulting in the formation of cracks and eventually fractures when subjected to sufficient cyclic loading, which determines the suitability of a material for structural purposes. And the stresses applied typically involve tension or a blend of tension and compression. Theoretically, the absence of any porosity or surface flaws, material failure from fatigue unfolds dramatically as voids emerge from dislocation accumulation and extend until complete rupture. Therefore, various factors may influence the fatigue resistance of the AMed components, including surface properties, like toughness and cleanliness, the morphology, location, dimensions and volume fraction of internal flaws (such as porosity, voids and lack of fusion), defects in the microstructure (e.g. grain boundaries, twinning, and dislocations), grain size, distribution, and morphology of secondary phases, loading profile, and topological design [45, 64, 210, 211]. As a whole, the introduction of any stress concentrators like surface or internal defects can significantly reduce the number of cycles needed for specimen fracture, thereby diminishing fatigue life the LPBF-processed implants or scaffolds. For instance, elongated voids with large,

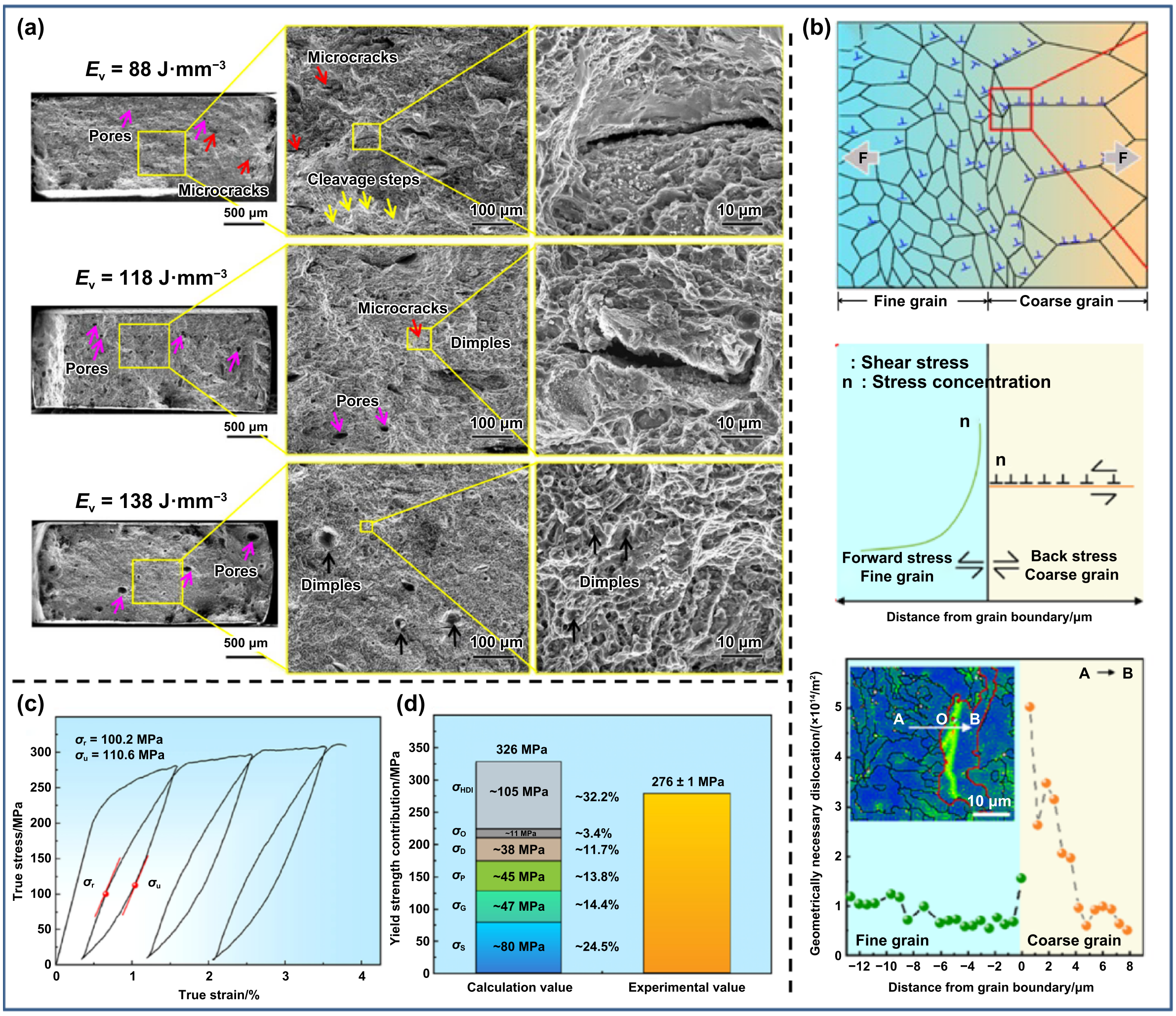

Figure 15. The mechanical properties of the LPBF-processed WE43 alloy. (a) Tensile fracture morphologies at different laser energy densities. (b) Schematic illustration of hetero-deformation induced strengthening mechanism. (c) Stress versus strain curves, and (d) stress-strain curve, and comparison of calculated and experimental values of the yield strength. Reproduced with permission from [116]. © 2024 Chongqing University. Publishing services provided by Elsevier B.V. on behalf of KeAi Communications Co. Ltd.CC BY-NC-ND 4.0.

irregular, and sharp corners, particularly those situated close the surface of counterparts, are the most detrimental type of internal flaws in shortening the fatigue lives of specimens due to the higher stress concentration at the tip of the cracks and the reduced load-bearing capacity [45]. Besides, brittle secondary phases, encompassing the oxides and intermetallic compounds, may serve as the nucleation sites where cracks initiate, leading to their easy propagation into the main matrix phases, particularly when these phases possess irregular morphologies [45].

Unluckily, the dynamic loading in human body, along with the corrosive body fluid, may cause premature loss of mechanical integrity of biodegradable Mg-based implants. Corrosion fatigue is defined as the simultaneous occurrence of an aggressive environment and cyclic stress, which results in the early failure of metals due to cracking [212]. Up to now, only a few fatigue studies on the biodegradation-affected fatigue behavior of bulk Mg alloy counterparts in the simulated body fluid (SBF) [213–215]. In comparison, cracks initiated at microstructural defects or deformation twinning boundaries in bulk pure Mg or Mg alloys when exposed to air, while cracks originated from localized sites or pits in fatigue specimens immersed in SBF [213, 214]. Moreover, Li *et al* pioneered the study on how biodegradation affects the fatigue performance of AMed porous WE43 alloy through the comparative study on fatigue behaviors in air and in a revised SBF (r-SBF) [216]. The study revealed that cracks tended to initiate from tiny degradation pits on the edges of the specimens where tensile stress was concentrated, especially at the structural joints. Subsequently, the cracks propagated through the material, while the dislocations showed increased complexity following the fatigue tests. Under cross action, biodegradation decreased the fatigue strength of the porous material from 30% to 20% of its YS and cyclic loading significantly increased its biodegradation rate. Therefore, to enhance the fatigue properties of LPBF-processed Mg-based counterparts, it is crucial to eliminate the process defects such as pores, oxides formation, and other surface defects.

5.1.4. Regulation of mechanical performance. To tailor the mechanical characteristics of Mg alloys for specific applications, three main methods are commonly used, liking micro-alloying, incorporation of nano-particles, and post-HT procedures. Generally, micro-alloying can significantly improve the mechanical performance of Mg alloys by grain refinement strengthening, precipitation strengthening via the formation of inter-metallic phases along grain boundaries, and solid solution strengthening [152, 217–222]. Shuai *et al* observed that the hardness and compressive strength of Mg alloys increased from (66.7 ± 3.5) HV and (105.3 ± 5.6) MPa in ZK30 alloy to (101.3 ± 6.3) HV and (130.4 ± 8.3) MPa in ZK30-1.0Ag, and from (80.5 ± 1.9) HV and (131.6 ± 3.5) MPa in ZK60 alloy to (105.2 ± 1.9) HV in ZK60-0.8Cu alloy and (158.3 ± 5.1) MPa in ZK60-0.4Cu alloy, respectively [220, 221]. The improvement in compressive strength was credited to the grain refinement strengthening and the precipitated phase strengthening. Nevertheless, the overabundant incorporation of Ag or Cu elements tends to generate a coarser precipitate phase with reduced binding ability at the interface between the magnesium matrix and the precipitated phase, thereby impairing the compressive YS. Besides, it is well-known that the atomic radii of Al and Zn are of the order of 0.11 nm, a value lower than the Mg radius of 0.13 nm. Thus, a lattice distoration occurs when these alloying elements are dissolved into the Mg matrix. For instance, by incorporating a small quantity of Zn, Mg-1Zn alloy achieved its highest tensile strength at 148 MPa and an EL rate of 11% due to the solid solution strengthening effect [152]. While, further addition of Zn content may lead to a reduction in mechanical properties attributed to the deterioration of densification degree and increased defects within the samples. Therefore, a meticulous balance of alloying elements is essential to customize the mechanical characteristics, ensuring the structural integrity and performance of Mg alloys in practical applications. Recently, with the rapid development of artificial intelligence (AI), using machine learning (ML) methods such as Bayesian optimization, generative deep learning, active learning, and inverse design approaches to find the optimal alloy compositions to meet specific performance requirements has become a new focus of research today [223–227].

Moreover, extensive research has been focused on RE-Mg alloys. Most RE elements exhibit high solid solubility in Mg, and the lattice distortion caused by the variance in atomic radii between RE and Mg boosts the strength of Mg matrix. This strengthening mechanism does not necessitate intricate microstructures but elevates the mechanical properties through interactions at the atomic level [116]. In a recent research conducted by Xu *et al*, the LPBF-processed WE43 alloy demonstrated a remarkable combination of strength and ductility under the optimal process parameters ($E_v = 138$ J mm^{-3}), outperforming traditional casting methods and other magnesium alloys [116]. The alloy exhibited a YS of (276 ± 1) MPa, UTS of (292 ± 1) MPa, and an EL at break of (6.1 ± 0.2)%, respectively. The exceptional YS was mainly attributed to the presence of rare-earth elements. Additionally, the contributions of rare-earth element solid solutions (around 24.5%), grain size refinement (approximately 14.4%), and HDI strengthening (roughly 32.2%) were highlighted as crucial factors in enhancing the alloy's mechanical properties, as shown in figures 15(b)–(d).

During solidification, RE also creates stable inter-metallic compounds with Mg matrix, acting as grain boundary pins, restraining grain boundary sliding and impeding dislocation movement, thereby notably improving creep resistance and fatigue performance. More importantly, RE-Mg alloys demonstrate enhanced printing capabilities as RE aid in reducing surface tension in the molten pool, minimizing pore and crack formation, and enhancing wettability to promote better spreading and bonding of molten metal, ultimately increasing inter-layer bonding strength. Moreover, RE elements boost oxidation and heat resistance, crucial for withstanding the repeated heating and cooling cycles in LPBF. These advantageous effects are evident not only in laser printing but also in related processes like laser welding.

Furthermore, the incorporation of various nano-particles into Mg-matrix composites (MMCs), including calcium-phosphate bioceramics, silicon-containing bioceramics, magnesium oxide, and carbon materials, is another crucial strategy for enhancing the mechanical characteristics of Mg alloys by the second phase dispersion strengthens and the inhibition of crack growth [159, 228–235]. Besides, these nano-particles attached to the feedstock powder could act as strong potent nucleation site, resulting in smaller grain size and CET transition [159]. In our previous work [232, 233], the mesoporous bioglass (BG, 1–5 μm, 5 wt.%) and mesoporous bioglass (MBG, 200–400 nm, 5 wt.%) were incorporated into Mg matrix composite of the LPBF-processed ZK60 alloy. The overall strength and hardness of the composite were significantly improved, attributed to the even distribution of the BG-reinforced particles and the refined grain structure. Interestingly, the relationship between the hardness and the quantity of BG particles added was not linear as expected. In the studies conducted by Wits *et al* [234] and Niu *et al* [159], SiC particles were selected as the strengthening component to fabricate SiC/WE43 composites and SiC/AZ91D composites via LPBF technology. The LPBF-processed SiC/WE43 composites exhibited enhanced microhardness and the LPBF-processed SiC/AZ91D composites displayed superior mechanical properties due to the grain refinement and more uniform distributed $Al_{12}Mg_{17}$ precipitates, compared to the AZ91D matrix, with YS values of around 307.5 MPa and UTS values of approximately 345.4 MPa.

In the realm of enhancing the mechanical properties of Mg alloys, several HT methods also come into play, including solid solution treatment (T4), age treatment (T5), and solid solution combined with age treatment (T6) [57, 91, 103, 112, 144, 191, 199]. The primary mechanisms for strengthening during HT involve fine-grain strengthening and second phase strengthening. Notably, T4 leads to an increase in EL but a decrease in YS and UTS, whereas T6 greatly enhances YS and UTS while reducing EL. Deng *et al* found that LPBF-T4 GZ112K alloys displayed YS of approximately (281 ± 6) MPa, UTS of around (311 ± 3) MPa, and EL of approximately (14.4 ± 1.8)% [144]. In comparison, the cast-T4 GZ112K alloys showed YS values of approximately (141 ± 7) MPa, UTS values of around (239 ± 7) MPa, and EL values of approximately (9.8 ± 1.2)%, respectively. On the other hand, the LPBF-T6 GZ112K alloys exhibited YS values of approximately (343 ± 9) MPa, UTS values of around (371 ± 4) MPa, and EL values of approximately (4.0 ± 0.05)%, compared to the cast-T6 GZ112K alloys with values of (171 ± 2) MPa, (267 ± 5) MPa, and (5.7 ± 0.6)%, respectively. Up to now, this LPBF-processed Mg-based alloy boasts the strongest strength among all reported. Besides, as discussed above, ensuring uniformity in the distribution of flaws and microstructure proves advantageous in enhancing fatigue resistance. Therefore, employing a combination of HTs and HIP after processing emerges as an effective approach for enhancing the fatigue properties [45]. As a whole, by skillfully manipulating HT techniques, it is possible to achieve a balance between strength and ductility for Mg alloys.

Last but not least, the mechanical property of AMed porous Mg-based counterparts is also closely linked to their structural design, especially for pore characteristics, including density, morphology, and size [209, 211, 216, 236]. A study conducted by Wang *et al* explored the impact of varied structural configurations, such as biomimetic, diamond, and sheet-gyroid, on the mechanical properties of LPBF-processed JDBM porous scaffolds [133]. The study revealed significant differences in the mechanical performance of these scaffolds. For instance, the sheet-gyroid scaffold exhibited impressive YS of 16 MPa and elastic modulus of 760 MPa, surpassing biomimetic scaffolds by 4 times and 3.5 times, respectively. Moreover, it surpassed diamond scaffolds by over 70% in YS and 60% in elastic modulus. These disparities can be attributed to the distinct deformation behaviors associated with each structural form. While biomimetic scaffolds display an uneven distribution of thick and thin struts, making them prone to fracture at the thin sections, the sheet-gyroid scaffold, characterized by stretch-dominated deformation, demonstrates superior mechanical strength compared to the bending-dominated diamond scaffold.

5.2. Biodegradation performance

5.2.1. Basic corrosion mechanism. For biodegradable Mg alloys, its basic corrosion mechanism involves a self-corrosion driven by its high oxidizing tendencies. This will weaken the structural strength of Mg matrix, creating voids or cracks that accelerate specific area corrosion, further hastening the degradation. Thus, understanding the corrosion behaviors is crucial for developing tailored biodegradable Mg alloys for biomedical applications. The electrochemical corrosion process of Mg alloys in aqueous environments, such as the body, involves the formation of a protective Mg hydroxide layer on the matrix surface. This process is accompanied by the release of hydrogen gas, which can create gas pocket at the tissue-scaffold interface. Such gas pockets may adversely affect tissue healing [47, 56, 232]. When chloride ion levels exceed 30 mMol l^{-1}, the protective $Mg(OH)_2$ layer breaks down, leading to localized film deterioration from $Mg(OH)_2$ and Cl ion interaction, as shown in figure 16(a). Considering the actual human body environment, which includes various molecular proteins, blood, cells, oxygen, etc., the corrosion process of Mg alloy implants is more complex and intricate, due to uncontrollable factors such as dynamic blood flow, tissue in growth, and so on.

According to the theory of electrochemical corrosion kinetics, biodegradable Mg alloys exhibit various corrosion types, including: (i) general corrosion, also called as surface corrosion, where the entire exposed surface undergoes uniformly electrochemical reactions with the environmental medium, resulting in Mg matrix dissolution. (ii) Localized corrosion, which encompasses filamentary corrosion and pitting corrosion. Filamentary corrosion, influenced by varying oxygen concentrations, presents as a strip-like pattern with significant potential discrepancies at its ends (around 0.1–0.2 V). It typically initiates from surface defects or uneven areas and progresses in a specific direction. Pitting corrosion, originating from active sites on the alloy surface, is particularly prominent in Cl ion-containing solutions. Cl ions, due to their small size and high diffusivity, can breach the passive film, react with Mg to form soluble $MgCl_2$, and disrupt the passive film structure, leading to the development of corrosion pits. (iii) Galvanic corrosion occurs when Mg matrix forms a galvanic couple with another phase of lower potential, accelerating the Mg alloys' corrosion as the anode. (iv) Stress corrosion, triggered when Mg alloys experience mechanical stress, significantly reduces their corrosion resistance, potentially resulting in stress corrosion cracking (SCC). Mg–Al alloys, in particular, display high stress corrosion susceptibility even at stress levels below the YS, impacting both corrosion resistance and overall service performance.

Interestingly, in LPBF-processed Mg alloys, a unique 'bulk erosion' mechanism has been observed instead of the typical 'surface corrosion' seen in conventional Mg alloys [162], as shown in figure 17. The distinctive microstructure resulting from LPBF exhibits high chemical reactivity, facilitating rapid fluid penetration, severe local corrosion, and intense micro-galvanic corrosion. The higher dislocation density or local strain in LPBF-processed parts compared to extruded samples puts them in a state of high energy, making them more susceptible to preferential attack, as illustrated in figure 17(a). This results in corrosion rates two orders of magnitude higher than plastic-deformed counterparts. Defect sites on the sample surface are the first to be attacked upon contact with water, with fluid penetrating deeply through interconnected pores, leading to accelerated material degradation. Isolated pores evolve into localized corrosion sites over time, with corrosion spreading rapidly along the pore profile when it encounters a new pore. The corrosion then progresses towards the material core as the loose and porous surface film easily detaches, failing to impede corrosion penetration and sample disintegration, as shown in figure 17(b).

5.2.2. Biodegradation behavior. Currently, the functionality and degradation behavior of Mg-based implants are primarily evaluated through *in-vitro* experiments, as depicted in

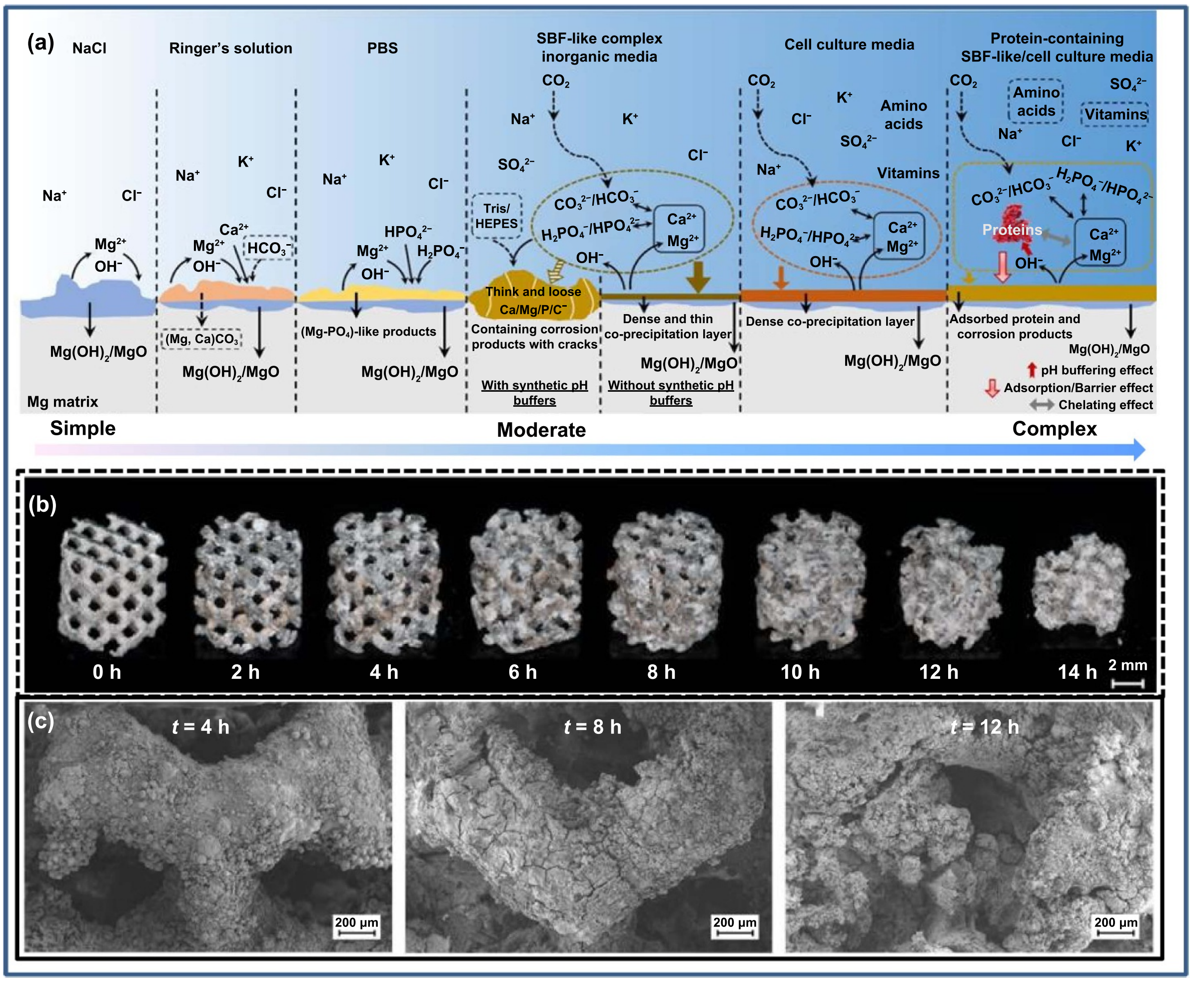

Figure 16. The corrosion mechanism and corrosion behavior of the LPBF-processed Mg alloys. (a) Diagram showing how Mg breaks down in the commonly used media. Reproduced from [56]. CC BY 4.0. (b)–(c) The pictures of Mg porous scaffolds after different periods under the *in vitro* conditions. Reproduced from [237]. CC BY 4.0.

figure 18. The *in-vitro* investigations primarily concentrate on analyzing the biodegradation performance of Mg-based implants in synthetic physiological environments outside the body. For *in-vitro* experiments, several variables, including temperature, pH levels, and different types of ionic impurities, are taken into account to gauge the degradation patterns of Mg-based implants. Table 4 summarizes the corrosion resistance of LPBF-processed Mg alloys *in-vitro*. Additionally, researchers also have conducted numerous *in-vivo* experiments on Mg-based implant in animal models and human subjects to obtain more realistic insights into their deterioration mechanisms and biocompatibility with physiological conditions. It has to point out that there is a significant distinction in the degradation process of Mg alloys between *in-vivo* and *in-vitro* experiments [237]. For instance, an intramedullary Mg_2Ag nail could last for 617 d without significant changes under the *in-vitro* degradation, but it only maintained integrity for 210 d under the *in-vivo* conditions, attributed to various factors present in the *in-vivo* environment [238]. Therefore, more *in vivo* test results are expected to truly evaluate the performance in corrosion resistance performance, as additional *in vivo* studies are crucial for improving clinical application.

Liu *et al* evaluated the degradability of the LPBF-processed WE43 porous scaffolds through both *in vitro* and *in vivo* experiments [56, 184, 185]. The *in vivo* results showed that the stability of the scaffold structure began to disintegrate into tiny fragments following a 12 hour soak in Hank's solution, only last 4 weeks during implantation testing in rabbit femurs. The scaffold structure became unclear with residual fragments visible after a four-week implantation test, indicating significant degradation and structural collapse. During degradation, the pH value and hydrogen volume increased. The presence of hydrogen gas bubbles near the scaffolds was first observed at 4 weeks after the surgery, visible as a white region in the Micro-CT results, and nearly disappeared after 8 and 12 weeks. In essence, it is believed that the degradation rate of WE43 porous scaffolds is considered too rapid for bone reconstruction purposes. Thus, additional measures are deemed essential to regulate the degradation rate of Mg-based scaffolds processed through LPBF. Liu *et al* proposed that HTO could effectively enhance the corrosion resistance [184], as shown in figures 18(a) and (b). The outcomes indicated that the HTO treated scaffold's entire contour morphology remained distinguishable for up to 12 weeks after surgery,

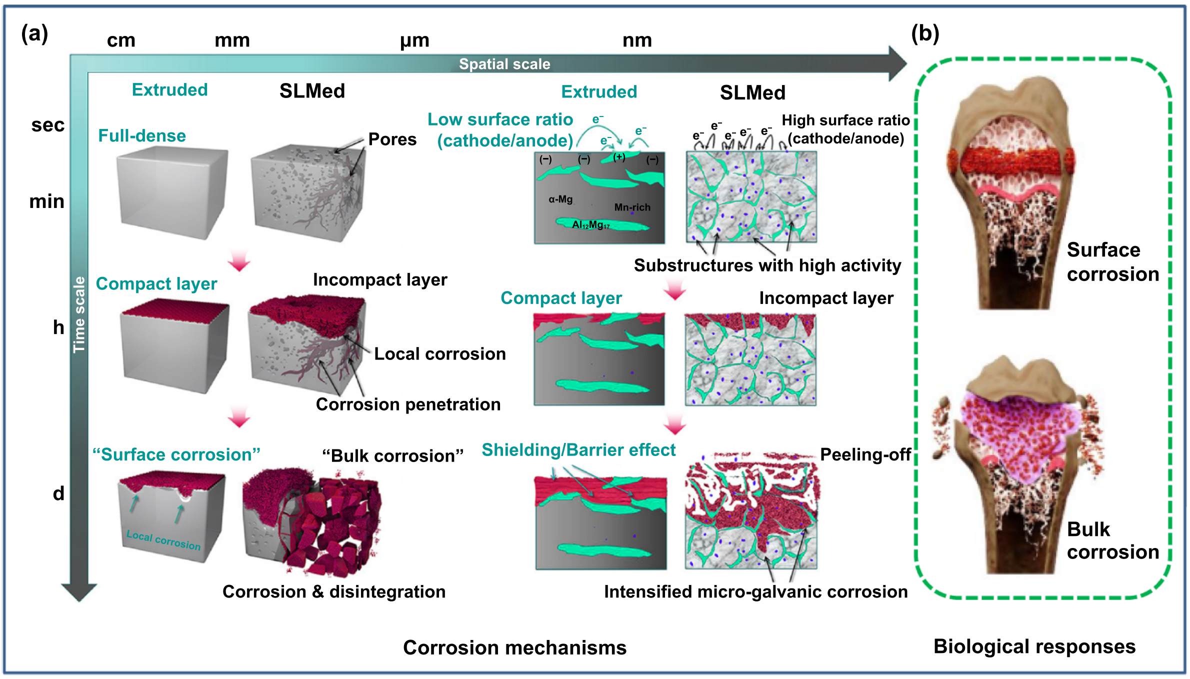

Figure 17. Schematics illustrate the corrosion mechanisms and the resulting biological responses: (a) the spatiotemporal 'bulk erosion' mode in the LPBF-processed samples, compared with the 'surface corrosion' mode in the extruded samples and (b) the consequent resulting cell and tissue response. Reprinted from [162], © 2024 Published by Elsevier Ltd on behalf of The editorial office of Journal of Materials Science & Technology.

as shown in figures 18(c) and (f). Subsequently, a degradation process initiated from the outer layers towards the inner, concurrently promoting enhanced bone regeneration. By the time between 24–48 weeks, the HTO-treated scaffolds completely lost the porous structure and degraded into granular debris gradually. At the same time, the newly-formed bone structure intertwined intricately with the remaining scaffold components, culminating in a firm osseointegration. No obvious signs of inflammatory reactions or collapse were detected from 6 to 48 weeks postoperatively, as illustrated in figures 18(d) and (e).

5.2.3. Regulation of biodegradation.

Although Mg-based biodegradable alloys hold considerable promise in biomedical applications, their implementation faces several challenges. The primary issue is their rapid degradation rate in the presence of bodily fluids, which can lead to premature implant failure and the potential release of harmful by-products. Repairing bone tissue defects generally involves three phases: inflammation, healing, and rebuilding [247]. In the first two phases, adequate support from the bone implant is essential to protect the fracture site from secondary injury; therefore, the implant must exhibit a slow degradation rate to preserve sufficient mechanical stability for at least 24–32 weeks. During the final phase, the impaired bone tissue requires gradual loading to regain its original weight-bearing capability, necessitating the complete decomposition of the bone implant. Typically, tissue engineering scaffolds are required to maintain mechanical strength for 3–6 months, with a degradation rate of less than 0.2 mm yr^{-1}; vascular stents need to provide support for 9–12 months, with an initial degradation rate of less than 0.1 mm yr^{-1}, and fully degrade within 1–2 years [11, 248]. Additionally, as degradation progresses, significant amounts of hydrogen gas may be generated, resulting in poor vascularization and the development of detrimental gas pockets. Moreover, the interaction of mechanical stress and a corrosive environment may induce SCC, which further accelerates the degradation of Mg alloys.

Technically speaking, the biodegradation performance of LPBF-processed Mg alloys relies on the choice of materials, design, and production methods. Organizationally speaking, the degradation performance of LPBF-processed Mg alloys depends on the factors, such as lattice defects (e.g. deformation twins, grain boundaries, and dislocation density), homogenous/heterogeneous microstructure, phases morphology, phases distribution, phases fraction, the grain size of phases, residual stresses associated with imperfections [2, 48, 62, 64, 177, 249]. Moreover, the degradation speed of Mg alloys even can be affected by the adsorption of lipids, proteins, and amino acids on the surface [27]. Therefore, managing the degradation speed of Mg-based implants can be accomplished by utilizing different methods. Usually, alloying treatment, surface modification, post-treatment, the composite manufacturing via introducing reinforcements, or geometrical design could serve as effective strategies to regulate the degradation rate of Mg alloys [250, 251].

In general, selecting the appropriate amount of nontoxic elements such as Ag, Cu, Al, Mn, Zn, Zr, Ca, and RE [251–254] can boost the ability of Mg-based implants to resist

Table 4. Summary of the biodegradation performance of LPBF-processed Mg alloys.

Alloy	Process parameters	Solution	E_{corr}/V	I_{corr}/(mA cm^{-2})	Corrosion rate/(mm yr^{-1})	References
Mg	$P = 70$ W, $v = 500$ mm min^{-1}, $s = 30$ μm	Hank	-1.52	74.0×10^{-3}	2.8	[156]
Mg	$P = 75$ W, $v = 15$ mm min^{-1}, $s = 70$ μm	SBF	-1.70	29.21×10^{-3}	0.67	[150]
Mg-0.4Mn			-1.58	22.08×10^{-3}	0.50	
Mg-0.8Mn			-1.54	10.18×10^{-3}	0.23	
Mg-1.2Mn			-1.44	28.25×10^{-3}	0.65	
Mg-1.6Mn			-1.42	37.82×10^{-3}	0.86	
WE43	$P = 175$ W, $v = 800$ mm min^{-1}, $s = 90$ μm	SBF	-1.59	—	1.30	[239]
ZK30	—	Hank	-1.56	64×10^{-3}	1.5	[240]
ZK30	$P = 80$ W, $v = 200$ mm min^{-1}, $s = 0.1$ mm	SBF	-1.57 ± 0.02	$(131 \pm 14) \times 10^{-3}$	—	[155]
ZK30-1Al			-1.58 ± 0.02	$(68 \pm 6) \times 10^{-3}$	—	
ZK30-3Al			-1.60 ± 0.03	$(24 \pm 6) \times 10^{-3}$	—	
ZK30-5Al			-1.61 ± 0.02	$(156 \pm 26) \times 10^{-3}$	—	
ZK30-7Al			-1.66 ± 0.03	$(340 \pm 28) \times 10^{-3}$	—	
ZK30	$P = 70$ W, $v = 500$ mm min^{-1}, $s = 80$ μm	SBF	-1.57	0.10	3.7 ± 0.10	[204]
ZK30-0.3GO			-1.59	0.33	10.8 ± 0.09	
ZK30-0.6GO			-1.65	0.10	3.38 ± 0.07	
ZK30-0.9GO			-1.51	0.49	15.64 ± 0.13	
ZK30	$P = 70$ W, $v = 15$ mm s^{-1}, $s = 80$ μm	SBF	-1.64 ± 0.04	$(109.6 \pm 4.5) \times 10^{-3}$	2.39 ± 0.22	[221]
ZK30-0.25Ag			-1.52 ± 0.05	$(81.1 \pm 4.2) \times 10^{-3}$	1.77 ± 0.15	
ZK30-0.5Ag			-1.53 ± 0.03	$(64.5 \pm 4.5) \times 10^{-3}$	1.41 ± 0.13	
ZK30-0.75Ag			-1.54 ± 0.02	$(74.3 \pm 3.5) \times 10^{-3}$	1.62 ± 0.16	
ZK30-1.0Ag			-1.56 ± 0.03	$(120.2 \pm 6.7) \times 10^{-3}$	2.62 ± 0.25	
Mg-5Ag	$P = 200$ W, $v = 900$ mm s^{-1}, $s = 100$ μm	SBF	—	—	0.472 ± 0.007	[241]
ZK30	$P = 70$ W, $v = 15$ mm s^{-1}, $s = 50$ μm	SBF	-1.52	17.8×10^{-3}	0.41	[153]
ZK30-0.1Cu			-1.51	28.2×10^{-3}	0.64	
ZK30-0.2Cu			-1.48	38.0×10^{-3}	0.87	
ZK30-0.3Cu			-1.46	47.8×10^{-3}	1.09	
ZK30-0.2Cu	$P = 80$ W, $v = 200$ mm min^{-1}	SBF	-1.578	29×10^{-3}	0.7	[151]
ZK30-0.2Cu-0.4Mn			-1.576	18×10^{-3}	0.4	
ZK30-0.2Cu-0.8Mn			-1.53	12×10^{-3}	0.3	
ZK30-0.2Cu-1.2Mn			-1.52	32×10^{-3}	0.7	
ZK30-0.2Cu-1.6Mn			-1.49	40×10^{-3}	0.9	
ZK30-10Gd	$P = 150$ W, $v = 800$ mm s^{-1}, $s = 0.1$ mm	SBF	-1.559	27.73×10^{-3}	1.323	[242]
ZK30-10Gd-0.3Mn			-1.5445	22.47×10^{-3}	0.966	
ZK30-10Gd-0.6Mn			-1.514	16.22×10^{-3}	0.798	
ZK30-10Gd-0.9Mn			-1.574	29.99×10^{-3}	1.428	
ZK30-10Gd-1.2Mn			-1.578	33.12×10^{-3}	1.617	
ZK60	$P = 60$ W, $v = 600$ mm min^{-1}, $s = 100$ μm	SBF	-1.612	4.420×10^{-2}	1.01	[220]
ZK60-0.2Cu			-1.584	6.039×10^{-2}	1.05	
ZK60-0.4Cu			-1.577	8.542×10^{-2}	1.12	
ZK60-0.6Cu			-1.570	4.857×10^{-2}	7.8	
ZK60-0.8Cu			-1.557	8.275×10^{-2}	14.01	

(Continued.)

Table 4. (Continued.)

ZK60	$P = 80$ W, $v = 120$ mm s^{-1}, $s = 0.06$ mm	SBF	−1.44	105×10^{-3}	0.89 ± 0.22	[233]
ZK60-BG			−1.32	20.1×10^{-3}	0.52 ± 0.11	
ZK60-MBG			−1.35	18.5×10^{-3}	0.31 ± 0.13	
AZ61-GO	$P = 72$ W, $v = 22$ mm s^{-1}	SBF	-1.53 ± 0.02	$(59 \pm 3) \times 10^{-3}$	1.24	[182]
AZ61-TiO_2/GO			-1.57 ± 0.03	$(32 \pm 2) \times 10^{-3}$	0.09	
AZ61-TiO_2-GO			-1.53 ± 0.02	$(44 \pm 2) \times 10^{-3}$	1.15	
AZ61	$P = 120$ W, $v = 10$ mm s^{-1}, $s = 80$ μm	SBF	−1.45	41.4×10^{-3}	1.72	[243]
AZ61-0.25Ti			−1.43	26.3×10^{-3}	1.5	
AZ61-0.5Ti			−1.4	9.2×10^{-3}	1.16	
AZ61-0.75Ti			−1.41	31.6×10^{-3}	0.55	
AZ61-1.0Ti			−1.41	56.5×10^{-3}	0.82	
AZ61	$P = 90$ W, $v = 600$ mm s^{-1}, $s = 70$ μm	SBF	−1.62	159.36×10^{-3}	1.55	[154]
AZ61-0.6Ce			−1.56	56.33×10^{-3}	0.66	
AZ61-1.2Ce			−1.47	12.5×10^{-3}	0.21	
AZ61-1.8Ce			−1.50	40.5×10^{-3}	0.40	
AZ61-2.4Ce			−1.58	88.7×10^{-3}	0.91	
AZ61	$P = 120$ W, $v = 10$ mm s^{-1}, $s = 80$ μm	SBF	−1.5	77×10^{-3}	3.46	[244]
AZ61-6MgF_2			−1.52	65×10^{-3}	1.52	
AZ61-12MgF_2			−1.65	58×10^{-3}	1.47	
AZ61-24MgF_2			−1.58	42×10^{-3}	1.38	
AZ61-48MgF_2			−1.48	105×10^{-3}	1.22	
AZ61	$P = 80$ W, $v = 15$ mm s^{-1}	SBF	-1.50 ± 0.02	$(59 \pm 3) \times 10^{-3}$	1.45	[245]
AZ61-1.0RGO/MgO			-1.47 ± 0.02	$(199 \pm 12) \times 10^{-3}$	2.19	
AZ61-2.0RGO/MgO			-1.48 ± 0.03	$(132 \pm 8) \times 10^{-3}$	1.99	
AZ61-3.0RGO/MgO			-1.48 ± 0.05	$(42 \pm 2) \times 10^{-3}$	1.05	
AZ61-4.0RGO/MgO			-1.48 ± 0.02	$(105 \pm 4) \times 10^{-3}$	1.32	
AZ61	$P = 80$ W, $v = 15$ mm s^{-1}	SBF	-1.54 ± 0.02	$(50 \pm 4) \times 10^{-3}$	1.21 ± 0.09	[246]
AZ61-0.2GO			-1.54 ± 0.02	$(89 \pm 12) \times 10^{-3}$	2.03 ± 0.27	
AZ61-0.4GO			-1.52 ± 0.03	$(212 \pm 16) \times 10^{-3}$	4.84 ± 0.36	
AZ61-0.6GO			-1.57 ± 0.02	$(118 \pm 13) \times 10^{-3}$	2.67 ± 0.30	
AZ61-0.8GO			-1.51 ± 0.02	$(85 \pm 6) \times 10^{-3}$	1.94 ± 0.14	
AZ61-1.0GO			-1.56 ± 0.02	$(35 \pm 3) \times 10^{-3}$	0.76 ± 0.07	
AZ61-1.2GO			-1.53 ± 0.02	$(135 \pm 15) \times 10^{-3}$	3.08 ± 0.34	

P: laser power; v: scanning speed; s: hatching space.

corrosion, affecting both its biocompatibility and mechanical properties, by optimizing grain size and forming the inter-metallic phases that can dissolve within grain matrix or distribute along the grain boundary. However, excessive addition of these elements might lead to accelerated galvanic and pitting corrosion due to the formation of more secondary precipitate phases. Additionally, some studies suggest that grain boundaries could serve as crystallographic flaws and resultantly raises Mg corrosion [255, 256]. Shuai *et al* found that the rate of corrosion for ZK30-xAg ($x = 0.25$, 0.5, 0.75, 1 wt%) alloy initially decreased from (109.6 ± 4.5) μA cm^{-2} of ZK30 to (74.3 ± 3.5) μA cm^{-2} of ZK30-0.75Ag and then tend to be adversely affected with increased Ag content [221]. Hence, the harmony of grain refinement and formation of secondary phases is crucial to achieve optimal resistance to corrosion, ensuring that the content of additives remains within the optimal range.

Moreover, the surface modification, like polymer coating, electrochemical deposition, chemical conversion, and micro-arc oxidation, is another promising approach way to customize the characteristics of the Mg-based implant's surface, decrease hydrogen release, reduce initial pit formation, thus resulting in slower biodegradation rate [184, 228, 257]. One of the most popular approaches for surface modification technique is the application of protective deposit coatings compatible with biological systems, such as polylactic acid, calcium phosphate,

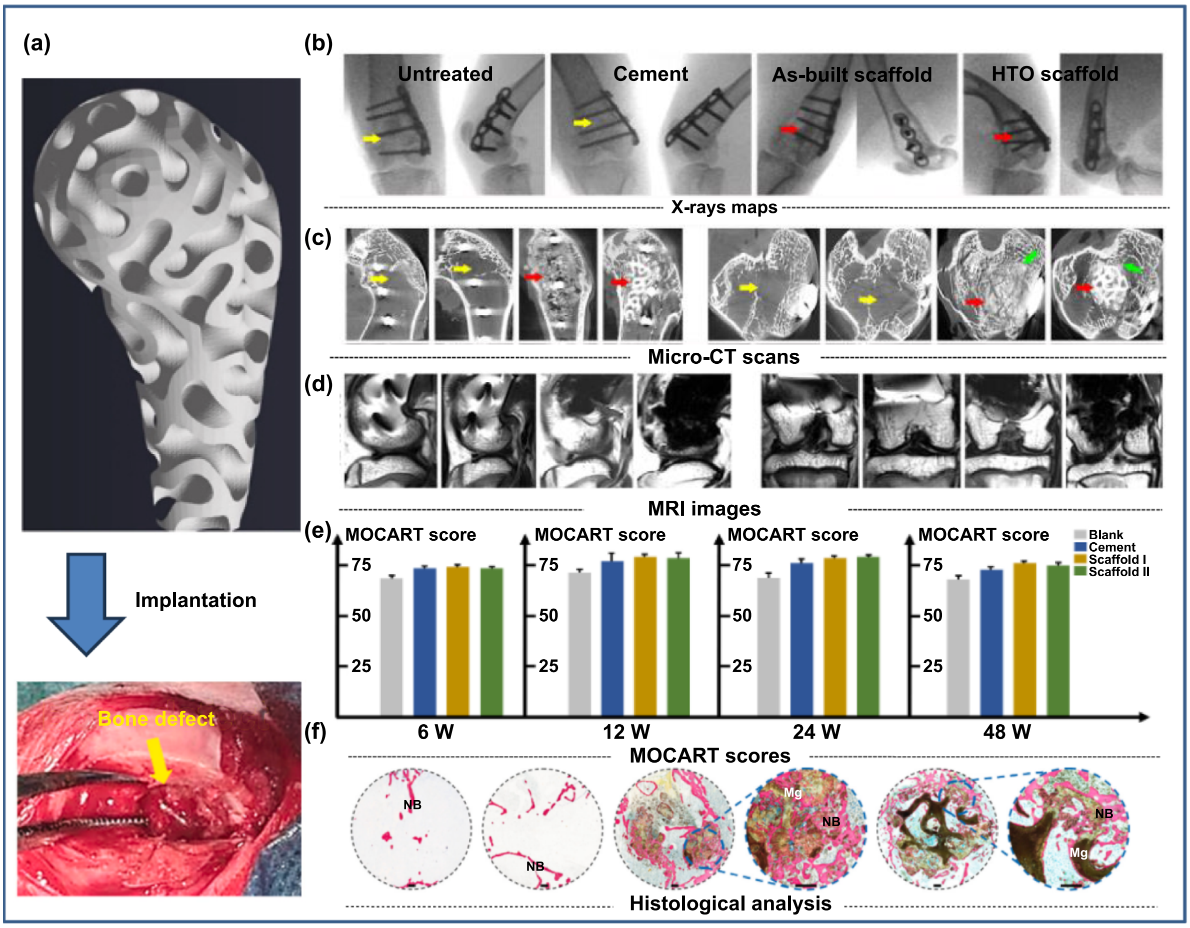

Figure 18. The *in-vivo* implantation of the HTO-treated Mg-based scaffold: (a) the implantation schematic. (b) X-ray maps, (c) the Micro-CT images, (d) MRI images, (f) histological analysis of different groups at 12 weeks, and (e) the MOCART scores of different groups at 6, 12, 24 and 48 weeks after surgery. Reproduced with permission from [185]. © 2023 The Authors. Publishing services by Elsevier B.V. on behalf of KeAi Communications Co. Ltd. CC BY-NC-ND 4.0.

and hydroxyapatite, to decrease the rate of degradation of Mg alloys without compromising biocompatibility during the initial phase [230, 258–260]. For instance, a calcium hydrogen phosphate dehydrate was utilized on the surface coating of JDBM porous scaffolds containing helical tetrahedral structural units, resulting a decrease in corrosion rates and enhancement of biocompatibility [261]. Similarly, a hydroxyapatite protective coating on AZ91 alloy through an electrophoretic deposition process was implemented, resulting in significantly enhanced corrosion resistance and biological properties [160]. These coating substances even have the potential to facilitate the growth of bones and enhance the bonding between implants and the surrounding tissue while undergoing degradation. Furthermore, enhancing the polished surface is another effective method to enhance the ability to resist corrosion by reducing hydrogen release and minimizing the formation of initial large pits. Recently, series studies demonstrated that HTO treatment could significantly optimize the degradation behavior of LPBF-processed WE43 alloys [184–186]. The excellent degradation behavior of the HTO group can be attributed to the oxidation of RE elements when WE43 is heated at high temperatures in air. These RE elements preferentially oxidize compared to Mg and subsequently diffuse to the surface, forming a dense oxide layer. Simultaneously, this outward diffuse of RE elements creates a transition layer between the innermost matrix and the outer oxide layer, which contains minimal Mg-RE secondary phase, effectively inhibiting the galvanic couple reaction.

Besides, some investigations point out that post-processing treatment, including HT and HIP, not only influences the mechanical characteristics but also exerts a significantly influence the corrosion resistance of LPBF-processed Mg alloys [101, 189, 193, 262]. Optimized HT, such as homogenization treatment, solution treatment, and aging treatment, is instrumental in eliminating residual stress, decreasing intragranular segregation, reducing the precipitation of secondary phase, thereby achieving desired microstructure and improving the corrosion resistant [2]. HIP stand out as the most effective post processing techniques for closing pores and increasing the density of Mg alloys [101, 193]. This process significantly enhances the homogeneity of the microstructure and, consequently, improves the material's corrosion resistance. In our previous work, we discovered that the β(Mg,Zn)$_3$Gd phases transformed into plate-shaped

14H-LPSO during the HT process, which were uniformly distributed within the grains and exhibited different orientations relative to adjacent grains [189]. Compared to the β-$(Mg,Zn)_3Gd$ phase, the LPSO phases showed a minor potential difference with α-Mg, resulting in reduced micro-galvanic corrosion. Additionally, the formation of Gd_2O_3 in the corrosion product layer enhanced the integrity and compactness of the corrosion film. Consequently, the LPSO-reinforced Mg–Zn–Gd alloy tended to expand laterally during corrosion evolution, leading to uniform degradation with a significantly reduced degradation rate. Shuai *et al* demonstrated that a dense LPSO structure leads to the formation of a uniform and compact film of degradation products by providing substantial sites for nucleation [242]. This protective film effectively isolates the Mg matrix from the corrosive environment, thereby preventing further deterioration. Furthermore, inhibiting the precipitation of the $(Mg,Zn)_3Gd$ phase can reduce galvanic corrosion, ultimately enhancing the corrosion resistance. However, Åhman *et al* observed a higher corrosion rate of the LPBF-processed Mg–Y–Nd–Zr alloy following the HIP process [193]. They attributed the decreased corrosion resistance to the growth of secondary phases and increased grain size during HIP, which lead to enhanced micro-galvanic corrosion. They suggested that the size and distribution of secondary phases are more critical than achieving a fully dense material.

Last but not least, the geometrical design, including porosity, pore size, curvature, permeability, diffusivity, and pore interconnectivity, on Mg alloy scaffolds also influence the degradation behavior [2, 211, 216, 263, 264]. Owing to the design freedom provided by AM, various porous structures such as body-centered cubic (BCC) [56, 157, 188], diamond [48, 56, 216, 265], and triply periodic minimal surfaces (TPMSs) [99, 211, 266, 267], as well as some functionally graded porous structures [208], were employed in the design of AM porous Mg alloys. For instance, three different porous structures were created using biomimetic, diamond, and sheet-gyroid unit cells, which were then subjected to LPBF-processed Mg–Nd–Zn–Zr alloy [211]. The research indicated that the sheeted-gyroid scaffold demonstrated the least structural deterioration and exhibited a relatively uniform degradation mode during the SBF immersion test. This suggests that geometrical design could serve as a promising approach in developing desirable bone substitutes for treating critical load-bearing defects. However, it is noticed that there are inherent connections and even conflicts among these factors regarding mechanical and corrosion properties since biodegradability complicates the influence of these factors on performance [2]. For instance, increasing porosity may improve biological performance but significantly reduces mechanical strength and corrosion resistance. Thus, determining the optimal porous structure design for the implant is crucial. The conventional CAD-based approach for designing porous scaffolds is often inefficient and involves considerable experimentation to find an optimal design that balances performance. In contrast, technologies like topology optimization (TO) [268–270] and AI, particularly ML [271–274], can rapidly identify the optimal design for porous structures that meets multiple goals and constraints simultaneously. These methods provide distinct benefits for designing functional structures with tailored properties. Natural bone tissues display varying elastic moduli influenced by factors like age and location, necessitating the targeted design of porous orthopedic implants that match the corresponding elastic modulus while ensuring maximum mechanical strength to prevent fractures or fatigue during implantation. Thus, Peng *et al* successfully integrated active learning ML algorithms with finite element simulations, allowing for the iterative refinement of Lattice-Gyroid porous frameworks by adjusting the porosity of each unit [271]. Following six cycles of ML optimization, the resulting structures exhibited a remarkable over 20% enhancement in YS, highlighting the potential of ML in addressing multi-objective structural optimization challenges. Despite recent advancements, the design of LPBF-processed porous Mg alloys remains in its infancy. This limitation largely stems from the underdeveloped research on LPBF-processed magnesium scaffolds, coupled with the unique design challenges posed by their degradability [2].

5.3. *Biocompatibility and osteoinductive properties*

Among all the potential biodegradable implant materials, the biocompatibility of Mg alloys stands out as an indispensable and pivotal characteristic. The key determinants impacting the biocompatibility of degradable metals encompass the properties of chemicals and resultant degradation products. Although Mg plays a vital role in human physiology, contributing to the stability of RNA and DNA, cellular growth and specialization, as well as bone regeneration, its application in implants remains constrained due to the significant challenge of achieving 'appropriate host response' [27]. This is primarily due to its inherent susceptibility to corrosion. As Mg alloys undergo rapid degradation, substantial quantities of $(OH)^-$ions, excessive Mg^{2+} ions, and ions of other alloying elements were released into the surrounding environment, resulting in an elevated pH levels and osmotic pressure with the culture medium, which negatively impacts cell survival and biocompatibility. Furthermore, the excessive release of hydrogen gas hampers tissue healing processes, leading to the formation of calluses and cortical defects [251]. The cytotoxic effect, which is characterized by a reduction in cell viability of over 30% through cellular culturing [275], serves as a common indicator for assessing biocompatibility.

For LPBF-processed block degradable Mg-based implant, the overall biocompatibility is comparable to traditional implants. As for LPBF-processed porous Mg-based implant, a notable advantage lies in the fact that the pores within the scaffold structure can serve as pathways for nutrient transportation and waste removal, promoting the growth of new tissues. An enhanced cell proliferation could discover in the LPBF-processed WE43 scaffolds due to the elevated surface-to-volume ratio [157]. However, it is noted that the geometric features and microstructure of LPBF-treated porous degradable Mg-based implants differ from those conventional block implant, resulting in distinct biodegradation patterns that can influence cellular responses either directly or indirectly [32, 48, 56, 263–265].

Xie *et al* first evaluated the biocompatibilities and osteoinductivity of the LPBF-processed JDBM porous scaffolds through both *in vitro* and *in vivo* experiments [265]. The MC3T3-E1 and RAW 264.7 cells were cultured in the presence of various extract concentration (100%, 50%, 25%, and 12.5%, respectively) for 1, 3, 5, and 7 d to assess the potential toxicity of the LPBF-processed JDBM (Mg-3.16Nd-0.18Zn-0.41Zr) implant. Overall, it was observed that the extracts at 50%, 25%, and 12.5% concentrations did not hinder cell viability, induce cell death, or alter cell morphology, which indicated that the LPBF-processed JDBM implants exhibited favorable biocompatibility. ALP staining and alizarin red staining demonstrated that 25% and 12.5% of the sample extract significantly boosted the osteogenic differentiation of MC3T3-E1 cells at an earlier stage and promoted the formation of calcified nodule after 21 d of culture, suggesting that LPBF-processed JDBM implants possess potential osteogenic properties. Besides, the initial *in vivo* biological behavior and antibacterial features of Mg-based porous structures was conducted through blood tests, histological evaluation, and measurements of Mg^{2+} deposition in a rabbit model. Blood tests and HE staining indicated that there were no abnormalities in hepatic and renal functions or pathological changes in the major organs, including the heart, liver, spleen, lungs, and kidneys, suggesting the biosafety of LPBF-processed JDBM implants.

Similarly, Liu *et al* evaluated the biocompatibility and osteogenic effects of the LPBF-processed WE43 porous scaffolds through both *in vitro* and *in vivo* experiments [56]. Bone mesenchymal stem cells were cultured in the Dulbecco's modified eagle medium of 1, 3 and 7 d to evaluate the cell viability and proliferation. Generally, the cells were widely distributed and in a healthy fusiform shape, confirming a favorable biocompatibility of LPBF-processed WE43 alloy. Comparing different groups over the course of the implantation period, there were no significant alterations in the levels of ALT, UREA and Mg^{2+} concentration as indicated by the continuous blood biochemistry, which verified the *in vivo* nontoxicity and excellent histocompatibility of the LPBF-processed WE43 scaffolds. Furthermore, the sectioning results of vital organs showed no signs of tissue damage at different time points. This included the absence of congestion or ischemia, structural disorders, inflammatory cell infiltration, and necrosis or apoptosis in the brain, heart, liver, spleen, lungs, and kidneys. Accompanied with the gradual degradation of LPBF-processed WE43 scaffold, new trabecular bone grew around in the early stage, and then increasingly grew inside the degraded scaffold. The Micro-CT results confirmed the enhanced osteogenic effect of WE43 scaffolds 8–12 weeks post-surgery.

Moreover, various types of coatings on LPBF-processed Mg-based component have exhibited effective corrosion resistance and improved biocompatibility. For instance, biodegradable ceramics and polymers including polylactic acid, polyglycolic acid, hydroxyapatite, polycaprolactone and tricalcium phosphate are usually utilized as reinforcements to promote biocompatibility and facilitate bone regeneration [276]. Wang *et al* discovered that a porous Mg–Nd–Zn–Zr (JDBM) scaffolds, combined with a coating of tricalcium phosphate, demonstrated reduced degradation rates and enhanced biocompatibility [261]. This improvement was attributed to the presence of a $CaHPO_4.2H_2O$ layer that was applied onto the scaffold surface, acting as an effective barrier separating the substrate from the corrosive surroundings, thus improving the material's ability to resist corrosion. Additionally, another surface modification method is the roughening of the surface, facilitating cell adhesion and promoting tissue growth by enlarging the functional surface area of implants. Nevertheless, maintaining the optimal surface durability is crucial to achieving a trade-off between the benefits of enhanced biocompatibility and the potential drawbacks of accelerated biodegradation, since excessive roughness can result in higher corrosion rates.

The last but not the least, the degradation and biocompatibility characteristics of LPBF-processed Mg-based scaffolds could be customized by the porous configurations and post treatment processing, which further influenced the osteogenic differentiation of bone marrow mesenchymal stem cells and the regeneration of bone tissues [103, 184, 185, 257, 258, 263–265]. Wang *et al* conducted a comprehensive characterization and comparison of the mechanical properties, biocompatibility, degradation behavior, and osteogenic capabilities of LPBF-processed Mg-based porous scaffolds with varying pore sizes (referred as P500, P800, and P1400) and pore structure, such as diamond, sheet gyroid, and body-centered (referred as DIA, SG, and BCC, as shown in figure 19(d)) in both *in vitro* and *in vivo* settings [263, 264], as depicted in figure 19. Both experiments *in vitro* and *in vivo* indicated that LPBF-processed WE43 scaffolds promoted survival of mesenchymal stem cells without inducing any local toxicity, as shown in figures 19(a), (b), (e) and (f). After 4 weeks recovery period from surgery in a rabbit femoral condyle defect model, the distinct visibility of the porous scaffold's structure remained intact, indicating minimal degradation and maintenance of structural integrity, as shown in figure 19(c). Besides, in the rabbit femoral condyle defect model, the P500, SG, and BCC groups exhibited enhanced differentiation of bone mesenchymal stem cells and exceptional ability to promote new bone generation. This enhanced performance can be attributed to the larger specific surface area, highlighting significant potential for application in bone defect regeneration therapy.

6. Conclusions and future researches

Biodegradable Mg alloys hold great promise as implant materials in the biomedical field, because of their biodegradability and biocompatibility. LPBF emerges as a suitable technique for producing biodegradable Mg alloy implants, as it enables precise control over intricate geometric shapes and intricate porous structures based on customized design derived from clinical needs. This paper provided an overview of the

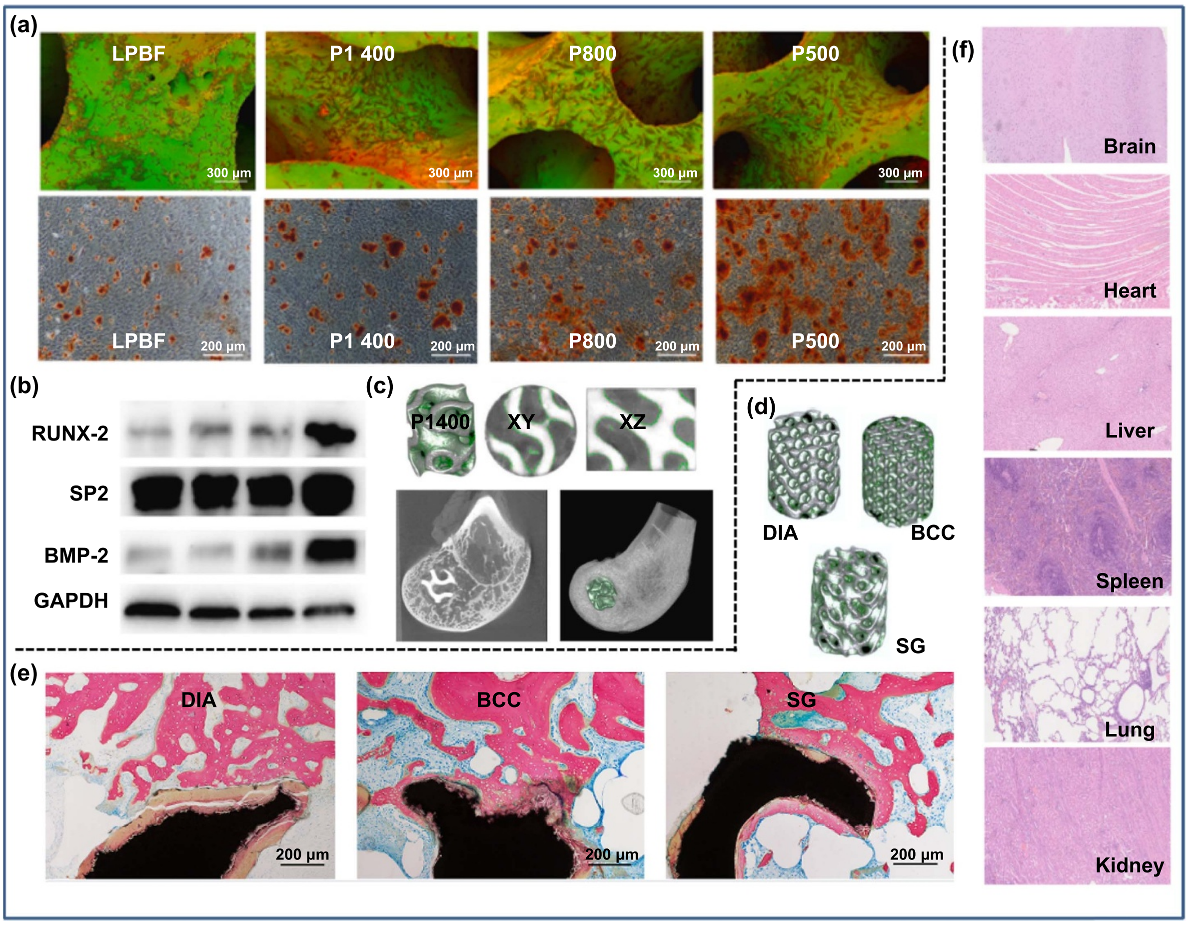

Figure 19. The *in-vivo* degradation behaviors of the LPBF-processed Mg-based scaffold with varied pore sizes and structures. (a) *In vitro* cell proliferation test and (b) osteogenic differentiation test of scaffolds with varying pore sizes. (c) Micro-CT scans of the distal femur 4 weeks after implantation of the magnesium scaffolds (P1400). Reproduced with permission from [263]. © 2023 The Authors. Publishing services by Elsevier B.V. on behalf of KeAi Communications Co. Ltd. CC BY-NC-ND 4.0 (d) 3D reconstructed micro-CT images and, (e) methylene blue/acid fuchsin staining of region of interest (ROI) at 4 weeks of scaffolds with varying pore structures, and (f) HE staining on organs in different groups (DIA). Reproduced with permission from [264]. © 2024 Chongqing University. Publishing services provided by Elsevier B.V. on behalf of KeAi Communications Co. Ltd. CC BY-NC-ND 4.0.

advancements in LPBF of biodegradable Mg alloys for biomedical application. It discussed the influence mechanism of process parameters on the microstructure and performance. Particularly, the correlation criteria between microstructure, degradation behavior, and biocompatibility are comprehensively described. Despite notable advancements in recent years, the current development stage is still in its early phase. More future research is expected to achieve breakthroughs in the following areas, as illustrated in figure 20, so as to promote its clinical application.

(1) In materials terms, it is important to design new Mg alloy systems dedicated to LPBF with good biocompatibility, excellent mechanical properties and controllable degradation rate. Current commercial Mg alloys, including WE43, ZK60 and AZ61, were originally designed as structural materials, and their biological performance, especially degradation rate, still falls short of clinical requirements. Moreover, the evaporation and burning of Mg during LPBF alter the chemical composition, leading to significant discrepancies between the printed parts and the initial powder. Traditional ‘trial-and-error’ methods are inadequate for quickly and accurately identifying performance-tuning rules, resulting in prolonged development cycles for new materials. However, recent advancements in programs like ‘materials genome engineering’ and ‘integrated computational materials engineering’ have propelled the field forward. Data-driven materials integration that combines high-throughput computing with high-performance experiments is accelerating the development of innovative new materials. By integrating existing experimental and process data with high-throughput materials computation, a comprehensive performance target for materials (like mechanical properties, corrosion resistance, and biocompatibility) can be established. Material parameters such as composition and process parameters are used as input, and a large dataset of alloy composition-process-performance is collected and constructed. Finally, experimental validations of the composition design results

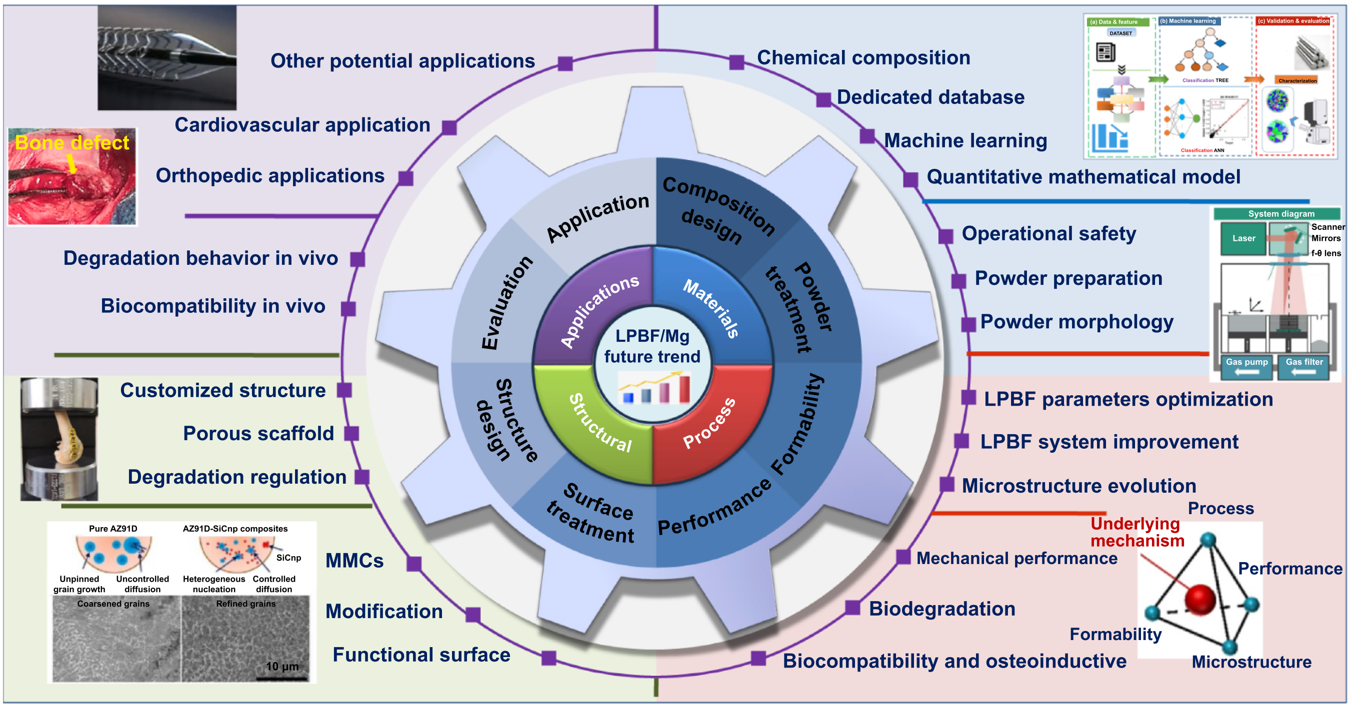

Figure 20. Significant technical factors of LPBF for biodegradable Mg-based implants.

are expected to be carried out to obtain Mg alloys with excellent performance for medical applications.

(2) From the term of process control, it is essential to establish a clear relationship of process-formability-microstructure-performance for high-performance biodegradable Mg-based implants manufactured by LPBF. Comparatively, the production of LPBF-processed Mg alloys poses greater challenges because of the unique properties of Mg and the complexity of forming mechanism. Inappropriate processing conditions can lead to defects such as element burning, porosity, lack of fusion, balling, and cracks. Currently, the control of defects in LPBF-processed Mg alloys relies heavily on extensive experiments to determine the optimal process parameters. There remains a gap in understanding the thermodynamic and kinetic processes involved in the interaction between the laser and Mg alloy powders. To address this limitation, *in-situ* monitoring of molten pool, alongside various numerical simulations techniques of temperature field, flow field, and microstructure evolution are essential for gaining a comprehensive insight into LPBF of Mg alloys. In addition, considering the certain risks associated with laser printing of Mg alloys, developing specialized equipment suitable for Mg alloys is also a future research direction, such as how to integrate explosion-proof devices.

(3) Laser AM provides significant design freedom for parts, enabling the creation of complex biomimetic porous structures. The design of porous structures has a crucial impact on the biocompatibility and osseointegration ability of implants. Among these, porosity, pore size, and pore structure are the core parameters that determine the implant's ability to induce new tissue growth. Currently, several pore structures are proposed, including Voronoi structure, spinous structure, and TPMS structure. TPMS is characterized by its periodicity, smoothness, continuity, and high specific surface area across three dimensions. It is well accepted that TPMS structural surfaces enhance cell movement, adhesion, and proliferation. However, the morphology of TPMS structures is often limited by fixed mathematical functions, resulting in predetermined structural parameters that restrict the design space. This limitation poses a significant challenge to fully realizing the potential of biomimetic design through parameter optimization. Furthermore, layered porous scaffolds with functional gradient features demonstrate superior mechanical properties and biological behavior compared to uniform porous structures. This gradient effect can be achieved by varying porosity, pore size, pillar size/thickness, or structural topology across different regions of the scaffold. Nonetheless, the design and integration of multiple functional areas and structure remain challenging, which should be one future research direction for LPBF-processed Mg alloys.

(4) For practical applications, it is essential to control the degradation rate of Mg-based implants while preserving their mechanical properties throughout the treatment period to support tissue healing, especially in high-load-bearing areas. Currently, research on the degradation behavior and biocompatibility of LPBF-processed Mg alloys has mostly been limited to animal studies. However, existing *in vivo* experiments on limb animals do not adequately replicate the stress evaluations necessary for successful implantation in humans. Therefore, further *in vivo*

studies using non-human primates are crucial to deepen our understanding of the mechanical, chemical, and biological interactions between Mg-based implants and living organisms. This interdisciplinary challenge requires optimizing implant performance through composition refinement, structural design, and adjustments to manufacturing processes, as well as accurately assessing their efficacy. Addressing these endeavors necessitates collaboration across the fields of materials science, engineering, information technology, biology, and medicine.

Acknowledgments

This study was supported by National Key Research and Development Program of China (2023YFB4605800); National Natural Science Foundation of China (52475362, 52165043); Jiang Xi Provincial Natural Science Foundation of China (20224ACB204013, 20224ACB214008, 20232BAB214007); Jiangxi Provincial Cultivation Program for Academic and Technical Leaders of Major Subjects (20225BCJ23008); Anhui Provincial Natural Science Foundation (2308085ME171); The University Synergy Innovation Program of Anhui Province (GXXT-2023-025, GXXT-2023-026); Ganzhou City science and technology project (204301000126); High-level Talents Scientific Research Start-up Program of Jiangxi University of Science and Technology (205200100350).

Conflict of interest

The authors declare that they have no known competing financial interests or personal relationships that could have appeared to influence the work reported in this paper.

CRediT authorship contribution statement

Xuehua Wu: Writing—original draft, Funding acquisition. Junying Liu: Writing—original draft. Jing Bai: Writing—review & editing. Joseph Buhagiar: Writing—review & editing. Youwen Yang: Review & editing, Funding acquisition, Conceptualization. Cijun Shuai: Investigation, Funding acquisition. XinghaiNing: Conceptualization, Writing—review & editing.

ORCID iDs

Youwen Yang https://orcid.org/0000-0003-1557-0252
Cijun Shuai https://orcid.org/0000-0002-2029-5112

References

[1] Wang N, Ma Y T, Shi H X, Song Y P, Guo S and Yang S D 2022 Mg-, Zn-, and Fe-based alloys with antibacterial properties as orthopedic implant materials *Front. Bioeng. Biotechnol.* **10** 888084

[2] Peng B, Xu H J, Song F, Wen P, Tian Y and Zheng Y F 2024 Additive manufacturing of porous magnesium alloys for biodegradable orthopedic implants: process, design, and modification *J. Mater. Sci. Technol.* **182** 79–110

[3] Niranjan C A, Raghavendra T, Rao M P, Siddaraju C, Gupta M, Jain V K S and Aishwarya R 2023 Magnesium alloys as extremely promising alternatives for temporary orthopedic implants—a review *J. Magnes. Alloys* **11** 2688–718

[4] Fu Q Y, Liang W Q, Huang J X, Jin W H, Guo B S, Li P, Xu S L, Chu P K and Yu Z T 2023 Research perspective and prospective of additive manufacturing of biodegradable magnesium-based materials *J. Magnes. Alloys* **11** 1485–504

[5] Khan A R, Grewal N S, Zhou C, Yuan K S, Zhang H J and Jun Z 2023 Recent advances in biodegradable metals for implant applications: exploring *in vivo* and *in vitro* responses *Results Eng.* **20** 101526

[6] Zhou Y, Zhang A X, Wu J B, Guo S and Sun Q 2024 Application and perspectives: magnesium materials in bone regeneration *ACS Biomater. Sci. Eng.* **10** 3514–27

[7] Seetharaman S, Sankaranarayanan D and Gupta M 2023 Magnesium-based temporary implants: potential, current status, applications, and challenges *J. Funct. Biomater.* **14** 324

[8] Rao J H, Gao H R, Sun J W, Yu R, Zhao D L and Ding Y M 2024 A critical review of biodegradable zinc alloys toward clinical applications *ACS Biomater. Sci. Eng.* **10** 5454–73

[9] Dong Z, Han C, Zhao Y, Huang J, Ling C, Hu G, Wang Y, Wang D, Song C and Yang Y 2024 Role of heterogenous microstructure and deformation behavior in achieving superior strength-ductility synergy in zinc fabricated via laser powder bed fusion *Int. J. Extreme Manuf.* **6** 045003

[10] Dong Z, Han C J, Liu G Q, Zhang J, Li Q L, Zhao Y Z, Wu H, Yang Y Q and Wang J H 2025 Revealing anisotropic mechanisms in mechanical and degradation properties of zinc fabricated by laser powder bed fusion additive manufacturing *J. Mater. Sci. Technol.* **214** 87–104

[11] Liu Y *et al* 2019 Fundamental theory of biodegradable metals-definition, criteria, and design *Adv. Funct. Mater.* **29** 1805402

[12] Kabir H, Munir K, Wen C and Li Y C 2021 Recent research and progress of biodegradable zinc alloys and composites for biomedical applications: biomechanical and biocorrosion perspectives *Bioact. Mater.* **6** 836–79

[13] Wang S Y, Li R, Xia D D, Zhao X, Zhu Y, Gu R L, Yoon J and Liu Y S 2021 The impact of Zn-doped synthetic polymer materials on bone regeneration: a systematic review *Stem Cell Res.* **12** 123

[14] Antoniac I, Miculescu M, Mănescu (Păltânea) V, Stere A, Quan P H, Păltânea G, Robu A and Earar K 2022 Magnesium-based alloys used in orthopedic surgery *Materials* **15** 1148

[15] Hong K, Park H, Kim Y, Knapek M, Minárik P, Máthis K, Yamamoto A and Choe H 2019 Mechanical and biocorrosive properties of magnesium-aluminum alloy scaffold for biomedical applications *J. Mech. Behav. Biomed. Mater.* **98** 213–24

[16] Yang Y W, He C X, Dianyu E, Yang W J, Qi F W, Xie D Q, Shen L D, Peng S P and Shuai C J 2020 Mg bone implant: features, developments and perspectives *Mater. Des.* **185** 108259

[17] Yang Y, Xiong X M, Chen J, Peng X D, Chen D L and Pan F S 2021 Research advances in magnesium and magnesium alloys worldwide in 2020 *J. Magnes. Alloys* **9** 705–47

[18] Xia D D, Yang F, Zheng Y F, Liu Y S and Zhou Y S 2021 Research status of biodegradable metals designed for oral

and maxillofacial applications: a review *Bioact. Mater.* **6** 4186–208

[19] Wang H Y, Yuan H N, Wang J M, Zhang E G, Bai M Y, Sun Y F, Wang J F, Zhu S J, Zheng Y F and Guan S K 2021 Influence of the second phase on protein adsorption on biodegradable Mg alloys' surfaces: comparative experimental and molecular dynamics simulation studies *Acta Biomater.* **129** 323–32

[20] Gu D D, Hagedorn Y C, Meiners W, Meng G B, Batista R J S, Wissenbach K and Poprawe R 2012 Densification behavior, microstructure evolution, and wear performance of selective laser melting processed commercially pure titanium *Acta Mater.* **60** 3849–60

[21] Heublein B, Rohde R, Kaese V, Niemeyer M, Hartung W and Haverich A 2003 Biocorrosion of magnesium alloys: a new principle in cardiovascular implant technology *Heart* **89** 651–6

[22] Seitz J M, Lucas A and Kirschner M 2016 Magnesium-based compression screws: a novelty in the clinical use of implants *JOM* **68** 1177–82

[23] Lee J W *et al* 2016 Long-term clinical study and multiscale analysis of *in vivo* biodegradation mechanism of Mg alloy *Proc. Natl Acad. Sci. USA* **113** 716–21

[24] Zhao D W *et al* 2016 Vascularized bone grafting fixed by biodegradable magnesium screw for treating osteonecrosis of the femoral head *Biomaterials* **81** 84–92

[25] Ding W J 2016 Opportunities and challenges for the biodegradable magnesium alloys as next-generation biomaterials *Regen. Biomater.* **3** 79–86

[26] Ansari N, Alabtah F G, Albakri M I and Khraisheh M 2024 Post processing of additive manufactured Mg alloys: current status, challenges, and opportunities *J. Magnes. Alloys* **12** 1283–310

[27] Lin X *et al* 2023 Biodegradable Mg-based alloys: biological implications and restorative opportunities *Int. Mater. Rev.* **68** 365–403

[28] Shan Z M, Xie X H, Wu X T, Zhuang S Y and Zhang C 2022 Development of degradable magnesium-based metal implants and their function in promoting bone metabolism (a review) *J. Orthop. Transl.* **36** 184–93

[29] Nasr Azadani M, Zahedi A, Bowoto O K and Oladapo B I 2022 A review of current challenges and prospects of magnesium and its alloy for bone implant applications *Prog. Biomater.* **11** 1–26

[30] Mohanasundaram S, Bhong M, Vatsa G, Verma R P, Srivastava M, Kumar G, Mohammed K A, Singh D and Gupta L R 2023 Mg-based metal matrix composite in biomedical applications: a review *Mater. Today Proc.*

[31] Zhang L, Yang G J, Johnson B N and Jia X F 2019 Three-dimensional (3D) printed scaffold and material selection for bone repair *Acta Biomater.* **84** 16–33

[32] Dong Q S, Li Y, Jiang H Q, Zhou X X, Liu H, Lu M M, Chu C L, Xue F and Bai J 2021 3D-cubic interconnected porous Mg-based scaffolds for bone repair *J. Magnesium Alloys* **9** 1329–38

[33] Shuai C J, Li D S, Yao X, Li X and Gao C D 2023 Additive manufacturing of promising heterostructure for biomedical applications *Int. J. Extreme Manuf.* **5** 032012

[34] Yan Y F *et al* 2019 Vascularized 3D printed scaffolds for promoting bone regeneration *Biomaterials* **190–191** 97–110

[35] Badoniya P, Srivastava M, Jain P K and Rathee S 2024 A state-of-the-art review on metal additive manufacturing: milestones, trends, challenges and perspectives *J. Braz. Soc. Mech. Sci. Eng.* **46** 339

[36] Kharat V J, Singh P, Raju G S, Yadav D K, Gupta M S, Arun V, Majeed A H and Singh N 2023 Additive manufacturing (3D printing): a review of materials, methods, applications and challenges *Mater. Today Proc.*

[37] Zhu S, Du W B, Wang X M, Han G F, Ren Z Q and Zhou K B 2023 Advanced additive remanufacturing technology *Chin. J. Mech. Eng.* **2** 100066

[38] Zhou L F, Miller J, Vezza J, Mayster M, Raffay M, Justice Q, Al Tamimi Z, Hansotte G, Sunkara L D and Bernat J 2024 Additive manufacturing: a comprehensive review *Sensors* **24** 2668

[39] Bandyopadhyay A, Mitra I, Avila J D, Upadhyayula M and Bose S 2023 Porous metal implants: processing, properties, and challenges *Int. J. Extreme Manuf.* **5** 032014

[40] Mao M, Meng Z J, Huang X X, Zhu H, Wang L, Tian X Y, He J K, Li D C and Lu B H 2024 3D printing in space: from mechanical structures to living tissues *Int. J. Extreme Manuf.* **6** 023001

[41] Chen L Y, Qin P, Zhang L N and Zhang L C 2024 An overview of additively manufactured metal matrix composites: preparation, performance, and challenge *Int. J. Extreme Manuf.* **6** 052006

[42] Zhu C, Gemeda H B, Duoss E B and Spadaccini C M 2024 Toward multiscale, multimaterial 3D printing *Adv. Mater.* **36** e2314204

[43] Wei C, Zhang Z Z, Cheng D X, Sun Z, Zhu M H and Li L 2021 An overview of laser-based multiple metallic material additive manufacturing: from macro- to micro-scales *Int. J. Extreme Manuf.* **3** 012003

[44] Dhavalikar P, Lan Z Y, Kar R, Salhadar K, Gaharwar A K and Cosgriff-Hernandez E 2020 Biomedical applications of additive manufacturing *Biomaterials Science* ed W R Wagner, S E Sakiyama-Elbert, G G Zhang and M J Yaszemski (Elsevier) pp 643–4

[45] DebRoy T, Wei H L, Zuback J S, Mukherjee T, Elmer J W, Milewski J O, Beese A M, Wilson-Heid A, De A and Zhang W 2018 Additive manufacturing of metallic components—process, structure and properties *Prog. Mater. Sci.* **92** 112–224

[46] Yang Y Q *et al* 2024 Frontiers in laser additive manufacturing technology *Addit. Manuf. Front.* **3** 200160

[47] Qin Y, Wen P, Guo H, Xia D D, Zheng Y F, Jauer L, Poprawe R, Voshage M and Schleifenbaum J H 2019 Additive manufacturing of biodegradable metals: current research status and future perspectives *Acta Biomater.* **98** 3–22

[48] Li Y *et al* 2018 Additively manufactured biodegradable porous magnesium *Acta Biomater.* **67** 378–92

[49] Qi X H, Liang X K, Wang J H, Zhang H R, Wang X B and Liu Z Z 2024 Microstructure tailoring in laser powder bed fusion (L-PBF): strategies, challenges, and future outlooks *J. Alloys Compd.* **970** 172564

[50] Sing S L, An J, Yeong W Y and Wiria F E 2016 Laser and electron-beam powder-bed additive manufacturing of metallic implants: a review on processes, materials and designs *J. Orthop. Res.* **34** 369–85

[51] Tan C L, Deng C, Li S, Abena A, Jamshidi P, Essa K, Wu L, Xu G, Attallah M M and Liu J 2022 Mechanical property and biological behaviour of additive manufactured TiNi functionally graded lattice structure *Int. J. Extreme Manuf.* **4** 045003

[52] Sun X Y, Chen M A, Liu T T, Zhang K, Wei H L, Zhu Z G and Liao W H 2024 Characterization, preparation, and reuse of metallic powders for laser powder bed fusion: a review *Int. J. Extreme Manuf.* **6** 012003

[53] K V, Kumar B N, Kumar S S and Vignesh M 2022 Magnesium role in additive manufacturing of biomedical implants—challenges and opportunities *Addit. Manuf.* **55** 102802

[54] Wei K W, Wang Z M and Zeng X Y 2015 Influence of element vaporization on formability, composition, microstructure, and mechanical performance of the

selective laser melted Mg-Zn-Zr components *Mater. Lett.* **156** 187–90

[55] Jauer L, Jülich B, Voshage M and Meiners W 2015 Selective laser melting of magnesium alloys *Eur. Cells Mater.* **30**

[56] Liu J G *et al* 2022 Biodegradable magnesium alloy WE43 porous scaffolds fabricated by laser powder bed fusion for orthopedic applications: process optimization, *in vitro* and *in vivo* investigation *Bioact. Mater.* **16** 301–19

[57] Liu C Y, Ling C R, Chen C, Wang D S, Yang Y W, Xie D Q and Shuai C J 2022 Laser additive manufacturing of magnesium alloys and its biomedical applications *Mater. Sci. Addit. Manuf.* **1** 24

[58] Manakari V, Parande G and Gupta M 2017 Selective laser melting of magnesium and magnesium alloy powders: a review *Metals* **7** 2

[59] Munir K, Biesiekierski A, Wen C and Li Y C 2020 Selective laser melting in biomedical manufacturing *Metallic Biomaterials Processing and Medical Device Manufacturing* ed C Wen (Elsevier) pp 235–69

[60] Zhang W N, Wang L Z, Feng Z X and Chen Y M 2020 Research progress on selective laser melting (SLM) of magnesium alloys: a review *Optik* **207** 163842

[61] Manjhi S K, Sekar P, Bontha S and Balan A S S 2024 Additive manufacturing of magnesium alloys: characterization and post-processing *Int. J. Lightweight Mater. Manuf.* **7** 184–213

[62] Sui S *et al* 2023 Additive manufacturing of magnesium and its alloys: process-formability-microstructure-performance relationship and underlying mechanism *Int. J. Extreme Manuf.* **5** 042009

[63] Peng L M, Deng Q C, Wu Y J, Fu P H, Liu Z Y, Wu Q Y, Chen K and Ding W J 2023 Additive manufacturing of magnesium alloys by selective laser melting technology: a review *Acta Metall Sin.* **59** 31

[64] Badkoobeh F, Mostaan H, Rafiei M, Bakhsheshi-Rad H R, RamaKrishna S and Chen X B 2023 Additive manufacturing of biodegradable magnesium-based materials: design strategies, properties, and biomedical applications *J. Magnes. Alloys* **11** 801–39

[65] Zeng Z R, Salehi M, Kopp A, Xu S W, Esmaily M and Birbilis N 2022 Recent progress and perspectives in additive manufacturing of magnesium alloys *J. Magnes. Alloys* **10** 1511–41

[66] Tang W N, Mo N and Hou J 2023 Research progress of additively manufactured magnesium alloys: a review *Aata Metall. Sin.* **59** 205

[67] Wang T S, Hua Z M, Yang Y J, Jia H L, Wang C, Zha M, Gao Y P and Wang H Y 2024 Macro-/micro-structures and mechanical properties of magnesium alloys based on additive manufacturing: a review *J. Mater. Sci.* **59** 9908–40

[68] Kruth J P, Mercelis P, Van Vaerenbergh J, Froyen L and Rombouts M 2005 Binding mechanisms in selective laser sintering and selective laser melting *Rapid Prototyp. J.* **11** 26–36

[69] Zhu H, Yao C, Wei B Y, Xu C Y, Huang X X, Liu Y, He J K, Zhang J N and Li D C 2023 3D printing of functional bioengineered constructs for neural regeneration: a review *Int. J. Extreme Manuf.* **5** 042004

[70] Chowdhury S, Yadaiah N, Prakash C, Ramakrishna S, Dixit S, Gupta L R and Buddhi D 2022 Laser powder bed fusion: a state-of-the-art review of the technology, materials, properties & defects, and numerical modelling *J. Mater. Res. Technol.* **20** 2109–72

[71] Karunakaran R, Ortgies S, Tamayol A, Bobaru F and Sealy M P 2020 Additive manufacturing of magnesium alloys *Bioact. Mater.* **5** 44–54

[72] Qin Y, Liu J G, Chen Y Z, Wen P, Zheng Y F, Tian Y, Voshage M and Schleifenbaum J H 2021 Influence of laser energy input and shielding gas flow on evaporation fume during laser powder bed fusion of Zn metal *Materials* **14** 2677

[73] Sezer N, Evis Z and Koç M 2021 Additive manufacturing of biodegradable magnesium implants and scaffolds: review of the recent advances and research trends *J. Magnes. Alloys* **9** 392–415

[74] Chen J Y and Chen B 2024 Progress in additive manufacturing of magnesium alloys: a review *Materials* **17** 3851

[75] Shuai C J, Zan J, Qi F W, Wang G Y, Liu Z, Yang Y W and Peng S P 2019 nMgO-incorporated PLLA bone scaffolds: enhanced crystallinity and neutralized acidic products *Mater. Des.* **174** 107801

[76] Kaljevic A and Demir A G 2022 Influence of shielding gas flow on the μLMWD of biodegradable Mg alloy and permanent stainless steel for additive manufacturing of biomedical implants *Int. J. Adv. Manuf. Technol.* **119** 4877–91

[77] Gnedenkov A S, Sinebryukhov S L, Mashtalyar D V, Gnedenkov S V, Subbotin E P, Nikitin A I, Nadaraia K V and Kulchin Y N 2018 Direct laser deposition as a method of biodegradable magnesium implant manufacturing *J. Phys.: Conf. Ser.* **1092** 012044

[78] Li Y, Yin S Q, Zhang G Z, Wang C F, Liu X and Guan R G 2024 A review on wire arc additive manufacturing of magnesium alloys: wire preparation, defects and properties *Met. Mater. Int.*

[79] Kuah K X, Blackwood D J, Ong W K, Salehi M, Seet H L, Nai M L S and Wijesinghe S 2022 Analysis of the corrosion performance of binder jet additive manufactured magnesium alloys for biomedical applications *J. Magnes. Alloys* **10** 1296–310

[80] Salehi M, Maleksaeedi S, Sapari M A B, Nai M L S, Meenashisundaram G K and Gupta M 2019 Additive manufacturing of magnesium–zinc–zirconium (ZK) alloys via capillary-mediated binderless three-dimensional printing *Mater. Des.* **169** 107683

[81] Palanivel S, Nelaturu P, Glass B and Mishra R S 2015 Friction stir additive manufacturing for high structural performance through microstructural control in an Mg based WE43 alloy *Mater. Des.* **65** 934–52

[82] Wlodarski S, Avery D Z, White B C, Mason C J T, Cleek C, Williams M B, Allison P G and Jordon J B 2021 Evaluation of grain refinement and mechanical properties of additive friction stir layer welding of AZ31 magnesium alloy *J. Mater. Eng. Perform.* **30** 964–72

[83] Ramazani H and Kami A 2022 Metal FDM, a new extrusion-based additive manufacturing technology for manufacturing of metallic parts: a review *Prog. Addit. Manuf.* **7** 609–26

[84] Buzko V, Ivanin S, Goryachko A, Shutkin I, Pushankina P and Petriev I 2023 Magnesium spinel ferrites development for FDM 3D-printing material for microwave absorption *Processes* **11** 60

[85] He L Z, Liu X L and Rudd C 2021 Additive-manufactured gyroid scaffolds of magnesium oxide, phosphate glass fiber and polylactic acid composite for bone tissue engineering *Polymers* **13** 270

[86] Sing S L and Yeong W Y 2020 Laser powder bed fusion for metal additive manufacturing: perspectives on recent developments *Virtual Phys. Prototyp.* **15** 359–70

[87] Liu S, Yang W S, Shi X, Li B, Duan S C, Guo H J and Guo J 2019 Influence of laser process parameters on the densification, microstructure, and mechanical properties of a selective laser melted AZ61 magnesium alloy *J. Alloys Compd.* **808** 151160

[88] Xu W Y, Fu P H, Wang N Q, Yang L, Peng L M, Chen J and Ding W J 2024 Effects of processing parameters on fabrication defects, microstructure and mechanical

properties of additive manufactured Mg-Nd-Zn-Zr alloy by selective laser melting process *J. Magnes. Alloys* **12** 2249–66

[89] Wei K W, Gao M, Wang Z M and Zeng X Y 2014 Effect of energy input on formability, microstructure and mechanical properties of selective laser melted AZ91D magnesium alloy *Mater. Sci. Eng.* A **611** 212–22

[90] Liu C, Zhang M and Chen C J 2017 Effect of laser processing parameters on porosity, microstructure and mechanical properties of porous Mg-Ca alloys produced by laser additive manufacturing *Mater. Sci. Eng.* A **703** 359–71

[91] Hyer H, Zhou L, Benson G, McWilliams B, Cho K and Sohn Y 2020 Additive manufacturing of dense WE43 Mg alloy by laser powder bed fusion *Addit. Manuf.* **33** 101123

[92] Deng Q C, Wang X C, Lan Q, Chang Z Y, Liu Z H, Su N, Wu Y J, Liu D Z, Peng L M and Ding W J 2022 Limitations of linear energy density for laser powder bed fusion of Mg-15Gd-1Zn-0.4Zr alloy *Mater. Charact.* **190** 112071

[93] Wang X C, Chen C J and Zhang M 2020 Effect of laser power on formability, microstructure and mechanical properties of selective laser melted Mg-Al-Zn alloy *Rapid Prototyp. J.* **26** 841–54

[94] Li X, Liu Y Z and Zhou Z G 2022 Influence of hatch distance on processing, microstructure and mechanical properties of AlMgScZr alloy fabricated by laser powder bed fusion *J. Manuf. Process.* **81** 78–91

[95] Zhou Y H, Li W P, Zhang L, Zhou S Y, Jia X, Wang D W and Yan M 2020 Selective laser melting of Ti-22Al-25Nb intermetallic: significant effects of hatch distance on microstructural features and mechanical properties *J. Mater. Process. Technol.* **276** 116398

[96] Xia M J, Gu D D, Yu G Q, Dai D H, Chen H Y and Shi Q M 2016 Influence of hatch spacing on heat and mass transfer, thermodynamics and laser processability during additive manufacturing of Inconel 718 alloy *Int. J. Mach. Tools Manuf.* **109** 147–57

[97] Dong Z C, Liu Y B, Wen W B, Ge J R and Liang J 2019 Effect of hatch spacing on melt pool and as-built quality during selective laser melting of stainless steel: modeling and experimental approaches *Materials* **12** 50

[98] Savalani M M and Pizarro J M 2016 Effect of preheat and layer thickness on selective laser melting (SLM) of magnesium *Rapid Prototyp. J.* **22** 115–22

[99] Yin B Z, Liu J G, Peng B, Zhou M R, Liu B C, Ma X L, Wang C M, Wen P, Tian Y and Zheng Y F 2024 Influence of layer thickness on formation quality, microstructure, mechanical properties, and corrosion resistance of WE43 magnesium alloy fabricated by laser powder bed fusion *J. Magnes. Alloys* **12** 1367–85

[100] Olakanmi E O, Cochrane R F and Dalgarno K W 2011 Densification mechanism and microstructural evolution in selective laser sintering of Al-12Si powders *J. Mater. Process. Technol.* **211** 113–21

[101] Esmaily M *et al* 2020 A detailed microstructural and corrosion analysis of magnesium alloy WE43 manufactured by selective laser melting *Addit. Manuf.* **35** 101321

[102] Liang J W, Lei Z L, Chen Y B, Wu S B, Chen X, Jiang M and Cao S Y 2022 Formability, microstructure, and thermal crack characteristics of selective laser melting of ZK60 magnesium alloy *Mater. Sci. Eng.* A **839** 142858

[103] Ling C R, Li Q, Zhang Z, Yang Y W, Zhou W H, Chen W L, Dong Z, Pan C R and Shuai C J 2024 Influence of heat treatment on microstructure, mechanical and corrosion behavior of WE43 alloy fabricated by laser-beam powder bed fusion *Int. J. Extreme Manuf.* **6** 015001

[104] Liu S and Guo H J 2020 A review of slmed magnesium alloys: processing, properties, alloying elements and postprocessing *Metals* **10** 1073

[105] Jhabvala J, Boillat E, Antignac T and Glardon R 2010 On the effect of scanning strategies in the selective laser melting process *Virtual Phys. Prototyp.* **5** 99–109

[106] Ouyang L X, Zhang S L, Zhang Y H, Wang J F, Wang Z H, Feng L, Gui Y W and Pan F S 2024 Manipulating scanning strategies towards controlled microstructure of laser remelted Mg-3Al-1Zn alloy *J. Mater. Sci.* **30** 7533–44

[107] Wang K K, Wang W L, Xu R R, Zhao D, Li H Y and Dong G W 2023 Effects of scanning strategy on the densification and microhardness of selective laser melting Mg–Y–Sm–Zn–Zr alloy *Adv. Eng. Mater.* **25** 2201173

[108] Zhang H, Gu D D and Dai D H 2022 Laser printing path and its influence on molten pool configuration, microstructure and mechanical properties of laser powder bed fusion processed rare earth element modified Al-Mg alloy *Virtual Phys. Prototyp.* **17** 308–28

[109] Wei K W, Wang Z M and Zeng X Y 2016 Element loss of AZ91D magnesium alloy during selective laser melting process *Acta Metall. Sin.* **52** 184–90

[110] Li G, Li X W, Guo C, Zhou Y, Tan Q Y, Qu W Y, Li X G, Hu X G, Zhang M X and Zhu Q 2022 Investigation into the effect of energy density on densification, surface roughness and loss of alloying elements of 7075 aluminium alloy processed by laser powder bed fusion *Opt. Laser Technol.* **147** 107621

[111] Wen P, Qin Y, Chen Y Z, Voshage M, Jauer L, Poprawe R and Schleifenbaum J H 2019 Laser additive manufacturing of Zn porous scaffolds: shielding gas flow, surface quality and densification *J. Mater. Sci. Technol.* **35** 368–76

[112] Deng Q C, Wu Y J, Wu Q Y, Xue Y T, Zhang Y, Peng L M and Ding W J 2022 Microstructure evolution and mechanical properties of a high-strength Mg-10Gd-3Y-1Zn-0.4Zr alloy fabricated by laser powder bed fusion *Addit. Manuf.* **49** 102517

[113] Gieseke M, Noelke C, Kaierle S, Wesling V and Haferkamp H 2013 Selective laser melting of magnesium and magnesium alloys *Magnesium Technology 2013* ed N Hort, S N Mathaudhu, N R Neelameggham and M Alderman (Springer) pp 66–68

[114] Hojjatzadeh S M H *et al* 2020 Direct observation of pore formation mechanisms during LPBF additive manufacturing process and high energy density laser welding *Int. J. Mach. Tools Manuf.* **153** 103555

[115] Sola A and Nouri A 2019 Microstructural porosity in additive manufacturing: the formation and detection of pores in metal parts fabricated by powder bed fusion *J. Adv. Manuf. Process.* **1** e10021

[116] Xu W H, Li J, Zhang Z, Yuan H, An G, Shi H, Cai C, Jiang W, Li W and Wei Q 2024 Laser powder bed fusion of WE43 magnesium alloy with superior balance of strength and ductility *J. Magnes. Alloys* (https://doi.org/10.1016/j.jma.2024.03.012)

[117] Deng Q C, Wu Y J, Luo Y H, Su N, Xue X Y, Chang Z Y, Wu Q Y, Xue Y T and Peng L M 2020 Fabrication of high-strength Mg-Gd-Zn-Zr alloy via selective laser melting *Mater. Charact.* **165** 110377

[118] Zhao C, Parab N D, Li X X, Fezzaa K, Tan W D, Rollett A D and Sun T 2020 Critical instability at moving keyhole tip generates porosity in laser melting *Science* **370** 1080–6

[119] Cunningham R, Zhao C, Parab N, Kantzos C, Pauza J, Fezzaa K, Sun T and Rollett A D 2019 Keyhole threshold and morphology in laser melting revealed by ultrahigh-speed x-ray imaging *Science* **363** 849–52

[120] Wang L, Zhang Y M, Chia H Y and Yan W T 2022 Mechanism of keyhole pore formation in metal additive manufacturing *npj Comput. Mater.* **8** 22

[121] Yi H, Wang Z P, Li J X, Luo J, Cao H J and Qi L H 2024 Gas entrapment and pore formation in metal droplet-based 3D printing *Int. J. Mech. Sci.* **264** 108810

[122] Attarzadeh F and Asadi E 2022 Analysis of element loss, densification, and defects in laser-based powder-bed fusion of magnesium alloy WE43 *J. Magnes. Alloys* **10** 2118–36

[123] Wu C L, Zai W and Man H C 2021 Additive manufacturing of ZK60 magnesium alloy by selective laser melting: parameter optimization, microstructure and biodegradability *Mater. Today Commun.* **26** 101922

[124] Liu J G, Yin B Z, Sun Z R, Wen P, Zheng Y F and Tian Y 2021 Hot cracking in ZK60 magnesium alloy produced by laser powder bed fusion process *Mater. Lett.* **301** 130283

[125] Tenbrock C, Fischer F G, Wissenbach K, Schleifenbaum J H, Wagenblast P, Meiners W and Wagner J 2020 Influence of keyhole and conduction mode melting for top-hat shaped beam profiles in laser powder bed fusion *J. Mater. Process. Technol.* **278** 116514

[126] Sibillano T, Ancona A, Berardi V, Schingaro E, Basile G and Lugarà P M 2007 Optical detection of conduction/keyhole mode transition in laser welding *J. Mater. Process. Technol.* **191** 364–7

[127] DePond P J, Fuller J C, Khairallah S A, Angus J R, Guss G, Matthews M J and Martin A A 2020 Laser-metal interaction dynamics during additive manufacturing resolved by detection of thermally-induced electron emission *Commun. Mater.* **1** 92

[128] Huang Y Z, Fleming T G, Clark S J, Marussi S, Fezzaa K, Thiyagalingam J, Leung C L A and Lee P D 2022 Keyhole fluctuation and pore formation mechanisms during laser powder bed fusion additive manufacturing *Nat. Commun.* **13** 1170

[129] Liu S and Guo H J 2020 Balling behavior of selective laser melting (SLM) magnesium alloy *Materials* **13** 3632

[130] Li R D, Liu J H, Shi Y S, Wang L and Jiang W 2012 Balling behavior of stainless steel and nickel powder during selective laser melting process *Int. J. Adv. Manuf. Technol.* **59** 1025–35

[131] Fu J, Li H, Song X and Fu M W 2022 Multi-scale defects in powder-based additively manufactured metals and alloys *J. Mater. Sci. Technol.* **122** 165–99

[132] Hu D, Wang Y, Zhang D F, Hao L, Jiang J J, Li Z H and Chen Y T 2015 Experimental investigation on selective laser melting of bulk net-shape pure magnesium *Mater. Manuf. Process.* **30** 1298–304

[133] Wang Y C, Fu P H, Wang N Q, Peng L M, Kang B, Zeng H, Yuan G Y and Ding W J 2020 Challenges and solutions for the additive manufacturing of biodegradable magnesium implants *Engineering* **6** 1267–75

[134] Brückner F, Finaske T, Willner R, Seidel A, Nowotny S, Leyens C and Beyer E 2015 Laser additive manufacturing with crack-sensitive materials: temperature monitoring system for defect-free material build-up *Opt. Laser Technol.* **2** 28–30

[135] Mercelis P and Kruth J P 2006 Residual stresses in selective laser sintering and selective laser melting *Rapid Prototyp. J.* **12** 254–65

[136] Chen C P, Xiao Z X, Wang Y L, Yang X and Zhu H H 2021 Prediction study on in-situ reduction of thermal stress using combined laser beams in laser powder bed fusion *Addit. Manuf.* **47** 102221

[137] Benn F, D'Elia F, van Gaalen K, Li M Z, Malinov S and Kopp A 2022 Printability, mechanical and degradation properties of Mg-(x)Zn elemental powder mixes processed by laser powder bed fusion *Addit. Manuf. Lett.* **2** 100025

[138] Niu X M, Shen H Y, Xu G H, Zhang L C, Fu J Z and Deng X L 2019 Effect of aluminium content and processing parameters on the microstructure and mechanical properties of laser powder-bed fused magnesium-aluminium (0, 3, 6, 9wt%) powder mixture *Rapid Prototyp. J.* **25** 744–51

[139] Liang J W, Lei Z L, Chen B Y, Fu W J, Chen X and Ma S C 2022 Elimination of extraordinarily high cracking susceptibility of ZK60 Mg alloy fabricated by laser powder bed fusion *Mater. Lett.* **312** 131731

[140] Roehling J D, Smith W L, Roehling T T, Vrancken B, Guss G M, McKeown J T, Hill M R and Matthews M J 2019 Reducing residual stress by selective large-area diode surface heating during laser powder bed fusion additive manufacturing *Addit. Manuf.* **28** 228–35

[141] Dong Z, Kang H, Xie Y, Chi C and Peng X 2019 Effect of powder oxygen content on microstructure and mechanical properties of a laser additively-manufactured 12CrNi$_2$ alloy steel *Mater. Lett.* **236** 214–7

[142] Ng C C, Savalani M M, Lau M L and Man H C 2011 Microstructure and mechanical properties of selective laser melted magnesium *Appl. Surf. Sci.* **257** 7447–54

[143] Salehi M, Maleksaeedi S, Farnoush H, Nai M L S, Meenashisundaram G K and Gupta M 2018 An investigation into interaction between magnesium powder and Ar gas: implications for selective laser melting of magnesium *Powder Technol.* **333** 252–61

[144] Deng Q C, Wu Y J, Zhu W X, Chen K, Liu D Z, Peng L M and Ding W J 2022 Effect of heat treatment on microstructure evolution and mechanical properties of selective laser melted Mg-11Gd-2Zn-0.4Zr alloy *Mater. Sci. Eng.* A **829** 142139

[145] Yu W H, Sing S L, Chua C K, Kuo C N and Tian X L 2019 Particle-reinforced metal matrix nanocomposites fabricated by selective laser melting: a state of the art review *Prog. Mater. Sci.* **104** 330–79

[146] Zumdick N A, Jauer L, Kersting L C, Kutz T N, Schleifenbaum J H and Zander D 2019 Additive manufactured WE43 magnesium: a comparative study of the microstructure and mechanical properties with those of powder extruded and as-cast WE43 *Mater. Charact.* **147** 384–97

[147] Julmi S, Abel A, Gerdes N, Hoff C, Hermsdorf J, Overmeyer L, Klose C and Maier H J 2021 Development of a laser powder bed fusion process tailored for the additive manufacturing of high-quality components made of the commercial magnesium alloy WE43 *Materials* **14** 887

[148] Bär F, Berger L, Jauer L, Kurtuldu G, Schäublin R, Schleifenbaum J H and Löffler J F 2019 Laser additive manufacturing of biodegradable magnesium alloy WE43: a detailed microstructure analysis *Acta Biomater.* **98** 36–49

[149] Ying T, Zhao Z X, Yan P F, Wang J Y and Zeng X Q 2022 Effect of fabrication parameters on the microstructure and mechanical properties of wire arc additive manufactured AZ61 alloy *Mater. Lett.* **307** 131014

[150] Xie B, Zhao M C, Zhao Y C, Tian Y, Yin D F, Gao C D, Shuai C J and Atrens A 2020 Effect of alloying mn by selective laser melting on the microstructure and biodegradation properties of pure Mg *Metals* **10** 1527

[151] Xie B, Zhao M C, Xu R, Zhao Y C, Yin D F, Gao C D and Atrens A 2020 Biodegradation, antibacterial performance, and cytocompatibility of a novel ZK30-Cu-Mn biomedical alloy produced by selective laser melting *Int. J. Bioprint.* **7** 300

[152] Wei K W, Zeng X Y, Wang Z M, Deng J F, Liu M N, Huang G and Yuan X C 2019 Selective laser melting of Mg-Zn binary alloys: effects of Zn content on densification behavior, microstructure, and mechanical property *Mater. Sci. Eng.* A **756** 226–36

[153] Xu R, Zhao M C, Zhao Y C, Liu L, Liu C, Gao C D, Shuai C J and Atrens A 2019 Improved biodegradation resistance by grain refinement of novel antibacterial

ZK30-Cu alloys produced via selective laser melting *Mater. Lett.* **237** 253–7

[154] Liu L, Ma H T, Gao C D, Shuai C J and Peng S P 2020 Island-to-acicular alteration of second phase enhances the degradation resistance of biomedical AZ61 alloy *J. Alloys Compd.* **835** 155397

[155] Shuai C J, He C X, Feng P, Guo W, Gao C D, Wu P, Yang Y W and Bin S 2018 Biodegradation mechanisms of selective laser-melted Mg-*x*Al-Zn alloy: grain size and intermetallic phase *Virtual Phys. Prototyp.* **13** 59–69

[156] Niu X M, Shen H Y, Fu J Z, Yan J W and Wang Y 2019 Corrosion behaviour of laser powder bed fused bulk pure magnesium in hank's solution *Corros. Sci.* **157** 284–94

[157] Li M Z, Benn F, Derra T, Kröger N, Zinser M, Smeets R, Molina-Aldareguia J M, Kopp A and Llorca J 2021 Microstructure, mechanical properties, corrosion resistance and cytocompatibility of WE43 Mg alloy scaffolds fabricated by laser powder bed fusion for biomedical applications *Mater. Sci. Eng.* C **119** 111623

[158] Manne B, Thiruvayapati H, Bontha S, Motagondanahalli Rangarasaiah R, Das M and Balla V K 2018 Surface design of Mg-Zn alloy temporary orthopaedic implants: tailoring wettability and biodegradability using laser surface melting *Surf. Coat. Technol.* **347** 337–49

[159] Niu X M, Shen H Y, Fu J Z and Feng J W 2021 Effective control of microstructure evolution in AZ91D magnesium alloy by SiC nanoparticles in laser powder-bed fusion *Mater. Des.* **206** 109787

[160] Rojaee R, Fathi M and Raeissi K 2013 Electrophoretic deposition of nanostructured hydroxyapatite coating on AZ91 magnesium alloy implants with different surface treatments *Appl. Surf. Sci.* **285** 664–73

[161] Deng Q C, Zhang Y, Liu Z Y, Chang Z Y, Su N, Wu Y J, Hao L L, Peng L M and Ding W J 2022 Laser powder bed fusion of an age-hardenable Mg-10Gd-0.2Zr alloy with excellent strength-ductility synergy *J. Alloys Compd.* **910** 164863

[162] Bian D, Tong Z P, Gong G C, Huang H, Cai G X, Yan X C, Yu H, Chang C and Zheng Y F 2024 A spatiotemporal "bulk erosion" mode in selective laser melted magnesium alloys and the resulting adverse cell & tissue responses *J. Mater. Sci. Technol.* **198** 243–58

[163] Dobkowska A *et al* 2022 A comparison of the microstructure-dependent corrosion of dual-structured Mg-Li alloys fabricated by powder consolidation methods: laser powder bed fusion vs pulse plasma sintering *J. Magnes. Alloys* **10** 3553–64

[164] Li X and Liu Y Z 2023 Effect of laser remelting on printability, microstructure and mechanical performance of Al-Mg-Sc-Zr alloy produced by laser powder bed fusion *J. Alloys Compd.* **963** 171287

[165] Wang G, Ouyang H, Fan C, Guo Q, Li Z Q, Yan W T and Li Z 2020 The origin of high-density dislocations in additively manufactured metals *Mater. Res. Lett.* **8** 283–90

[166] Hu D J, Grilli N and Yan W T 2023 Dislocation structures formation induced by thermal stress in additive manufacturing: multiscale crystal plasticity modeling of dislocation transport *J. Mech. Phys. Solids* **173** 105235

[167] Mu Y K, He L H, Deng S H, Jia Y F, Jia Y D, Wang G, Zhai Q J, Liaw P K and Liu C T 2022 A high-entropy alloy with dislocation-precipitate skeleton for ultrastrength and ductility *Acta Mater.* **232** 117975

[168] Liu L F, Ding Q Q, Zhong Y, Zou J, Wu J, Chiu Y L, Li J X, Zhang Z, Yu Q and Shen Z J 2018 Dislocation network in additive manufactured steel breaks strength-ductility trade-off *Mater. Today* **21** 354–61

[169] Chen C, Li S Y, Ling C R, Yang Y W, Gao C D, Li Y G, Xiao X Y, Zhou W H and Shuai C J 2023 Laser printed amorphous magnesium alloy: microstructure, mechanical properties and degradation behavior *J. Mater. Res. Technol.* **27** 6961–73

[170] Li H F and Zheng Y F 2016 Recent advances in bulk metallic glasses for biomedical applications *Acta Biomater.* **36** 1–20

[171] Zhang P L, Tan J, Tian Y T, Yan H and Yu Z S 2022 Research progress on selective laser melting (SLM) of bulk metallic glasses (BMGs): a review *Int. J. Adv. Manuf. Technol.* **118** 2017–57

[172] Zhang C, Ouyang D, Pauly S and Liu L 2021 3D printing of bulk metallic glasses *Mater. Sci. Eng.* R **145** 100625

[173] Li F C, Liu T, Zhang J Y, Shuang S, Wang Q, Wang A D, Wang J G and Yang Y 2019 Amorphous-nanocrystalline alloys: fabrication, properties, and applications *Mater. Today Adv.* **4** 100027

[174] Ouyang D, Li N, Xing W, Zhang J J and Liu L 2017 3D printing of crack-free high strength Zr-based bulk metallic glass composite by selective laser melting *Intermetallics* **90** 128–34

[175] Chen C, Ling C R, Shao Y J, Yang Y, Wang D and Shuai C 2023 Quasicrystal-strengthened biomedical magnesium alloy fabricated by laser additive manufacturing *J. Alloys Compd.* **947** 169555

[176] Zhang C H, Li Z, Zhang J K, Tang H B and Wang H M 2023 Additive manufacturing of magnesium matrix composites: comprehensive review of recent progress and research perspectives *J. Magnes. Alloys* **11** 425–61

[177] Wu C L, Xie W J and Man H C 2022 Laser additive manufacturing of biodegradable Mg-based alloys for biomedical applications: a review *J. Magnes. Alloys* **10** 915–37

[178] Yuan Q H, Zhou G H, Liao L, Liu Y and Luo L 2018 Interfacial structure in AZ91 alloy composites reinforced by graphene nanosheets *Carbon* **127** 177–86

[179] Nie K B, Wang X J, Deng K K, Hu X S and Wu K 2021 Magnesium matrix composite reinforced by nanoparticles-a review *J. Magnes. Alloys* **9** 57–77

[180] Chen L Y, Xu J Q, Choi H, Pozuelo M, Ma X, Bhowmick S, Yang J M, Mathaudhu S and Li X C 2015 Processing and properties of magnesium containing a dense uniform dispersion of nanoparticles *Nature* **528** 539–43

[181] Min Y, Akbulut M, Kristiansen K, Golan Y and Israelachvili J 2008 The role of interparticle and external forces in nanoparticle assembly *Nat. Mater.* **7** 527–38

[182] Shuai C J, Wang B, Bin S, Peng S P and Gao C D 2020 TiO_2-induced in situ reaction in graphene oxide-reinforced AZ61 biocomposites to enhance the interfacial bonding *ACS Appl. Mater. Interfaces* **12** 23464–73

[183] Gangireddy S, Gwalani B, Liu K M, Faierson E J and Mishra R S 2019 Microstructure and mechanical behavior of an additive manufactured (AM) WE43-Mg alloy *Addit. Manuf.* **26** 53–64

[184] Xu H J, Peng B, Liu J G, Song F, Tian Y, Zheng Y F and Wen P 2024 Improved passivation effect of additively manufactured WE43 porous scaffolds treated by high temperature oxidation in pure oxygen atmosphere *Mater. Lett.* **357** 135713

[185] Liu B C, Liu J G, Wang C X, Wang Z G, Min S Y, Wang C M, Zheng Y F, Wen P and Tian Y 2024 High temperature oxidation treated 3D printed anatomical WE43 alloy scaffolds for repairing periarticular bone defects: *in vitro* and *in vivo* studies *Bioact. Mater.* **32** 177–89

[186] Liu J G, Yin B, Song F, Liu B, Peng B, Wen P, Tian Y, Zheng Y, Ma X and Wang C 2024 Improving corrosion resistance of additively manufactured WE43 magnesium alloy by high temperature oxidation for biodegradable applications *J. Magnes. Alloys* **12** 940–53

[187] Li K, Chen W, Yin B Z, Ji C, Bai S W, Liao R B, Yang T B, Wen P, Jiang B and Pan F S 2023 A comparative study on WE43 magnesium alloy fabricated by laser powder bed fusion coupled with deep cryogenic treatment: evolution in microstructure and mechanical properties *Addit. Manuf.* **77** 103814

[188] Kopp A, Derra T, Müther M, Jauer L, Schleifenbaum J H, Voshage M, Jung O, Smeets R and Kröger N 2019 Influence of design and postprocessing parameters on the degradation behavior and mechanical properties of additively manufactured magnesium scaffolds *Acta Biomater.* **98** 23–35

[189] Yang Y W, Ling C R, Li Y G, Peng S P, Xie D Q, Shen L D, Tian Z J and Shuai C J 2023 Microstructure development and biodegradation behavior of additively manufactured Mg-Zn-Gd alloy with LPSO structure *J. Mater. Sci. Technol.* **144** 1–14

[190] Liu S and Guo H J 2020 Influence of hot isostatic pressing (HIP) on mechanical properties of magnesium alloy produced by selective laser melting (SLM) *Mater. Lett.* **265** 127463

[191] Liang J W, Lei Z L, Chen Y B, Fu W J, Wu S B, Chen X and Yang Y C 2022 Microstructure evolution of laser powder bed fusion ZK60 Mg alloy after different heat treatment *J. Alloys Compd.* **898** 163046

[192] Sorkhi L, Hammell J J and Crawford G A 2020 Effect of interlayer interval time on the microstructure and mechanical behavior of additively manufactured WE43 mg alloy *Metall. Mater. Trans.* A **51** 4390–405

[193] Åhman H N, D'Elia F, Mellin P and Persson C 2022 Microstructural origins of the corrosion resistance of a Mg-Y-Nd-Zr alloy processed by powder bed fusion-laser beam *Front. Bioeng. Biotechnol.* **10** 917812

[194] Liu J G, Min S Y, Mao Z J, Zhou M R, Liu B C, Liu D Z, Song F, Wen P, Tian Y and Zheng Y F 2024 Influence of high temperature oxidation on mechanical properties and *in vitro* biocompatibility of WE43 magnesium alloy fabricated by laser powder bed fusion *J. Mater. Sci. Technol.* **179** 26–39

[195] Gnedenkov A S, Sinebryukhov S L, Mashtalyar D V and Gnedenkov S V 2016 Protective properties of inhibitor-containing composite coatings on a Mg alloy *Corros. Sci.* **102** 348–54

[196] Li X Z, Fang X W, Jiang X, Duan Y S, Li Y, Zhang H K, Li X P and Huang K 2023 Additively manufactured high-performance AZ91D magnesium alloys with excellent strength and ductility via nanoparticles reinforcement *Addit. Manuf.* **69** 103550

[197] Pawlak A, Szymczyk P E, Kurzynowski T and Chlebus E 2019 Selective laser melting of magnesium AZ31B alloy powder *Rapid Prototyp. J.* **26** 249–58

[198] Liu S and Guo H J 2022 Influence of heat treatment on microstructure and mechanical properties of AZ61 magnesium alloy prepared by selective laser melting (SLM) *Materials* **15** 7067

[199] Deng Q C, Chang Z Y, Su N, Luo J, Liang Y Y, Jin Y H, Wu Y J, Peng L M and Ding W J 2023 Developing a novel high-strength Mg-Gd-Y-Zn-Mn alloy for laser powder bed fusion additive manufacturing process *J. Magnes. Alloys* (https://doi.org/10.1016/j.jma.2023.09.027)

[200] Fu P H, Wang N Q, Liao H G, Xu W Y, Peng L M, Chen J, Hu G Q and Ding W J 2021 Microstructure and mechanical properties of high strength Mg-15Gd-1Zn-0.4Zr alloy additive-manufactured by selective laser melting process *Trans. Nonferrous Met. Soc.* **31** 1969–78

[201] Baptista L S, Kronemberger G S, Côrtes I, Charelli L E, Matsui R A M, Palhares T N, Sohier J, Rossi A M and Granjeiro J M 2018 Adult stem cells spheroids to optimize cell colonization in scaffolds for cartilage and bone tissue engineering *Int. J. Mol. Sci.* **19** 1285

[202] Wu S L, Liu X M, Yeung K W K, Liu C S and Yang X J 2014 Biomimetic porous scaffolds for bone tissue engineering *Mater. Sci. Eng.* R **80** 1–36

[203] Carluccio D, Xu C, Venezuela J, Cao Y X, Kent D, Bermingham M, Demir A G, Previtali B, Ye Q S and Dargusch M 2020 Additively manufactured iron-manganese for biodegradable porous load-bearing bone scaffold applications *Acta Biomater.* **103** 346–60

[204] Tao J X, Zhao M C, Zhao Y C, Yin D F, Liu L, Gao C D, Shuai C J and Atrens A 2020 Influence of graphene oxide (GO) on microstructure and biodegradation of ZK30-xGO composites prepared by selective laser melting *J. Magnes. Alloys* **8** 952–62

[205] Gao C D, Li S, Liu L, Bin S, Yang Y W, Peng S P and Shuai C J 2021 Dual alloying improves the corrosion resistance of biodegradable Mg alloys prepared by selective laser melting *J. Magnes. Alloys* **9** 305–16

[206] Wu C L, Zhang S, Zhang C H, Zhang J B, Liu Y and Chen J 2019 Effects of SiC content on phase evolution and corrosion behavior of SiC-reinforced 316L stainless steel matrix composites by laser melting deposition *Opt. Laser Technol.* **115** 134–9

[207] Chang C, Liao H L, Yi L, Dai Y L, Cox S C, Yan M, Liu M and Yan X C 2023 Achieving ultra-high strength and ductility in Mg-9Al-1Zn-0.5Mn alloy via selective laser melting *Adv. Powder Mater.* **2** 100097

[208] Li Y *et al* 2018 Additively manufactured biodegradable porous iron *Acta Biomater.* **77** 380–93

[209] Bobbert F S L, Lietaert K, Eftekhari A A, Pouran B, Ahmadi S M, Weinans H and Zadpoor A A 2017 Additively manufactured metallic porous biomaterials based on minimal surfaces: a unique combination of topological, mechanical, and mass transport properties *Acta Biomater.* **53** 572–84

[210] Zadpoor A A 2019 Mechanical performance of additively manufactured meta-biomaterials *Acta Biomater.* **85** 41–59

[211] Wang Y C, Huang H, Jia G Z, Zeng H and Yuan G Y 2021 Fatigue and dynamic biodegradation behavior of additively manufactured Mg scaffolds *Acta Biomater.* **135** 705–22

[212] Bhuiyan M, Mutoh Y, Murai T and Iwakami S 2008 Corrosion fatigue behavior of extruded magnesium alloy AZ61 under three different corrosive environments *Int. J. Fatigue* **30** 1756–65

[213] Bian D, Zhou W R, Liu Y, Li N, Zheng Y F and Sun Z L 2016 Fatigue behaviors of HP-Mg, Mg-Ca and Mg-Zn-Ca biodegradable metals in air and simulated body fluid *Acta Biomater.* **41** 351–60

[214] Jafari S, Raman R K S, Davies C H J, Hofstetter J, Uggowitzer P J and Löffler J F 2017 Stress corrosion cracking and corrosion fatigue characterisation of MgZn1Ca0. 3 (ZX10) in a simulated physiological environment *J. Mech. Behav. Biomed. Mater.* **65** 634–43

[215] Yi M, Tang W, Zhu Y Q, Liang C G, Tang Z M, Yin Y, He W W, Sun S and Su S P 2024 A holistic review on fatigue properties of additively manufactured metals *J. Mater. Process. Technol.* **329** 118425

[216] Li Y, Jahr H, Zhang X Y, Leeflang M A, Li W, Pouran B, Tichelaar F D, Weinans H, Zhou J and Zadpoor A A 2019 Biodegradation-affected fatigue behavior of additively manufactured porous magnesium *Addit. Manuf.* **28** 299–311

[217] Gu X N, Li N, Zhou W R, Zheng Y F, Zhao X, Cai Q Z and Ruan L Q 2011 Corrosion resistance and surface biocompatibility of a microarc oxidation coating on a Mg-Ca alloy *Acta Biomater.* **7** 1880–9

[218] Wang H X, Guan S K, Wang X, Ren C X and Wang L G 2010 *In vitro* degradation and mechanical integrity of Mg-Zn-Ca

alloy coated with Ca-deficient hydroxyapatite by the pulse electrodeposition process *Acta Biomater.* **6** 1743–8

[219] Fan J, Qiu X, Niu X D, Tian Z, Sun W, Liu X J, Li Y D, Li W R and Meng J 2013 Microstructure, mechanical properties, *in vitro* degradation and cytotoxicity evaluations of Mg-1.5Y-1.2Zn-0.44Zr alloys for biodegradable metallic implants *Mater. Sci. Eng.* C **33** 2345–52

[220] Shuai C J, Liu L, Zhao M C, Feng P, Yang Y W, Guo W, Gao C D and Yuan F L 2018 Microstructure, biodegradation, antibacterial and mechanical properties of ZK60-Cu alloys prepared by selective laser melting technique *J. Mater. Sci. Technol.* **34** 1944–52

[221] Shuai C J, Zhou Y Z, Yang Y W, Gao C D, Peng S P and Wang G Y 2018 Ag-introduced antibacterial ability and corrosion resistance for Bio-Mg alloys *BioMed Res. Int.* **2018** 6023460

[222] Ding J, Zhao W M, Qin L and Li Y Y 2014 Study of Ca and Ce additions on different ignition resistance behavior of magnesium alloy *Mater. Sci. Forum.* **788** 7–11

[223] Ghorbani M, Boley M, Nakashima P N H and Birbilis N 2024 An active machine learning approach for optimal design of magnesium alloys using Bayesian optimisation *Sci. Rep.* **14** 8299

[224] Dong S Y, Wang Y Y, Li J Y, Li Y Y, Wang L and Zhang J L 2024 Machine learning aided prediction and design for the mechanical properties of magnesium alloys *Met. Mater. Int.* **30** 593–606

[225] Hou H B, Wang J F, Ye L, Zhu S J, Wang L G and Guan S K 2023 Prediction of mechanical properties of biomedical magnesium alloys based on ensemble machine learning *Mater. Lett.* **348** 134605

[226] Cheng Y H, Wang L F, Yang C Y, Bai Y L, Wang H X, Cheng W L, Tiyyagura H R, Komissarov A and Shin K S 2024 A brief review of machine learning-assisted Mg alloy design, processing, and property predictions *J. Mater. Res. Technol.* **30** 8108–27

[227] Gou W, Shi Z Z, Zhu Y M, Gu X F, Dai F Z, Gao X Y and Wang L N 2024 Multi-objective optimization of three mechanical properties of Mg alloys through machine learning *Mater. Genome Eng. Adv.* **2** e54

[228] Bommala V K, Krishna M G and Rao C T 2019 Magnesium matrix composites for biomedical applications: a review *J. Magnes. Alloys* **7** 72–79

[229] Kumar K, Das A and Prasad S B 2021 Recent developments in biodegradable magnesium matrix composites for orthopaedic applications: a review based on biodegradability, mechanical and biocompatibility perspective *Mater. Today Proc.* **44** 2038–42

[230] Prajapati S K, Jain A, Jain A and Jain S 2019 Biodegradable polymers and constructs: a novel approach in drug delivery *Eur. Polym. J.* **120** 109191

[231] Shuai C, Zhou Y Z, Yang Y W, Feng P, Liu L, He C X, Zhao M C, Yang S, Gao C D and Wu P 2017 Biodegradation resistance and bioactivity of hydroxyapatite enhanced Mg-Zn composites via selective laser melting *Materials* **10** 307

[232] Yang Y W, Lu C F, Peng S P, Shen L D, Wang D, Qi F W and Shuai C J 2020 Laser additive manufacturing of Mg-based composite with improved degradation behaviour *Virtual Phys. Prototyp.* **15** 278–93

[233] Yang Y W, Lu C F, Shen L D, Zhao Z Y, Peng S P and Shuai C J 2023 *In-situ* deposition of apatite layer to protect Mg-based composite fabricated via laser additive manufacturing *J. Magnes. Alloys* **11** 629–40

[234] Wits W W, Smit M D, Al-Hamdani K and Clare A T 2019 Laser powder bed fusion of a Magnesium-SiC metal matrix composite *Proc. CIRP* **81** 506–11

[235] Abazari S, Shamsipur A, Bakhsheshi-Rad H R, Drelich J W, Goldman J, Sharif S, Ismail A F and Razzaghi M 2023 Magnesium-based nanocomposites: a review from mechanical, creep and fatigue properties *J. Magnes. Alloys* **11** 2655–87

[236] Ahmadi S M, Hedayati R, Li Y, Lietaert K, Tümer N, Fatemi A, Rans C D, Pouran B, Weinans H and Zadpoor A A 2018 Fatigue performance of additively manufactured meta-biomaterials: the effects of topology and material type *Acta Biomater.* **65** 292–304

[237] Mei D, Lamaka S V, Lu X P and Zheludkevich M L 2020 Selecting medium for corrosion testing of bioabsorbable magnesium and other metals—a critical review *Corros. Sci.* **171** 108722

[238] Jähn K *et al* 2016 Intramedullary Mg_2Ag nails augment callus formation during fracture healing in mice *Acta Biomater.* **36** 350–60

[239] Lovašiová P, Lovaši T, Kubásek J, Jablonská E, Msallamová Š, Michalcová A, Vojtěch D, Suchý J, Koutný D and Ghassan Hamed Alzubi E 2022 Biodegradable WE43 magnesium alloy produced by selective laser melting: mechanical properties, corrosion behavior, and *in-vitro* cytotoxicity *Metals* **12** 469

[240] Xie B, Zhao M C, Tao J X, Zhao Y C, Yin D F, Gao C D, Shuai C J and Atrens A 2021 Comparison of the biodegradation of ZK30 subjected to solid solution treating and selective laser melting *J. Mater. Res. Technol.* **10** 722–9

[241] Praveen T S, Padmanaban R, Vaira Vignesh R and Baghad A 2024 Investigations on the corrosion characteristics of additive manufactured Mg-Ag alloy in simulated body fluids for biodegradable *Prog. Addit. Manuf.* (https://doi.org/10.1007/s40964-024-00705-x)

[242] Shuai C J, Liu L, Gao C D, Yang W J, Zhao Z Y, Tan Y and Liao W W 2020 Mn-promoting formation of a long-period stacking-ordered phase in laser-melted Mg alloys to enhance degradation resistance *Mater. Corros.* **71** 553–63

[243] Shuai C J, Yang W J, Yang Y W, Gao C D, He C X and Pan H 2019 A continuous net-like eutectic structure enhances the corrosion resistance of Mg alloys *Int. J. Bioprint.* **5** 207

[244] Gao C D, Zeng Z H, Peng S P, Tan W and Shuai C J 2021 A continuous MgF_2 network structure encapsulated mg alloy prepared by selective laser melting for enhanced biodegradation resistance *Adv. Eng. Mater.* **23** 2100389

[245] Shuai C J, Wang B, Bin S Z, Peng S P and Gao C D 2020 Interfacial strengthening by reduced graphene oxide coated with MgO in biodegradable Mg composites *Mater. Des.* **191** 108612

[246] Shuai C J, Wang B, Yang Y W, Peng S P and Gao C D 2019 3D honeycomb nanostructure-encapsulated magnesium alloys with superior corrosion resistance and mechanical properties *Composites* B **162** 611–20

[247] Liu H R, Li D F, Zhang Y and Li M Q 2018 Inflammation, mesenchymal stem cells and bone regeneration *Histochem. Cell Biol.* **149** 393–404

[248] Zheng Y F, Gu X N and Witte F 2014 Biodegradable metals *Mater. Sci. Eng.* R **77** 1–34

[249] Li K, Ji C, Bai S W, Jiang B and Pan F S 2023 Selective laser melting of magnesium alloys: necessity, formability, performance, optimization and applications *J. Mater. Sci. Technol.* **154** 65–93

[250] Song G L 2007 Control of biodegradation of biocompatable magnesium alloys *Corros. Sci.* **49** 1696–701

[251] Agarwal S, Curtin J, Duffy B and Jaiswal S 2016 Biodegradable magnesium alloys for orthopaedic applications: a review on corrosion, biocompatibility and surface modifications *Mater. Sci. Eng.* C **68** 948–63

[252] Kumar R and Katyal P 2022 Effects of alloying elements on performance of biodegradable magnesium alloy *Mater. Today Proc.* **56** 2443–50

[253] Hassan S F, Islam M T, Saheb N and Baig M M A 2022 Magnesium for implants: a review on the effect of alloying elements on biocompatibility and properties *Materials* **15** 5669

[254] Ding Y F, Wen C, Hodgson P and Li Y C 2014 Effects of alloying elements on the corrosion behavior and biocompatibility of biodegradable magnesium alloys: a review *J. Mater. Chem.* B **2** 1912–33

[255] Zhang T, Shao Y W, Meng G Z, Cui Z Y and Wang F H 2011 Corrosion of hot extrusion AZ91 magnesium alloy: i-relation between the microstructure and corrosion behavior *Corros. Sci.* **53** 1960–8

[256] Shuai C J, Yang Y W, Wu P, Lin X, Liu Y, Zhou Y Z, Feng P, Liu X Y and Peng S P 2017 Laser rapid solidification improves corrosion behavior of Mg-Zn-Zr alloy *J. Alloys Compd.* **691** 961–9

[257] Benn F *et al* 2021 Influence of surface condition on the degradation behaviour and biocompatibility of additively manufactured WE43 *Mater. Sci. Eng.* C **124** 112016

[258] Zhang A M, Lenin P, Zeng R C and Kannan M B 2022 Advances in hydroxyapatite coatings on biodegradable magnesium and its alloys *J. Magnesium Alloys* **10** 1154–70

[259] Shadanbaz S and Dias G J 2012 Calcium phosphate coatings on magnesium alloys for biomedical applications: a review *Acta Biomater.* **8** 20–30

[260] Li X, Liu X M, Wu S L, Yeung K W K, Zheng Y F and Chu P K 2016 Design of magnesium alloys with controllable degradation for biomedical implants: from bulk to surface *Acta Biomater.* **45** 2–30

[261] Wang Q, Wang W, Jiang D J and Jia W T 2021 Evaluation of JDBM porous scaffold coated with DCPD in promoting angiogenesis and repairing bone defects *J. Shanghai Jiaotong Univ.* **41** 732–40

[262] Hu Q J, Chen C, Liu M, Chang C, Yan X C and Dai Y L 2023 Improved corrosion resistance of magnesium alloy prepared by selective laser melting through T4 heat treatment for biomedical applications *J. Mater. Res. Technol.* **27** 813–25

[263] Wang C X *et al* 2023 The effect of pore size on the mechanical properties, biodegradation and osteogenic effects of additively manufactured magnesium scaffolds after high temperature oxidation: an *in vitro* and *in vivo* study *Bioact. Mater.* **28** 537–48

[264] Wang C X, Min S Y, Liu J G, Liu B C, Peng B, Wang C M, Ma X L, Wen P, Zheng Y F and Tian Y 2023 Effect of pore geometry on properties of high-temperature oxidized additively manufactured magnesium scaffolds *J. Magnesium Alloys* (https://doi.org/10.1016/j.jma.2023.08.016)

[265] Xie K *et al* 2022 Additively manufactured biodegradable porous magnesium implants for elimination of implant-related infections: an *in vitro* and *in vivo* study *Bioact. Mater.* **8** 140–52

[266] Lin X, Zhang R T, Lu W F, Zhu K P and Dan B B 2024 Effect of additive manufactured gyroid porous structure of hybrid gradients on mechanical and failure properties *Addit. Manuf. Front.* **3** 200152

[267] Feng J W, Fu J Z, Yao X H and He Y 2022 Triply periodic minimal surface (TPMS) porous structures: from multi-scale design, precise additive manufacturing to multidisciplinary applications *Int. J. Extreme Manuf.* **4** 022001

[268] Li D W, Dai N, Tang Y L, Dong G Y and Zhao Y F 2019 Design and optimization of graded cellular structures with triply periodic level surface-based topological shapes *J. Mech. Des.* **141** 071402

[269] Senhora F V, Sanders E D and Paulino G H 2022 Optimally-tailored spinodal architected materials for multiscale design and manufacturing *Adv. Mater.* **34** 2109304

[270] Chen W, Gu D D, Yang J K, Yang Q, Chen J and Shen X F 2022 Compressive mechanical properties and shape memory effect of NiTi gradient lattice structures fabricated by laser powder bed fusion *Int. J. Extreme Manuf.* **4** 045002

[271] Peng B, Wei Y, Qin Y, Dai J B, Li Y, Liu A B, Tian Y, Han L L, Zheng Y F and Wen P 2023 Machine learning-enabled constrained multi-objective design of architected materials *Nat. Commun.* **14** 6630

[272] Ma C P, Zhang Z W, Luce B, Pusateri S, Xie B L, Rafiei M H and Hu N 2020 Accelerated design and characterization of non-uniform cellular materials via a machine-learning based framework *npj Comput. Mater.* **6** 40

[273] Liu Y, Zhao T L, Ju W W and Shi S Q 2017 Materials discovery and design using machine learning *J. Mater.* **3** 159–77

[274] Hippalgaonkar K, Li Q X, Wang X N, Fisher J W, Kirkpatrick J and Buonassisi T 2023 Knowledge-integrated machine learning for materials: lessons from gameplaying and robotics *Nat. Rev. Mater.* **8** 241–60

[275] Atrens A, Song G L, Cao F Y, Shi Z M and Bowen P K 2013 Advances in Mg corrosion and research suggestions *J. Magnes. Alloys* **1** 177–200

[276] Matena J, Petersen S, Gieseke M, Teske M, Beyerbach M, Kampmann A, Escobar H M, Gellrich N C, Haferkamp H and Nolte I 2015 Comparison of selective laser melted titanium and magnesium implants coated with PCL *Int. J. Mol. Sci.* **16** 13287–301